2011

A Shock Tube Technique for Blast Wave Simulation and Studies of Flow Structure Interactions in Shock Tube Blast Experiments

Nicholas N. Kleinschmit
University of Nebraska-Lincoln, n_kleinschmit@yahoo.com

Kleinschmit, Nicholas N., "A Shock Tube Technique for Blast Wave Simulation and Studies of Flow Structure Interactions in Shock Tube Blast Experiments" (2011). *Engineering Mechanics Dissertations & Theses*. 22.
https://digitalcommons.unl.edu/engmechdiss/22

A Shock Tube Technique for Blast Wave Simulation and Studies of Flow Structure Interactions in Shock Tube Blast Experiments

By:

Nicholas Noel Kleinschmit

A THESIS

Presented to the Faculty of

The Graduate College at the University of Nebraska

In Partial Fulfillment of Requirements

For the Degree of Master of Science

Major: Engineering Mechanics

Under the Supervision of Professor Ruqiang Feng

Lincoln, Nebraska

August 2011

A Shock Tube Technique for Blast Wave Simulation and Studies of Flow Structure Interactions in Shock Tube Blast Experiments

Nicholas Noel Kleinschmit, M.S.

University of Nebraska, 2011

Advisor: Ruqiang Feng

Improvised explosive devices (IED's) are widely used against US and allied forces fighting in Iraq and Afghanistan. Exposure to IED blast may cause blast-induced traumatic brain injury (bTBI). The injury mechanisms are however not well understood. A critical need in bTBI-related research is the ability to replicate the loading conditions of IED blast waves in a laboratory environment. In this work, experimental studies have been carried out to explore the use of the shock tube technique for generating air shock waves that mimic the temporal and spatial characteristics of free-field blast waves and to investigate the blast wave-test sample interactions in such a simulated blast experiment.

To facilitate the studies, new data acquisition and analysis systems for shock tube experiments were developed along with LabVIEW-based software. Techniques for proper mounting of piezoelectric sensors in square shock tubes were also worked out.

Evolutions of the blast waves simulated with a 9-inch square shock tube inside and outside the tube were then investigated by placing a metal cylinder instrumented with piezoelectric sensor array at various locations of interest. The results show that the temporal and spatial characteristics of free-field blast waves can only be replicated *deep inside* the tube. The lateral expansion as the shock front exits the tube causes unwanted

premature release in part of the tube near the exit and complex three-dimensional flow which evolves quickly into subsonic jet flow outside the exit. Motivated by the results, a 28-inch square shock tube adequate for *in-tube* full scale head/helmet model testing was developed along with a catch tank for blast energy mitigation and noise reduce. Its modular configuration was optimized for best efficiency. Correlations of the peak shock pressure and the positive impulse with the diaphragm burst pressure were determined for various configurations. Accurate (Friedlander) blast wave profiles were obtained for peak pressures from 5.5 to 42 psi and for positive durations from 4 to 9.25 ms.

The interactions between the blast waves simulated with the 9-inch shock tube and cylindrical polycarbonate tubes filled with a mineral oil as idealized two-dimensional skull-brain models were then studied. The results indicate that the sample geometry causes flow separation from lateral surfaces and thus large surface pressure gradients and lateral underpressure pulses as the blast wave engulfs the sample. While the sample front and then the back are compressed, parts of it expand with the underpressure pulses. Such a deformation and the subsequent recovery/oscillation dictate the internal pressure response, which oscillates with multiple full releases and even reversals to underpressure and therefore is temporally different from the pressure wave impinging on the sample front. A thicker shell may reverse from lateral elliptic to front-back elliptic under higher loadings. This can cause cavitations at the front and back walls. These findings have provided, for the first time, experimental measurements of the dynamic response of fluid-filled cylinders (simplified skull-brain models) subjected to blast wave loading.

Dedication

I would like to dedicate this thesis to:

Those who read my thesis with intent to study blast induced traumatic brain injuries

&

To the soldiers who sacrifice so much for our freedom.

Acknowledgements

The writing of my thesis has been a challenging journey that would not have been possible without the help and encouragement from many people. My efforts would have been futile if it hadn't been for you.

I would like to thank my parents for the education they gave me since I was young. You instilled in me a great work ethic and sparked my mechanical interest.

I would like to thank my wife Laura for supporting my decision to partake in graduate studies. I couldn't have done it without your love and support.

I would like to thank my advisor, Dr. Feng, for his guidance and support throughout my studies. Your knowledge of engineering mechanics was of great assistance when questions arose.

I would like to thank Aaron Holmberg for his technical advice and suggestions. Your ideas always had positive contributions during our frequent brainstorming sessions.

I would also like to thank Jonathan Hein and Aaron Alai for their technical support during experiments. I could always count on you both for experimental assistance.

I would like to thank Dr. Feng, Dr. Nelson, and Dr. Turner for serving on my thesis committee and for their assistance and constructive comments. Your time and efforts are greatly appreciated.

Thank you to the rest of my family and friends for always being there for me. Spending time with you is always appreciated, especially after long periods of studying.

Table of Contents

CHAPTER 4: WAVE PROFILE EVOLUTION OUTSIDE A SHOCK TUBE....81

CHAPTER 5: DEVELOPMENT AND CHARACTERIZATION OF A 28-INCH SHOCK TUBE.... 97

List of Figures

List of Tables

Chapter 1: Introduction

The increased use of improvised explosive devices (IEDs) has caused significant casualties among soldiers involved in the war on terror in Iraq and Afghanistan (Ramasamy, et al., 2008). Improved body armor provides better protection for soldiers, reducing the damage that was previously caused by other injury mechanisms such as shrapnel, projectiles, and blunt impact, but does not adequately protect soldiers against blast waves, leading to an increased risk for mild traumatic brain injury (mTBI). Furthermore, the size of improvised explosive devices is increasing causing higher intensity blasts and stressing the need for better protection from IEDs (Holmberg, 2010).

Ramasamy et al. (2008) compiled data from 100 consecutive casualties from the War on Terror; 53 of these casualties occurred from 23 different IED incidents, which corresponds to 2.3 casualties per incident and demonstrates the power of the explosives being used. Hoge et al. (2008) interviewed 2525 soldiers after returning from a 1 year tour in Iraq and found that 4.9% reported injuries associated with a loss of consciousness. They found a strong link between post traumatic stress disorder (PTSD) and TBI, which significantly reduces the quality of life of a returning soldier. Another article stated "35% of the battlefield casualties evacuated to the National Naval Medical Center from April 2003 to October 2005 required neurosurgical consultation and treatment, with the majority of these injuries resulting directly or indirectly from blasts propagated by improvised explosive devices (IEDs)" (Long et al., 2009). These conclusions from a variety of sources firmly state the need to better understand blast induced traumatic brain injury.

1.1 Background

This section contains literature review of previous shock wave, TBI, and explosives related research. Shock wave theory and derivation is also contained in this section.

1.1.1 Literature review

Shock tubes are regularly used for generating shock waves to simulate the primary blast loading effects of an explosive. They come in a variety of shapes and sizes and can therefore produce various shock wave profiles. A shock tube used by Bauman et al. (2008) was 71 inches in diameter and 68 feet long, while a shock tube used by the University of Wisconsin has a 10 inch square cross section. From a mechanical perspective, one of the most important aspects of blast induced TBI research is the generation of shock waves that accurately represent conditions created by an explosive blast. Actual pressure profiles collected by Mott et al. (2008) for a 0.75 kg spherical C4 charge are shown in Figure 1-1. The demonstrated charge is much smaller than typical improvised explosive devices, since a suicide bomber's vest carries approximately 10 kg of explosives and a small car bomb contains approximately 100 kg (NCTC, 2011).

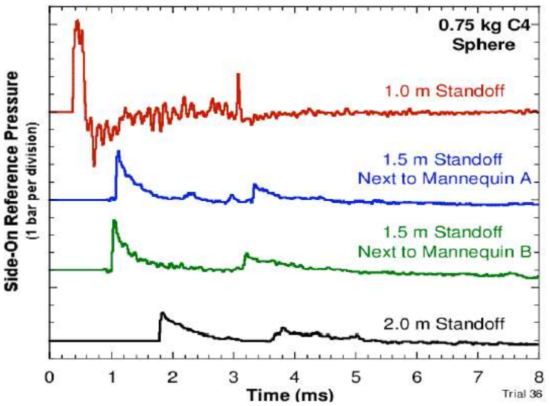

Figure 1-1: Pressure histories at various distances from a 0.75 kg spherical C4 charge (Mott, et al., 2008)

A typical free-field blast wave takes the form of a planar Friedlander wave at a significant distance from the explosion source location. This wave has the characteristics of a positive-pressure phase decaying to ambient pressure, followed by a negative pressure phase as shown in Figure 1-2.

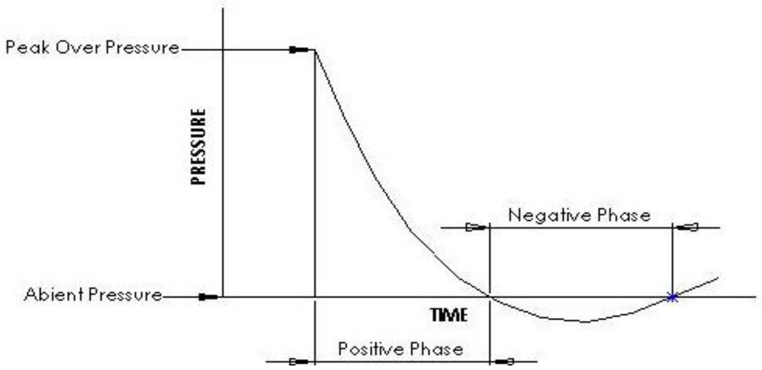

Figure 1-2: Idealized free field blast wave profile (Friedlander wave) (Holmberg, 2009)

Because the shock waves generated at the UNL shock facility are intended to replicate the blast waves generated by explosives, the explosive equivalence should be known for an experimental shock profile. Figure 1-3 is a compilation of data by Esparza (1986) showing the side-on peak pressure (psi) versus scaled distance (ft/lb^1/3) for spherical TNT charges. These tables can be used to correlate shock tube generated loading to explosive driven blast waves. The use of shaped charges is a common practice which optimizes the destructive power of the explosive, but the characterization of these can be much more complicated (Pack & Curtis, 1999). Explosive data is available for hemispherical TNT equivalencies (Huntington, 2001), but is not explored in this thesis. Analysis of complicated explosive configurations can be computed using ConWep (Protection Engineering Consultants, 2010).

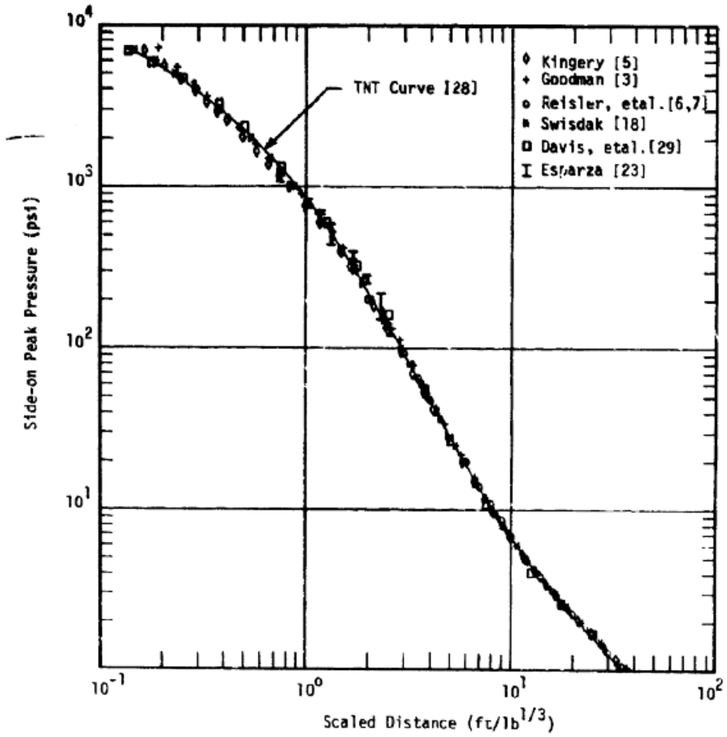

Figure 1-3: Comparison of side-on peak pressure (psi) to scaled distance (ft/lb^3) for spherical TNT charges compiled from multiple sources (Esparza, 1986).

Figure 1-4 is the second part of the spherical TNT characterization compiled by Esparza (1986) which compares the scaled positive duration to the scaled distance. The positive duration data is not as consistent, but does give a close approximation of a shock wave duration for a given charge weight/distance.

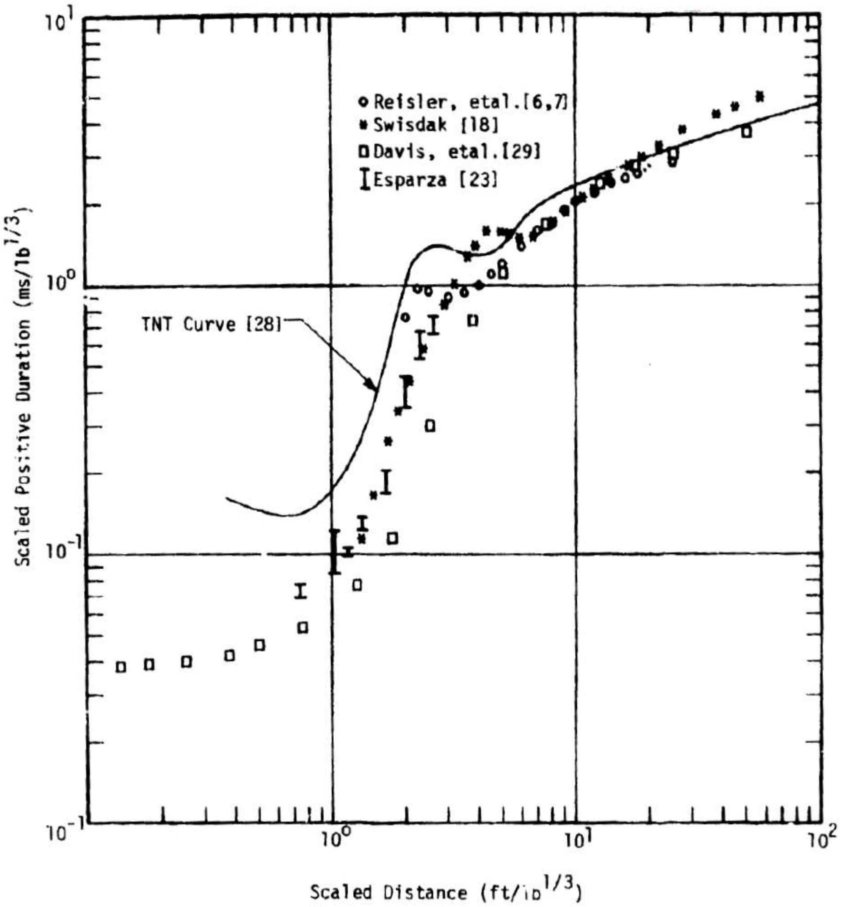

Figure 1-4: Comparison of scaled positive duration (ms/lb^3) to scaled distance (ft/lb^3) for spherical TNT charges compiled from multiple sources (Esparza, 1986).

An example explosive weight of 125 pounds at a distance of 20 feet would produce a scaled distance of 4 and a peak pressure of approximately 50 psi from Figure 1-3. Using a scaled distance of 4 in Figure 1-4 yields a scaled positive duration of approximately 1. Multiplying this by the cube root of the weight (125^(1/3)) produces an actual positive duration of approximately 5 ms. The reverse procedure can be performed to determine the equivalent TNT weight and distance using peak pressure and positive duration data from an actual shock wave profile.

TNT is one of the most common explosives, but others are commonly used as well. General pressure and impulse equivalencies to TNT are shown in Figure 1-5 for some explosives such as C4 and Composition B (NCTC, 2011).

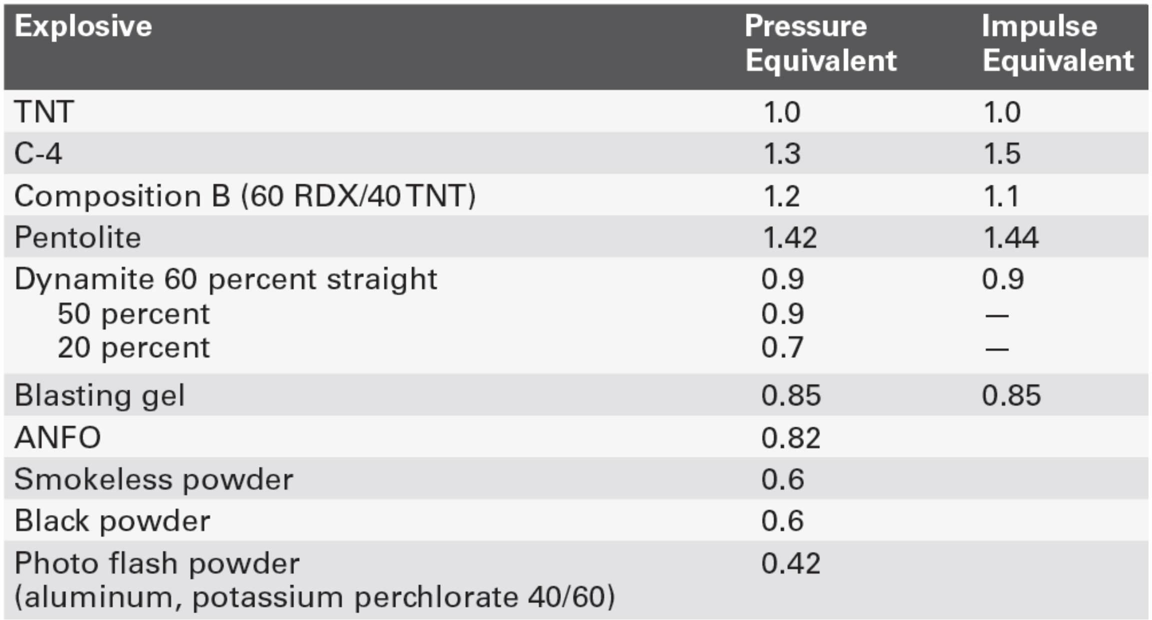

Explosive	Pressure Equivalent	Impulse Equivalent
TNT	1.0	1.0
C-4	1.3	1.5
Composition B (60 RDX/40 TNT)	1.2	1.1
Pentolite	1.42	1.44
Dynamite 60 percent straight	0.9	0.9
50 percent	0.9	—
20 percent	0.7	—
Blasting gel	0.85	0.85
ANFO	0.82	
Smokeless powder	0.6	
Black powder	0.6	
Photo flash powder (aluminum, potassium perchlorate 40/60)	0.42	

Figure 1-5: Pressure and impulse equivalencies to TNT for common explosives (NCTC, 2011)

Explosive induced injury can be caused by four different blast phases including primary, secondary, tertiary, and quaternary injuries, although the first three are the main culprits of blast induced traumatic brain injury (Chen, et al., 2009). Primary injury corresponds to the shock wave pressure loading, secondary injury corresponds to ballistic/shrapnel penetration, tertiary injury corresponds to accelerations caused by blunt impact, and quaternary injury relates to all other injuries that follow such as chemical or burn injuries. Primary blast injury was commonly observed during World War 1, and was given the term "shell shock" (Chen, et al., 2009). Traumatic brain injuries are typically caused by the first three modes, but primary blast injury is the least understood and is the only mode studied in this thesis.

Historically, pulmonary (lung related) injury thresholds for a human were derived from a variety of animal models by Bowen (1968). Pulmonary injury thresholds are typically lower than TBI injury thresholds, but modern body armor provides significant pulmonary protection leading to the increased occurrence of TBI. However, consistent injury thresholds for bTBI have not been developed. Bowen's pulmonary injury models were not published in peer reviewed literature and the animal-human scaling of blast thresholds has been questioned for accuracy for the short duration shock waves (Bass, et al., 2008). A re-analyzed model published by Bass et al. (2008) produced the injury threshold shown in Figure 1-6.

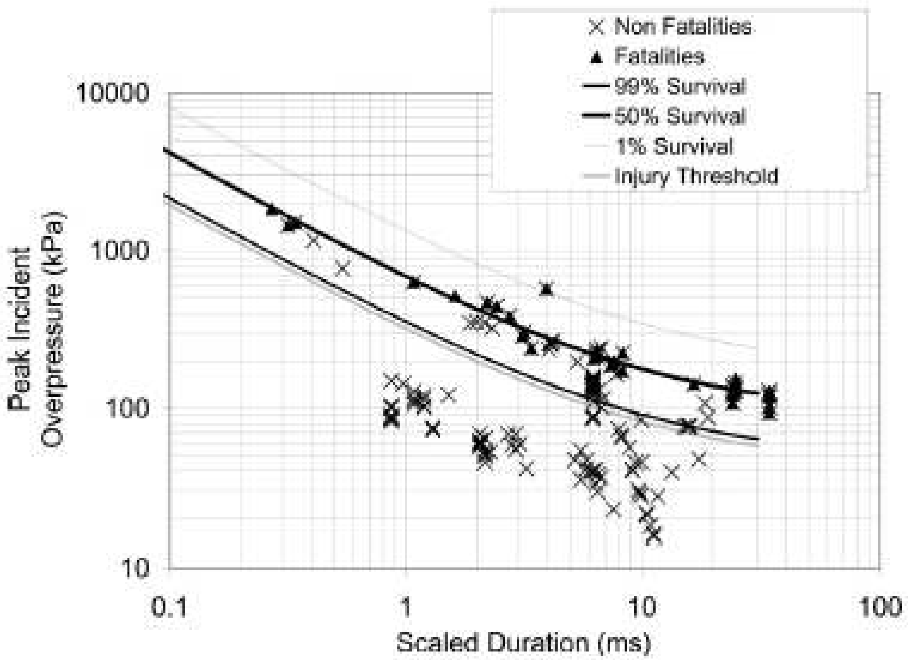

Figure 1-6: Pulmonary injury threshold for humans compiled from animal models (Bass, et al., 2008)

The durations of interest in this figure are shown for 0.25 to 30 milliseconds, but durations pertinent to typical IED blasts are in the middle range. The TNT equivalence charts show a peak pressure and positive duration of 50 psi and 3 milliseconds for an explosive weight of 26 lbs at a distance of 12 feet. This would have a survival level around 50% according to Bass (2008). The loading intensity for mild TBI should have a survival rate near 100%. Larger explosives create longer duration blast profiles, especially at increasing distances. Since 80% of the IEDs used in Afghanistan in December 2009 were larger than 26 lbs and increasing (Dreazen, 2010), the pertinent blast regime for TBI studies is likely greater than 3 milliseconds.

There are three primary theories for primary bTBI mechanisms (Courtney & Courtney, 2010). The first investigates “whether whole-body or local (chest) exposure to blast overpressure can induce ultra-structural, biochemical, and cognitive impairments in the brain” (Cernak, et. al., 2001). This study was carried out by exposing the bodies of rats to blast waves and found that brain impairment occurred. Courtney and Courtney (2010) also studied this phenomenon.

The second theory is based upon the idea that significant head acceleration contributes to TBI. A study of football equipment (Zhang, et al., 2004) showed that translational and rotational acceleration can induce brain injury, with rotational acceleration causing more significant damage. Another study by Finkel (2006) using finite element analysis showed that accelerations induced by blast waves can cause TBI, without the accelerations caused by blunt impact (tertiary injury).

The final theory states that direct transmission of a blast wave induces pressure loading in the brain, leading to traumatic brain injury. One segment of this theory is based upon the idea that significant flexure of the skull occurs leading to damaging loading on the brain cavity (Moss, et al., 2009). Cavitation in fluid filled regions of the brain could also be an injury mechanism induced by direct pressure wave transmission and negative pressure phases leading to localized damage (Wardlaw & Goeller, 2010). The work of Taylor and Ford (2008) showed significant regions of negative pressure that could induce cavitation in the brain. Pressure spikes in localized areas of the brain could be significant enough to cause axonal injury and lead to TBI (Taylor & Ford, 2008). Axonal injury thresholds are typically above pressures that will cause significant brain injury by other mechanisms. This study was done using a very intense (1.3 MPa) shock wave with a short duration (0.6 ms) so the results may only be pertinent at very close distances to small explosives. Rafaels et al. (2010) suggested that different injury mechanisms likely exist for short and long duration blasts, so the incident pulse should be carefully considered.

These TBI inducing theories are likely intertwined, leading to the necessity for complex models that can incorporate and understand many injury mechanisms. The TBI mechanisms discussed are all mechanical, but physiological and psychological issues are also correlated to mild TBI. Further difficulties arise from the need to perform live testing, since scaling issues are a concern when human-related TBI conclusions are drawn from animal testing. For these reasons, the combination of engineering, medicine, veterinary science, psychology, military and other fields must work together to solve the complicated problem of blast induced traumatic brain injury.

1.1.2 Shock Wave Theory

An understanding of shock wave physics is required to accurately perform blast wave experiments. Furthermore, the differences between free-field explosive driven blast waves and shock tube generated blast waves must be understood. A free-field shock wave expands in 3 dimensions, but can be approximated as a planar wave for far-field conditions. Since a shock tube creates a planar 1-dimensional wave, shock tubes can only replicate far-field blast waves, where the shock front can be considered planar.

The governing relations for 1-D shock wave theory are described by the Rankine-Hugoniot equations, which describe property changes across a shock front. The derivation is performed using a control volume shown in Figure 1-7. This figure is drawn for shock tube applications with a moving shock front; derivations for aerodynamics applications are performed using a stationary shock front. The two styles can be correlated using vector addition of the shock and particle velocities. Shock velocity, temperature, pressure, density, and particle velocity are shown for the two states across the shock front. The shock front velocity is shown as U.

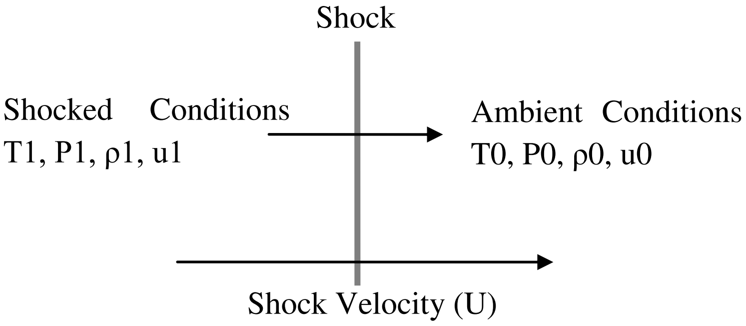

Figure 1-7: Control volume used for derivation of Rankine-Hugoniot jump conditions showing the ambient state (0) and the shocked state (1)

The jump conditions across the shock front contain equations for the conservation of mass, momentum, and energy along with the ideal gas equation of state. The ambient particle velocity is assumed to be zero for shock tube applications.

Conservation of mass:

$$\rho_1(\mathrm{U} - u_1) = \rho_0\mathrm{U} \tag{1.1}$$

Conservation of momentum:

$$\mathrm{P_1 - P_0 = \rho_0 U u_1} \tag{1.2}$$

Conservation of energy:

$$\mathrm{E_1 - E_0} = \frac{1}{2}(\mathrm{P_1 + P_0})\left(\frac{1}{\rho_0} - \frac{1}{\rho_1}\right) \tag{1.3}$$

Equation of State:

$$\mathrm{P_1} = (\gamma - 1)\rho_1\mathrm{E_1} \tag{1.4}$$

A more common form of the shock equations is given by the following equations. These equations assume ideal gas behavior, meaning the specific heats are constant. Since the change in state across a shock front is nearly instantaneous, the process is considered to be adiabatic (negligible heat transfer). The shock velocity is replaced by the Mach number which is equal to the shock velocity divided by the local sound speed as shown in equation 1.5. The local sound speed is equal to the square root of the product of the specific heat ratio, the specific gas constant, and temperature as shown by equation 1.6. The specific heat ratio of air is approximately 1.41 and the gas constant for air is approximately 287 J/(kg*K). Data from these equations are often tabulated in the form of shock tables for quick and convenient analysis, and can be found in most aerodynamics textbooks.

$$\mathrm{M} = \frac{\mathrm{U}}{\mathrm{a}} \qquad (1.5)$$

$$\mathrm{a} = \sqrt{\gamma \mathrm{R} \mathrm{T}_0} \qquad (1.6)$$

$$\frac{\mathrm{P}_1}{\mathrm{P}_0} = \frac{2\gamma \mathrm{M}^2 - (\gamma - 1)}{(\gamma + 1)} \qquad (1.7)$$

$$\frac{\mathrm{T}_1}{\mathrm{T}_0} = \frac{[2\gamma \mathrm{M}^2 - (\gamma - 1)][(\gamma - 1)\mathrm{M}^2 + 2)]}{(\gamma - 1)^2 \mathrm{M}^2} \qquad (1.8)$$

$$\frac{\rho_1}{\rho_0} = \frac{(\gamma + 1)\mathrm{M}^2}{(\gamma - 1)\mathrm{M}^2 + 2} \qquad (1.9\,)$$

A distance-time or x-t diagram demonstrates the shock propagation phenomena inside a shock tube, as shown by Figure 1-8. A typical shock tube consists of a high pressure section (driver section or breech) and a low pressure section (driven section or barrel) which are separated by a rupture membrane. Upon membrane rupture, a shock wave front propagates in the positive direction at a constant shock velocity.

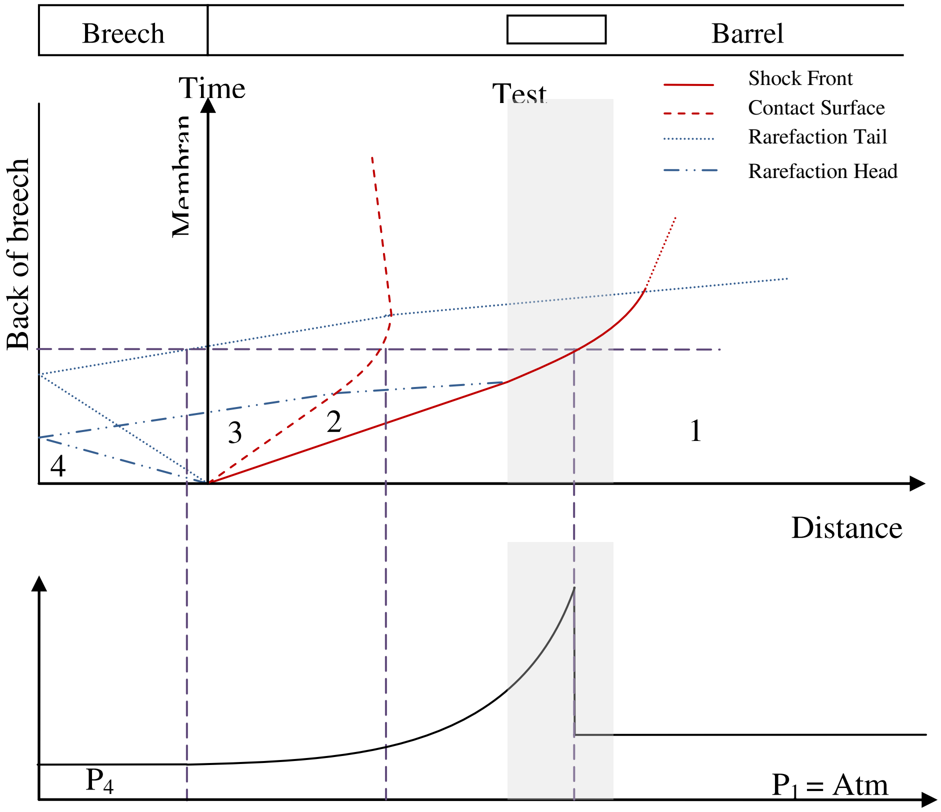

Figure 1-8: Distance-time (X-t) diagram for a shock tube (Holmberg, 2010). The ideal test section is placed so that the breech rarefaction catches the shock front to produce a sharp Friedlander profile shown (bottom).

Simultaneously, an expansion (rarefaction) wave propagates in the opposite direction (negative distance) until it reflects off the back of the breech. Unlike the shock front, the rarefaction wave is continuous with a head and a tail. Since the gas behind the shock front is flowing forward in a compressed state, the rarefaction wave reflected from the back of the breech travels faster than the shock front relative to the laboratory scale. The region behind a shock wave is at constant pressure (flat topped shock wave) until the reflected rarefaction from the breech catches the shock front. At this point the shock wave history will exhibit the characteristics of a sharp Friedlander profile. At further distances from the driver the peak pressure will erode due to the expanding rarefaction wave.

The contact surface is the "surface" where the driver and driven gas meets. The rapidly expanding driver gas causes a significant drop in temperature and density, creating a discontinuity in material properties across the contact surface. Because of this, the rarefaction propagation velocity can change across the contact surface depending on the state/makeup of the driver and driven gases. The shock overpressure does not change across the contact surface, but the reflected pressure could have a significant change due to the density differences. The reflected shock pressure is induced by completely stopping the shock flow, causing the kinetic flow energy to convert to pressure.

Because of the discontinuities across the contact surface, an ideal location to simulate a blast wave would be located after the rarefaction front meets the shock front and beyond the range of the contact surface. Further information concerning ideal test section placement can be found in chapter 5 of this thesis and in Aaron Holmberg's thesis (2010).

After the shock wave reaches the exit of an open ended shock tube, a rarefaction wave travels from the shock tube exit towards the driver section. This characteristic is not shown on the diagram, but can cause significant profile degradation near the shock tube exit. If the shock tube has a closed end, a reflected shock wave will be generated instead of the rarefaction caused by an open ended shock tube. These characteristics are not shown on the wave diagram, but secondary loading from these effects can be a potential concern for blast experiments.

1.2 Research objectives

The overall goal of the shock generation facility is to understand the mechanisms of traumatic brain injury and to minimize their severity/occurrence. The main goal of this thesis is to research fundamental concepts and to provide a stepping stone for further advancements in blast-induced TBI research.

One of the core concepts that needs to be understood is the proper sample placement in shock tubes to replicate the blast waves generated by IEDs, which take the form of a Friedlander wave under free field conditions. This understanding needs to be obtained through experimental data. The development of data measurement and analysis systems is necessary to collect data in a consistent manner. Careful sensor selection and an understanding of their limitations are necessary to provide accurate measurements. An understanding of the fundamental wave propagation modes inside a human head during blast exposure is another goal of this thesis.

A large-scale shock tube must be designed, assembled, and characterized to pave the way for full-scale human head model testing under experimentally simulated blast conditions. The blast profiles need to have the proper intensity, shape, and duration in order to accurately reproduce blast-like conditions.

1.3 Organization of thesis

This thesis consists of six chapters covering various shock wave and TBI-related topics. The key topics of each chapter are mentioned in the following paragraphs.

The first chapter covers background information regarding the motivation for performing blast induced traumatic brain injury research. Literature review outlining previous results was done to obtain a current understanding of TBI research. Information regarding explosive characteristics is also studied to demonstrate typical shock wave loading caused by IEDs. Basic shock wave theory including governing equations and wave diagrams are covered to give an understanding of blast wave physics.

The second chapter describes the methods of collecting and analyzing shock wave data. Operational procedures for the data acquisition and analysis programs are outlined. Sensor information including factory specifications and practical observations are covered to give a concise overview of key operational aspects. The Fiso fiber optic pressure sensors are covered in detail because they produce erroneous results under high loading rates typical of shock exposure.

The third chapter covers the experimental analysis of a simplified head model to assist in a fundamental understanding of the wave propagation modes within a human head. Surface strain and pressure are compared to internal pressure to determine potential causes of various loading phenomena within a human head.

The fourth chapter investigates the surface pressure loading applied to a rigid cylinder placed at various locations inside and outside a 9 inch square shock tube to determine the ideal sample placement for simulated blast wave experiments. Pressure and impulse profiles as well as planarity testing are used for comparison. The loading on the cylinder at various orientations was also studied.

Chapter five covers the design and characterization of a large-scale shock tube for performing large-scale blast testing. The design is modular for relatively simple tuning to produce a variety of shock profiles. Characterization testing was done to determine empirical relations between burst pressure, peak overpressure, and positive impulse. The actual shock profiles are also shown to emphasize details of the generated blast waves.

The final chapter sums up the results obtained from each chapter. A list of recommended future experiments is given to provide guidance for future work to be done at UNL's experimental blast wave simulation facility.

Chapter 2: Shock Tube Technique for Blast Wave Simulation

This chapter describes the data acquisition and data analysis methods. Key aspects of the data acquisition hardware and software are covered as well as specifications, advantages, and disadvantages of various types of sensors. Much of the chapter is devoted to describing operational procedures and technical data, but a significant portion also covers the limitations of using Fiso optical pressure sensors under shock loading conditions. Proper mounting of piezoelectric pressure sensors is also covered.

2.1 Data acquisition and analysis system

The data acquisition and analysis system implements hardware from National Instruments as well as LabVIEW software for data collection and analysis. The following section describes system hardware design characteristics, as well as the features of the in-house written LabVIEW programs.

2.1.1 Hardware

The hardware chosen for the data acquisition system was selected primarily from National Instruments, with the exception of the trigger sensor, remote desktop computer, and pressure/strain sensors. A schematic of the flow of data through the various components is shown in Figure 2-1. Further details about the flow of information through these components are outlined in the following sections.

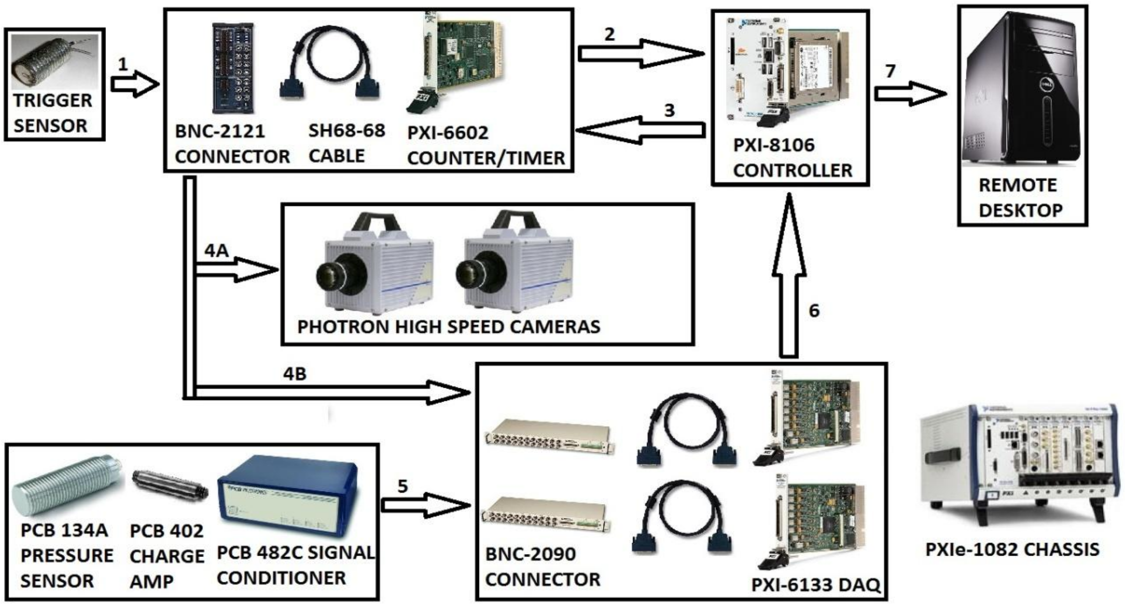

Figure 2-1: Schematic of data acquisition process: 1) Trigger sensor sends digital pulse to counter. 2) Counter relays signal to controller. 3) Controller instructs counter to send timed pulses. 4) Counter sends timed trigger pulses to cameras and DAQ. 5) Upon receiving trigger, DAQ collects prescribed data. 6) Data is sent to the controller module. 7) Data can be viewed in the control room via remote desktop.

2.1.1.1 Trigger sensors

The use of the trigger sensors was implemented to begin collecting data before the shock wave reaches the experiment in the shock tube. They are inexpensive and provide the digital pulse which tells the counter of shock wave arrival, but pressure data is not collected from the trigger. Two types of trigger sensors are outlined in the following sections.

2.1.1.1.1 Piezoelectric trigger

The first method of triggering the data acquisition system is with a handmade sensor which is resistant to electromagnetic noise, simple to fabricate, inexpensive, and does not require a power supply. The trigger simply consists of a piezoelectric element, a Zener diode, and a resistor, which can all be purchased from Digi-Key Corporation, or another similar electronics supplier. A schematic, the individual components, and a completed trigger sensor are shown in Figure 2-2.

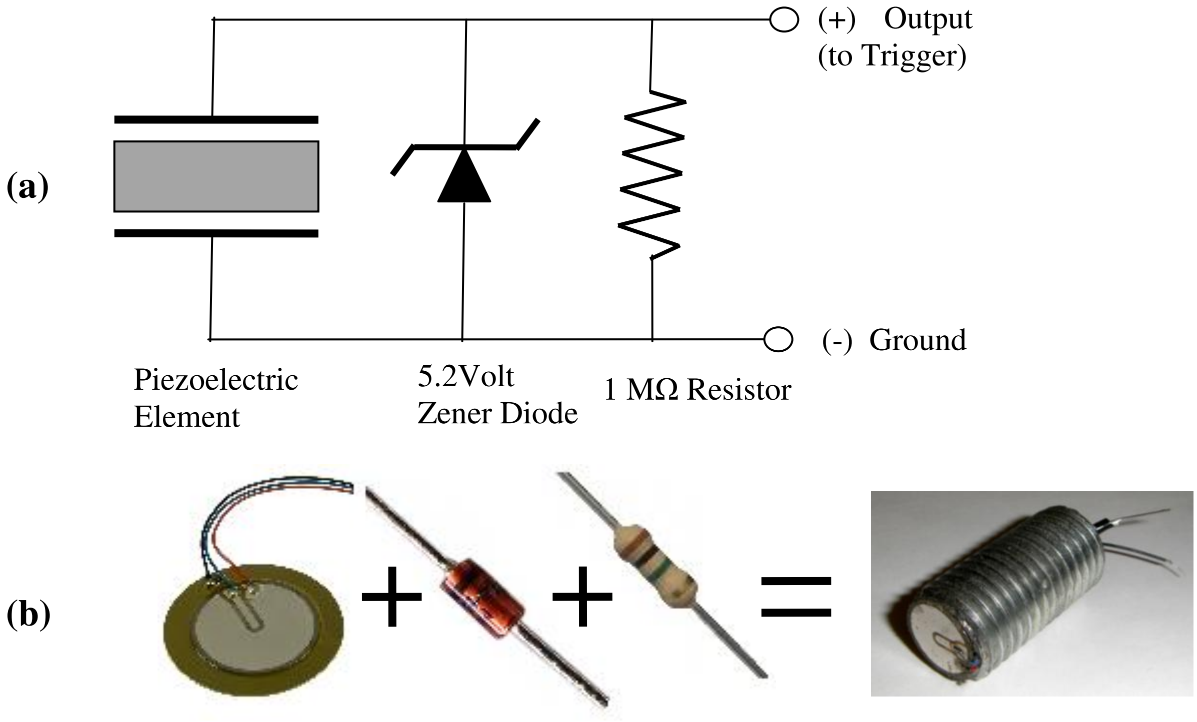

Figure 2-2: (a) Trigger sensor electrical wiring schematic. (b) Trigger sensor components fully assembled.

The piezoelectric element generates a charge which is seen at the output terminals. A Zener diode is used to limit the voltage to 5.2 volts and a resistor is used to prevent charge buildup. The components are contained using a length of ¾ inch threaded rod with a ½ inch diameter hole through the center. The positive terminals were brought through a small groove at the tip of the housing and the negative terminals were soldered to the brass backing of the piezoelectric element. The element was glued on with epoxy but was not back filled, since flexure of the element produces much of the voltage output. The tip of the sensor is mounted flush with the shock tube surface, and creates a charge when dynamic pressure is applied. This sensor does not typically cross the digital threshold (~3 volts) for shock wave intensities below 10-15 psi, so a charge amplifier can be applied to the circuit for low pressure shots.

2.1.1.1.2 Metallic silk screen trigger

Another trigger sensor was developed in our lab by Aaron Holmberg which uses a small metallic screen (silk screen) to switch the trigger as a shock wave passes. A schematic and an image of the sensor are shown in Figure 2-3. The two terminals of the switch are composed of a piece of metallic silk screen and a piece of wire which is bent over the screen. Air flow over the screen causes it to flex and contact the wire which sends a digital signal to the trigger on the pulse generator/delay box. A resistor is used to prevent excessive current flow and battery depletion.

This sensor is sensitive to low pressure shock waves and has been used successfully. One of the disadvantages is that the system will not function if the power supply is depleted or turned off. The battery power supply can be depleted if the switch closes and does not spring back open. The timing of this trigger is also less consistent than the piezoelectric type.

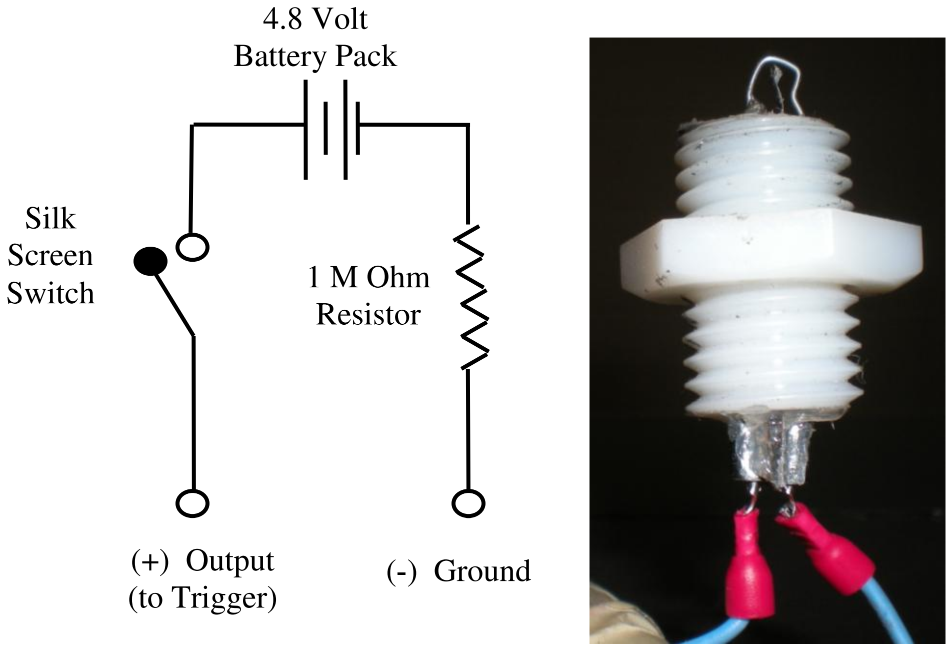

Figure 2-3: Wiring diagram and image of a silk screen trigger switch

2.1.1.2 Pulse generating counter/delay box

The pulse generating counter receives a signal from the trigger sensor and sends out digital pulses to start the data recording devices, such as the DAQ and high speed cameras. The counter is a National Instruments PXI-6602, which uses the BNC-2121 connector block and a shielded SH68-68-EPM cable. The digital pulse generator can either send out synchronized pulses to the various data collection systems or act as a delay box to generate the pulses at prescribed intervals. The counter could be bypassed and the trigger could be sent directly to the recording instruments, but the system was set up for flexible configurations for timed trigger pulses. The delay function is not typically used in shock experiments, though.

2.1.1.3 DAQ

Experimental data is collected using two National Instruments PXI-6133 data acquisition cards, which have 8 analog channels each. These DAQs are capable of 14 bit sampling at up to 2.5 MHz, although 1 MHz is typical for most experiments. They also have a built in memory storage of up to 32 million data points per channel (32 seconds at 1 MHz sampling rate). The analog inputs are connected through BNC-2090 panel mounted connector blocks and a 68 pin SH68-68-EPM cable. The DAQ cards are mounted inside the chassis, similarly to the 6602 counter.

2.1.1.4 System controller and chassis

Computations and data transfer are done through the controller module, which is model PXIe-8106. The controller is basically a computer system which consists of a dual core 2.16 GHz processor, 1 GB of RAM, Windows Vista operating system, and a 60 GB hard drive. Communication with the data acquisition system is performed using an Ethernet connection and a remote desktop computer located in the control room.

The housing for all of the components is a PXIe-1082 chassis, which has 7 slots for holding various PXI modules as well as the controller. There are currently 4 open slots in the chassis, allowing for future expansion if necessary.

2.1.2 Software

LabVIEW is a graphical programming language that is easily implemented for data acquisition, control systems, and data analysis. Two programs were written using LabVIEW to aid in the collection and analysis of data, and are outlined in the following sections. A shock tube control program which is also written with LabVIEW can be viewed in Aaron Holmberg's MS thesis (2010).

2.1.2.1 Data acquisition program

The data acquisition program was developed for recording experimental data in a consistent and easily analyzed format. The software collects data, applies sensor calibrations, and saves important experimental parameters. Further details are given in the following sections.

2.1.2.1.1 Inputs tab

A screen shot of the "Inputs" tab of the data acquisition program is shown in Figure 2-4. This tab is used for selecting sample parameters such as rate, sensor selection, trigger timing, and more.

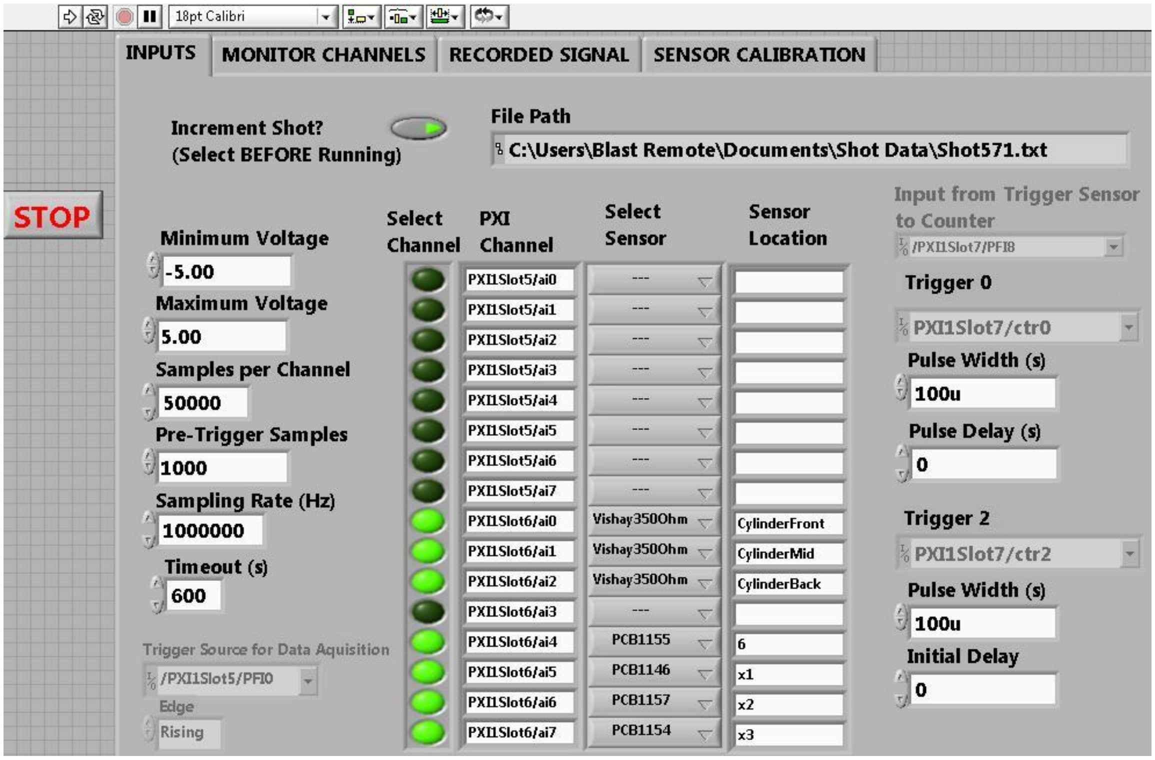

Increment Shot? (Select BEFORE Running)

File Path: C:\Users\Blast Remote\Documents\Shot Data\Shot571.txt

Minimum Voltage: -5.00

Maximum Voltage: 5.00

Samples per Channel: 50000

Pre-Trigger Samples: 1000

Sampling Rate (Hz): 1000000

Timeout (s): 600

Trigger Source for Data Aquisition: /PXI1Slot5/PFI0

Edge: Rising

Select Channel	PXI Channel	Select Sensor	Sensor Location
○	PXI1Slot5/ai0	---	
○	PXI1Slot5/ai1	---	
○	PXI1Slot5/ai2	---	
○	PXI1Slot5/ai3	---	
○	PXI1Slot5/ai4	---	
○	PXI1Slot5/ai5	---	
○	PXI1Slot5/ai6	---	
○	PXI1Slot5/ai7	---	
●	PXI1Slot6/ai0	Vishay350Ohm	CylinderFront
●	PXI1Slot6/ai1	Vishay350Ohm	CylinderMid
●	PXI1Slot6/ai2	Vishay350Ohm	CylinderBack
○	PXI1Slot6/ai3	---	
●	PXI1Slot6/ai4	PCB1155	6
●	PXI1Slot6/ai5	PCB1146	x1
●	PXI1Slot6/ai6	PCB1157	x2
●	PXI1Slot6/ai7	PCB1154	x3

Input from Trigger Sensor to Counter: /PXI1Slot7/PFI8

Trigger 0: PXI1Slot7/ctr0

Pulse Width (s): 100u

Pulse Delay (s): 0

Trigger 2: PXI1Slot7/ctr2

Pulse Width (s): 100u

Initial Delay: 0

Figure 2-4: Data acquisition program: "INPUTS" tab

Before running the data acquisition program the button labeled "Increment Shot?" must be set to the desired state. It has a default value of ON. When this button is on, the output file is named "Shot###.txt," where ### is a number incremented with each consecutive shot. Each time a shot is incremented, a file named "ShotList.txt" is updated to show the entire list of recorded shots. If the "Increment Shot?" button is off the file will be saved as "Default.txt," and the file must be renamed before another shot is fired because the program will overwrite existing files. After this selection is made, the program can be started by pressing the run button (shown as an arrow) located in the upper left hand side of the screen.

The voltage range for the data collection can be adjusted from -10 to +10 volts by using the voltage inputs. A total number of samples are selected using the "Samples per Channel" input. Although the relevant data for a shock wave experiment is typically less than 10 milliseconds, 50,000 samples is typical for most experiments. These extra points ensure that the complete event is captured and also show any reflections/rarefactions that occur from the shock tube end configuration. A preset number of samples are taken before the trigger sensor is switched, which is set using the "Pre-Trigger Samples" input. This establishes a clean baseline without interference caused by stress waves in the shock tube, which travel faster than the shock front. A sampling rate of up to 2.5 MHz can be selected using the "Sampling Rate" input, although 1 MHz is usually sufficient for most shock wave experiments.

The chassis houses two 6133 DAQ cards with 8 channels per DAQ. The available channels are listed in an array labeled "PXI Channel," and channel selection is done using the "Select Channel" array of buttons. There is also an array with pull-down lists for selecting a sensor for each channel. This pull-down list labeled "Select Sensor" contains the serial numbers of many sensors, and selections are made for each active channel. The sensor location is also recorded using a write-in array labeled “Sensor Location.” Since it is write-in, other experimental notes can be added to this spot as well.

The hardware schematic in Figure 2-1 shows a trigger pulse being sent from the counter module to the DAQ and cameras. The "Trigger 0" slot is reserved for triggering the DAQ, but three more are available for triggering other systems (only two are shown in the figure). The trigger pulse duration and delay time can be adjusted for each trigger, which corresponds to an output pin on the digital counter.

2.1.2.1.2 Monitor channels tab

After all inputs have been selected, the "Monitor Channels" tab shown in Figure 2-5 should be opened. The graph shows real time data from all sensors, measured at 10 kHz. These signals do not have calibrations applied, which allows the user to easily monitor noise level and troubleshoot problems before firing the shock tube. Sensors typically have a slight DC voltage offset, as shown on the figure. There is also a summary of the selected channels, selected sensors, sensor calibrations, sensor locations, and the average value of each signal shown on the right hand side of the screen. When a shot is ready to be fired, the "Look for Trigger" button should be pressed, causing the large light next to the button to turn bright green. The system is now armed and looking for a signal from the trigger. Upon receipt of the trigger signal the light changes to red which alerts the user that the system was triggered. The "Processing Data" light will activate while processing and turn off when the data is saved causing "Data Saved" to light up.

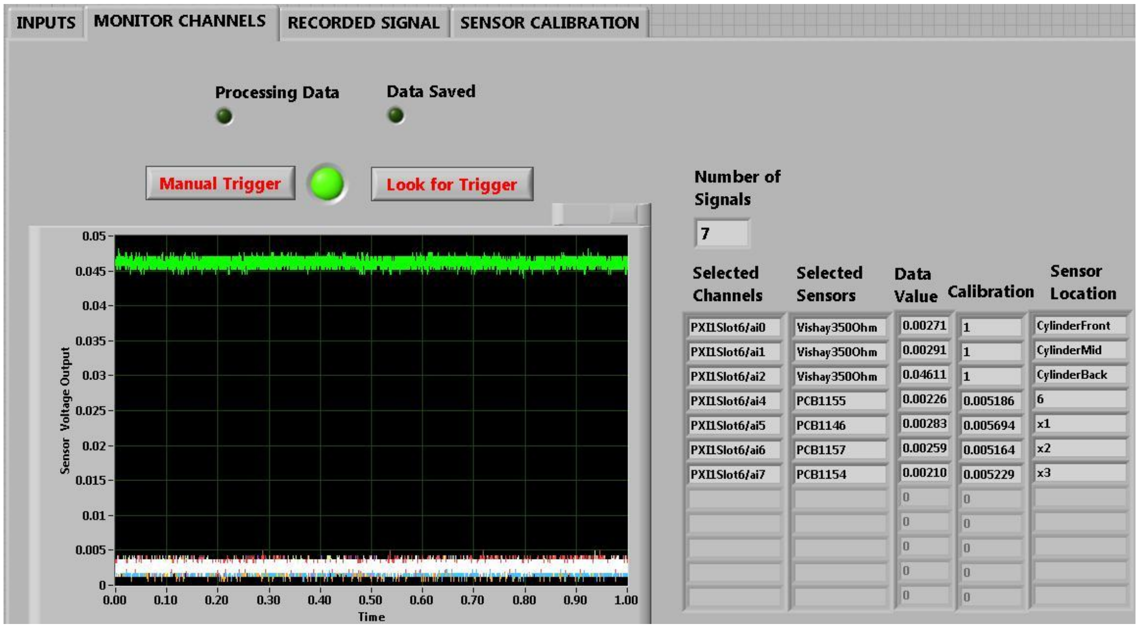

Number of Signals: 7

Selected Channels	Selected Sensors	Data Value	Calibration	Sensor Location
PXI1Slot6/ai0	Vishay350Ohm	0.00271	1	CylinderFront
PXI1Slot6/ai1	Vishay350Ohm	0.00291	1	CylinderMid
PXI1Slot6/ai2	Vishay350Ohm	0.04611	1	CylinderBack
PXI1Slot6/ai4	PCB1155	0.00226	0.005186	6
PXI1Slot6/ai5	PCB1146	0.00283	0.005694	x1
PXI1Slot6/ai6	PCB1157	0.00259	0.005164	x2
PXI1Slot6/ai7	PCB1154	0.00210	0.005229	x3
		0	0	
		0	0	
		0	0	
		0	0	
		0	0	

Figure 2-5: Data acquisition program: "MONITOR CHANNELS" tab

During the data processing phase, the DC baseline offset is calculated, and the signal baseline is adjusted to zero. Then the appropriate calibration value is applied to each sensor. These actions greatly reduce redundant calibration procedures required after a shot. Then the data are saved, the program is automatically stopped, and the data are ready for viewing. The format of the data is stored in a text file which contains the sensor data as well as a record of the user inputs, shock wave arrival time, and DC voltage offset.

2.1.2.1.3 Recorded signal tab

The recorded signal tab has a single graph which shows the calibrated profiles of the recorded data. This tab is not meant for detailed viewing of data but allows the user to quickly ensure that the expected data were collected. Detailed viewing and analysis of data are intended to be done using the data analysis program.

2.1.2.1.4 Sensor calibration tab

The sensor calibration tab shown in Figure 2-6 contains a list of sensors used in the shock facility along with their corresponding calibration value. Sensors with a linear voltage to pressure relation have their appropriate linear calibration listed in this tab. Non-linearly calibrated sensors could have a calibration value set to unity, yielding a pure voltage output requiring further analysis.

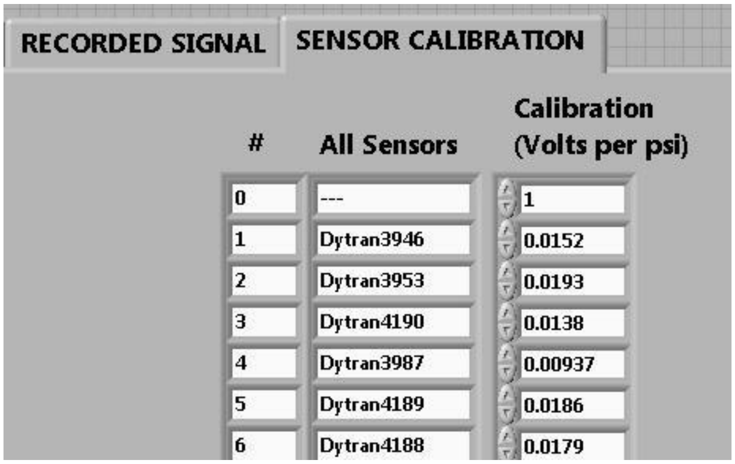

#	All Sensors	Calibration (Volts per psi)
0	---	1
1	Dytran3946	0.0152
2	Dytran3953	0.0193
3	Dytran4190	0.0138
4	Dytran3987	0.00937
5	Dytran4189	0.0186
6	Dytran4188	0.0179

Figure 2-6: Data acquisition program: "SENSOR CALIBRATION" tab

When the list of sensors in the "Sensor Calibration" tab is updated, the "Select Sensor" list in the "Inputs" tab must also be updated in the same numerical order to ensure that the proper calibration values are applied to the correct sensors. Failure to do this will cause the incorrect sensor calibrations to be applied.

2.1.2.2 Data analysis program

Programs like Microsoft Excel can be used for graphing data, but graphing with LabVIEW is often faster, especially when large amounts of data are dealt with. Microsoft Excel 2007 is limited to 32000 data points per series in a chart (Microsoft Corporation, 2011), and the processing time can be extensive. Although LabVIEW can provide faster graphing, some programming is required. However, this can be advantageous since the program can be adapted to user requirements.

A data analysis program was written in LabVIEW for rapid data viewing and analysis. There are four sections to the data analysis program: Open File, Signal Analysis, Save Filtered Profile, and File Data tabs. The following sections describe the operations and features of each in detail.

2.1.2.2.1 Open file tab

Before running the data analysis program a file path must be selected. Since most shots are saved by shot number in a common directory, a file path can be selected based entirely on the shot number. Selecting a particular shot is done by using the "Shot Number" selection, and running the program. The sampling frequency, number of channels, and the number of samples per channel are automatically determined from the file and displayed. The program can be stopped at any time using the "STOP" button located on the left side of the user interface.

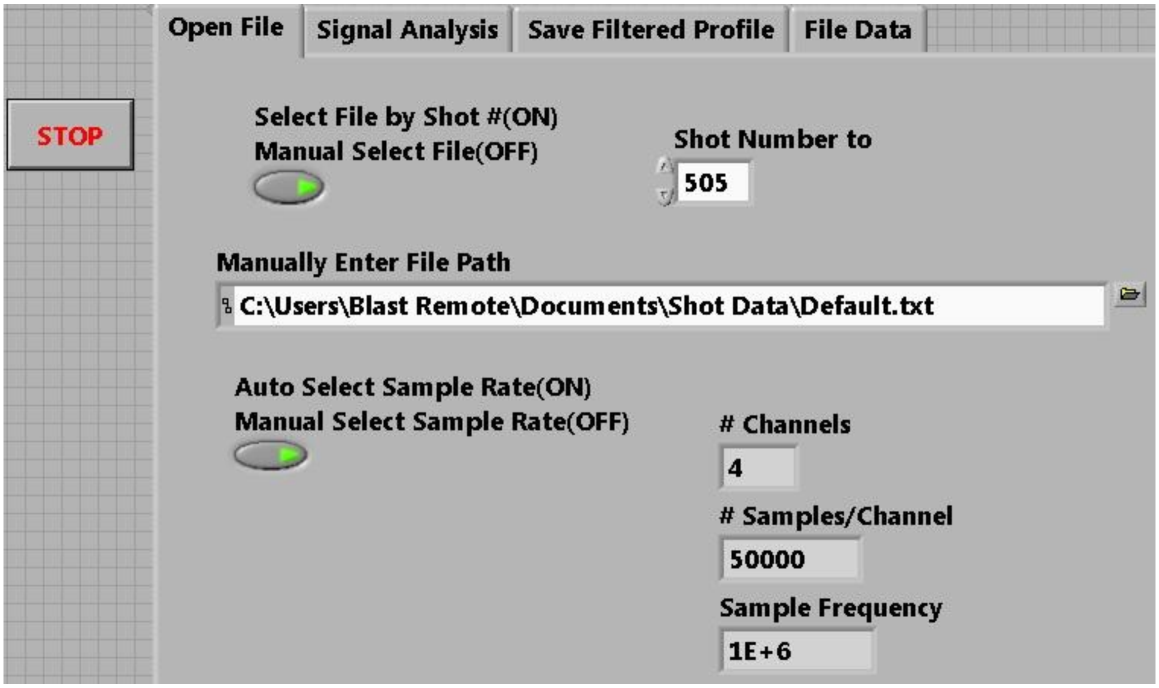

Select File by Shot #(ON)
Manual Select File(OFF)

Shot Number to: 505

Manually Enter File Path: C:\Users\Blast Remote\Documents\Shot Data\Default.txt

Auto Select Sample Rate(ON)
Manual Select Sample Rate(OFF)

Channels: 4

Samples/Channel: 50000

Sample Frequency: 1E+6

Figure 2-7: Data analysis program: "Open File" tab

If the desired file is not named after a particular shot, the "Manual Select File" button must be turned off. The URL entered in the file path will be opened. The sampling frequency may not be detected when manually selecting a file, so the "Manual Select Sample Rate" button can be used to enter the appropriate sampling rate.

2.1.2.2.2 Signal analysis tab

The signal analysis tab has a variety of options which were developed specifically for analyzing shock wave profiles, but can be implemented for other purposes as well. There are two graphs showing the data in a time domain, and a third which shows the Fourier transform (FFT) of a given profile in the frequency domain.

The first graph shown in Figure 2-8 shows a single profile which is selected using the "Select Profile" indexer. The start time and the duration are adjusted using the "Start Time" and "Graph Duration" indexers. The adjustment increments can be set using the

"Start Increment" and "Duration Increment" indexers. For example, an incremental rate set at -3 adjusts the time interval by 0.001 (10^{-3}) seconds. When the data were collected, an approximate arrival time was determined at 25% of the peak signal value. Pressing the "Go to Arrival Time" button will shift the start of the graph to this time allowing the user to adjust a graph to the shock front quickly. This feature works consistently for rapid rising profiles, but is not as effective for slow rising signals.

The impulse under a curve is automatically calculated and displayed in the "Impulse" output box. The calculated impulse is graphically represented by the area under the first graph in Figure 2-8 with the negative regions subtracted. When calculating the peak overpressure of a shock wave the average value of several points is used, especially for sensor calibration using flat-topped shock waves. The "# Points Averaged" selection adjusts the number of points to average after the start time of the first graph. The average is shown in the "Average Value" display box, and a cursor graphically indicates the average value and the duration of the averaging.

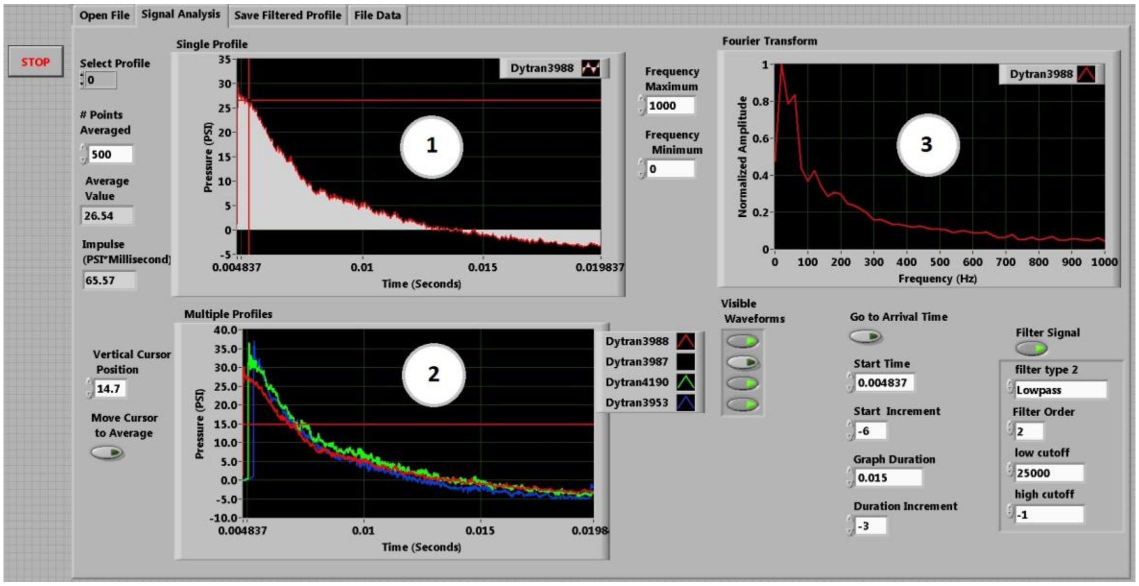

Select Profile: 0
Points Averaged: 500
Average Value: 26.54
Impulse (PSI*Millisecond): 65.57
Vertical Cursor Position: 14.7
Frequency Maximum: 1000
Frequency Minimum: 0
Start Time: 0.004837
Start Increment: -6
Graph Duration: 0.015
Duration Increment: -3
filter type 2: Lowpass
Filter Order: 2
low cutoff: 25000
high cutoff: -1

Figure 2-8: Data analysis program: Signal Analysis tab

The second graph in Figure 2-8 shows multiple waveforms simultaneously. Displayed waveforms can be selected using the "Visible Waveforms" array of switches, which simultaneously adjusts the legend on the right of the graph. The scaling of the horizontal axis of this graph is scaled identically to graph 1, but the vertical axis is scaled automatically for all signals. When comparing waveforms on this graph, it is sometimes useful to compare signals to a given value. For this reason the cursor on graph 2 can be adjusted with the "Vertical Cursor Position" control, which can be automatically set to the average value computed for graph 1.

Graph 3 shows the Fourier transform of the selected profile in graph 1 and is normalized to have a peak value at unity. The frequency range can be adjusted from zero to half of the sampling frequency using the "Frequency Maximum" and "Frequency Minimum" controls. The frequency increment between points is equal to the sampling frequency divided by the number of samples taken. This analysis tool is useful for observing the main frequencies present in a signal. The largest frequency peak of a shock wave is at a low frequency, but minor spikes can also show high frequency components, noise, and resonant frequencies of sensors.

Undesired high frequency noise based on sensor dynamics does not necessarily represent part of an actual shock wave signal, and can be reduced using filtering techniques. A filtering algorithm was implemented to remove unrepresentative frequencies (noise). Several filter types are available including the low-pass, high-pass, and band-pass, but the low-pass filter is used almost exclusively. Filtering can be turned on or off using the "Filter Signal" button. The filter characteristics (type, order, and cutoff frequencies) can be selected using the controls below the “Filter Signal” button.

Using a low-pass filter with a cutoff of 25 kHz cleans up a shock wave profile significantly, with less than 0.1% decrease in calculated impulse.

2.1.2.2.3 Save filtered profile tab

Filtered shock wave profiles can be successfully used as inputs to finite element simulations such as ABAQUS, without introducing unrealistic noise created by the imperfect pressure sensor dynamics. Filtering of a signal does not change the data in the original file, so the capability to save filtered data was created. The "Select Profile" control in the "Signal Analysis" tab determines which filtered profile will be saved. The "Write Filtered Signal File" should be pressed and held until a prompt opens to enter a file path and name. Clicking "OK" saves the filtered profile in a separate text file which can be imported into other programs.

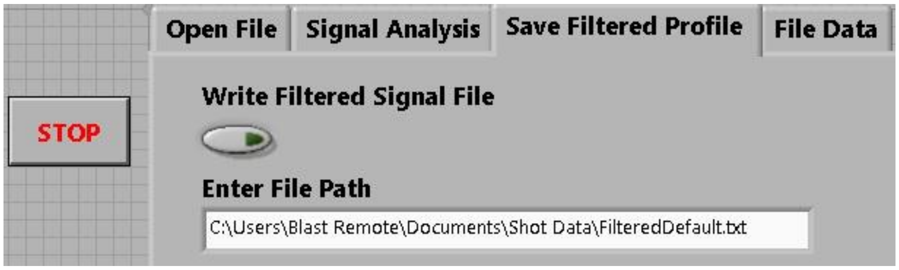

Enter File Path

C:\Users\Blast Remote\Documents\Shot Data\FilteredDefault.txt

Figure 2-9: Data analysis program: Save Filtered Profile tab

2.1.2.2.4 File data tab

The “File Data” tab contains an array with data from the opened text file in tab delimited format. The starting points of the array can be adjusted using the arrows on the upper right of the array. All of the user inputs are contained in this array, as well as the approximate arrival time, DC offset before shifting, and the shot data (pressure, strain, etc.). An example showing the information in this tab is shown in Figure 2-10.

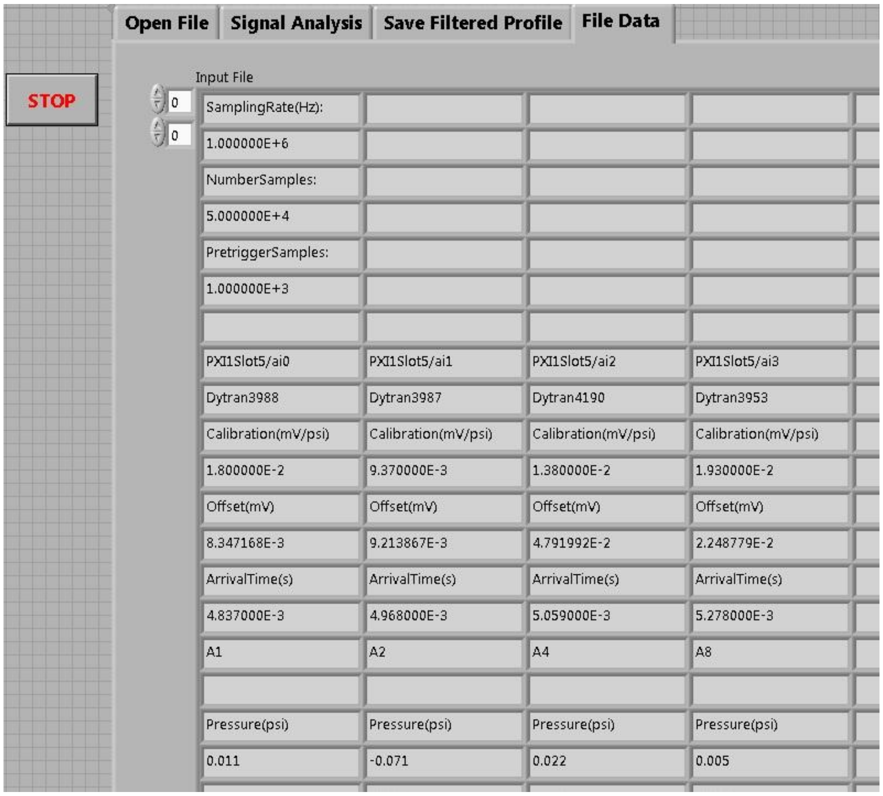

SamplingRate(Hz):			
1.000000E+6			
NumberSamples:			
5.000000E+4			
PretriggerSamples:			
1.000000E+3			
PXI1Slot5/ai0	PXI1Slot5/ai1	PXI1Slot5/ai2	PXI1Slot5/ai3
Dytran3988	Dytran3987	Dytran4190	Dytran3953
Calibration(mV/psi)	Calibration(mV/psi)	Calibration(mV/psi)	Calibration(mV/psi)
1.800000E-2	9.370000E-3	1.380000E-2	1.930000E-2
Offset(mV)	Offset(mV)	Offset(mV)	Offset(mV)
8.347168E-3	9.213867E-3	4.791992E-2	2.248779E-2
ArrivalTime(s)	ArrivalTime(s)	ArrivalTime(s)	ArrivalTime(s)
4.837000E-3	4.968000E-3	5.059000E-3	5.278000E-3
A1	A2	A4	A8
Pressure(psi)	Pressure(psi)	Pressure(psi)	Pressure(psi)
0.011	-0.071	0.022	0.005

Figure 2-10: Data analysis program: File Data tab

2.2 Data measurement sensors

Many different types of measurements are taken during shock wave experiments. Piezoelectric, piezoresistive, and fiber optic sensors were commonly used for pressure measurements, while strain gauges and high speed cameras were used for strain and displacement visualization. Each type of gauge has advantages and disadvantages which will be discussed specifically for each type of sensor in the following sections.

2.2.1 Piezoelectric pressure sensors

Dynamic pressure measurements are often taken using piezoelectric pressure sensors because of their microsecond rise time and high resonant frequencies (PCB Piezotronics, 2009). They are well suited for dynamic measurements, but the charge buildup in the piezoelectric crystal will eventually decay to zero based upon a specified time constant. An entire shock wave event typically takes place in less than 20 milliseconds so the discharge time constant should not have a significant effect on the piezoelectric sensors used in the UNL shock facility.

The typical construction of a piezoelectric sensor is shown in Figure 2-11. The sensing elements can be made of any piezoelectric element but are primarily quartz or tourmaline. The sensing elements are isolated using a diaphragm and are preloaded to avoid tensile stresses in the brittle sensing element. Due to the low current capability of the piezoelectric element, a charge amplifier is used to convert the high impedance charge into a low impedance voltage output. The charge amplifier can be built into the sensor or it can come as an external component. They typically have acceleration compensation built into the sensor to minimize false measurements caused by sensor oscillation. All of these components are contained within a threaded metallic housing for protection and simple mounting. More information about the piezoelectric sensors in general can be obtained from PCB Piezotronics Inc.

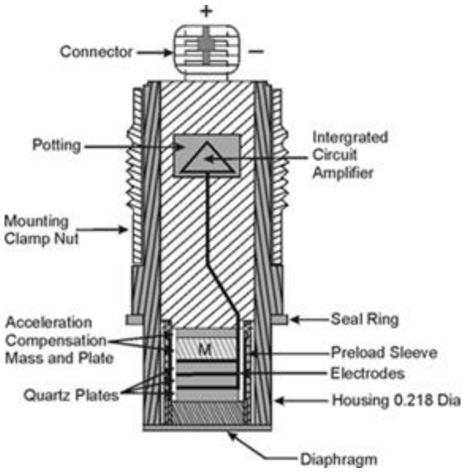

Figure 2-11: Typical components of a piezoelectric pressure sensor (PCB Piezotronics, 2009)

2.2.1.1 Dytran pressure sensors

The first type of piezoelectric pressure sensor is the Dytran model 2300V1 which is used in combination with the four channel 4114B1 signal conditioner. These pressure sensors have a pressure range of 0 to 250 psi with an advertised resonant frequency of 500 kHz (Dytran Instruments, 1996). The sensor is acceleration compensated but it is not impervious to the effects. It has an advertised acceleration sensitivity of 0.001 psi/g with a maximum loading of 5000 g's. These have an integrated charge amplifier which gives the sensor low output impedance. The sensor diaphragm has a diameter of 0.216". Further technical information about these sensors can be found at the Dytran website.

These sensors have proven to be effective for measuring shock wave profiles, but in-house calibration must be done because factory calibrations are not typically accurate. Detailed calibration procedures can be found in Aaron Holmberg's thesis (2009). Large oscillations are present at the shock front due to inadequate damping making it difficult to determine peak overpressures. Filtering or averaging is typically done to determine peak overpressures in signals with large oscillations.

2.2.1.2 PCB pressure sensors

The PCB model 134A24 pressure sensors use a tourmaline piezoelectric sensing element and are used in conjunction with an external PCB 402A charge amplifier and a PCB 482C signal conditioner. This particular model has an operating range from 0 to 1000 psi and has an advertised response time of 0.2 microseconds. They have a resonant frequency above 1.5 MHz, and a time constant greater than one second (PCB

Piezotronics, 2003). They come with vinyl tape placed over the sensing diaphragm to insulate the tip from flash temperatures, present at a shock front due to compression.

These sensors typically produce very clean shock wave profiles that do not require filtering, and have very fast rise times. The factory calibrations are consistent with shock wave experiments, making them ready to use out of the box. These sensors are also very easy to install due to the ½-20 all-thread design. They are larger than the Dytran sensors, but the time for a shock wave to cross a parallel sensing element is approximately 10 microseconds yielding little difference in resolution.

The PCB 134A sensors have many advantages over the Dytran sensors, but the initial cost is significantly higher. Also, the built in acceleration compensation does not consistently mitigate noise caused by high frequency oscillations imparted by the flexing shock tube. Acceleration compensation is built into the sensors but the longevity/degree of that feature may be limited. The susceptibility of sensors to acceleration can be crudely tested for by simply shaking the sensor and recording the intensity of the output signal. A sensor unaffected by acceleration would not have any voltage changes, while one with poor acceleration compensation would have large voltage spikes. These sensors are also susceptible to edge loading which is caused by squeezing the tip of the sensor. This effect can be reduced by using the proper mounting hole (0.453 inch thru; ½-20 UNFB tap (PCB Piezotronics, 2003)) and minimizing flexure at the mounting location.

Figure 2-12 shows an example of an irregular shock wave profile measured by a PCB sensor mounted in the thin side wall of the 28-inch shock tube. This odd behavior is caused by the flexure of the 28-inch shock tube causing oscillation as shown by a strain gauge. Strains in other directions could cause significant oscillations as well, but were not recorded. There is a noticeable disturbance before the shock front arrival, which is due to longitudinal stress waves traveling in the shock tube faster than the shock front. Essentially, the pressure sensor in the thin wall could be measuring a combination of pressure, acceleration, and edge loading. These measurement errors can be avoided by mounting the sensors in a thick plate to reduce flexing and edge loading.

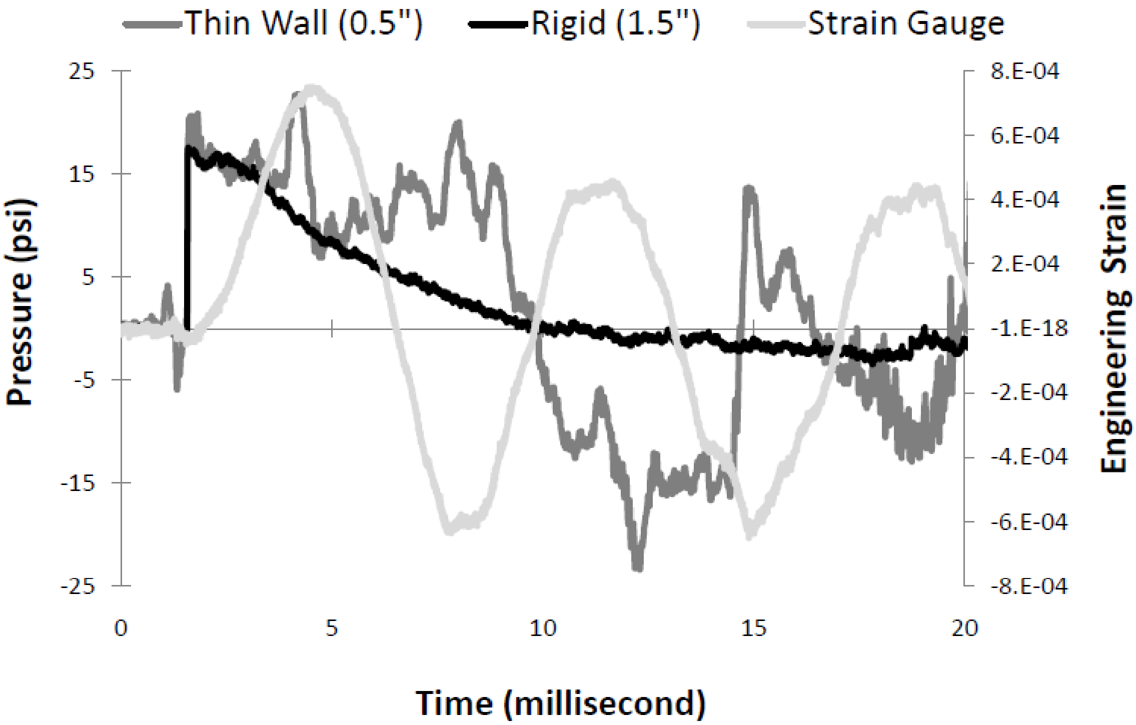

Figure 2-12: Comparison of shock wave profiles measured with rigidly mounted PCB sensor vs. sensor in thin wall. Deviation is due to sensor acceleration shown by strain data.

2.2.2 Fiso pressure sensors using Fabry-Pérot interferometer

Fabry-Pérot interferometer pressure sensors use an optical technique that allows very small sensors to be manufactured. They have been successfully used to measure pressure with minimally invasive techniques, they are impervious to electromagnetic radiation, and they can be used in medical and corrosive environments (Physics Animations). These characteristics make this sensor type appealing for performing tests within a conductive liquid medium when small sensor size is necessary. In the past they have successfully been used in biological samples such as rats and tested under blast conditions of 40 kPa (Chavko, et al., 2007). However, significant measurement errors are seen under high frequency, high pressure loading.

2.2.2.1 Theory of operation

The Fabry-Pérot interferometer method is illustrated in Figure 2-13. The system consists of a light generating diode which transmits light through the fiber optic cable to a mirror at the end of the sensor cavity. The light is reflected by the mirror and transmitted back to a photo detector. Translation of the mirror will cause the light intensity to change based on the degree of constructive or destructive interference.

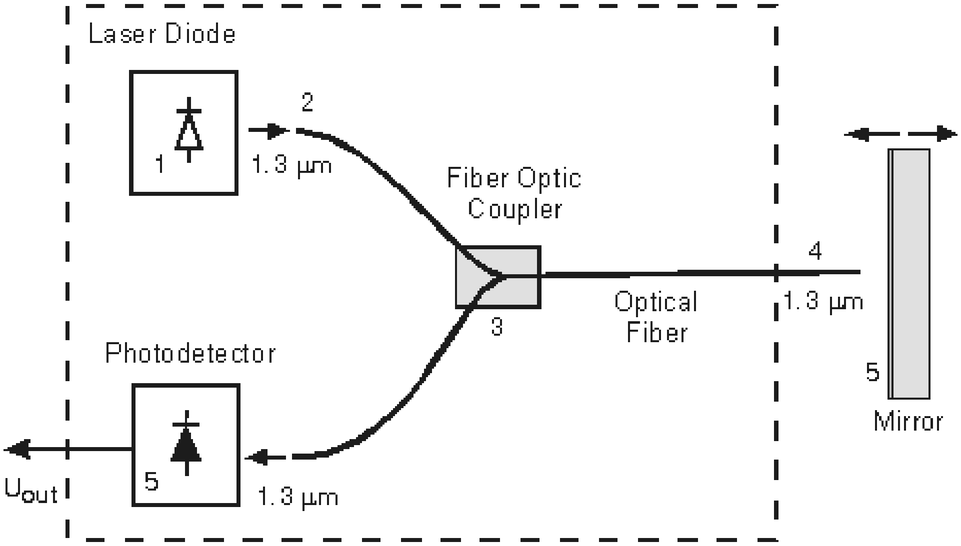

Figure 2-13: Fabry-Pérot interferometer concept diagram (Physics Animations)

Changes in light intensity can be directly correlated to the displacement of the mirror, and is described by equation 2.1.

$$I = 2I_0\left(1 + \cos\left(\frac{4\pi}{\lambda}x_0 + \varphi_0\right)\right) \qquad (2.1)$$

$I_0 = Initial\ Light\ Intensity$

$\lambda = Light\ Wavelength$

$x_0 = Initial\ Mirror\ Position$

$\phi_0 = Initial\ Phase\ Angle$

Based on this equation a full period of intensity is equal to half of the wavelength (λ/2) of light. In the case that both positive and negative displacement is measured (i.e. ± pressure changes), the maximum resolution for a measurement becomes ± λ/4. In the event that the displacement exceeds this range, the light intensity will repeat causing the true value to be unknown.

Figure 2-14 shows a simplified schematic to describe this phenomenon, although it is actually more complicated because a spectrum of light is used instead of a single frequency. Figure 2-14A demonstrates an initial state of the Fabry-Pérot cavity with constructive interference created upon reflection. The dotted lines in Figure 2-14C represent the maximum mirror displacement (λ/4) that can occur between data samples without repeating light intensity measurements due to the cyclic nature of interference. Figure 2-14B shows a transition between these two extremes with partial interference.

The same principles could be applied to a negative cavity deformation to produce the same trend.

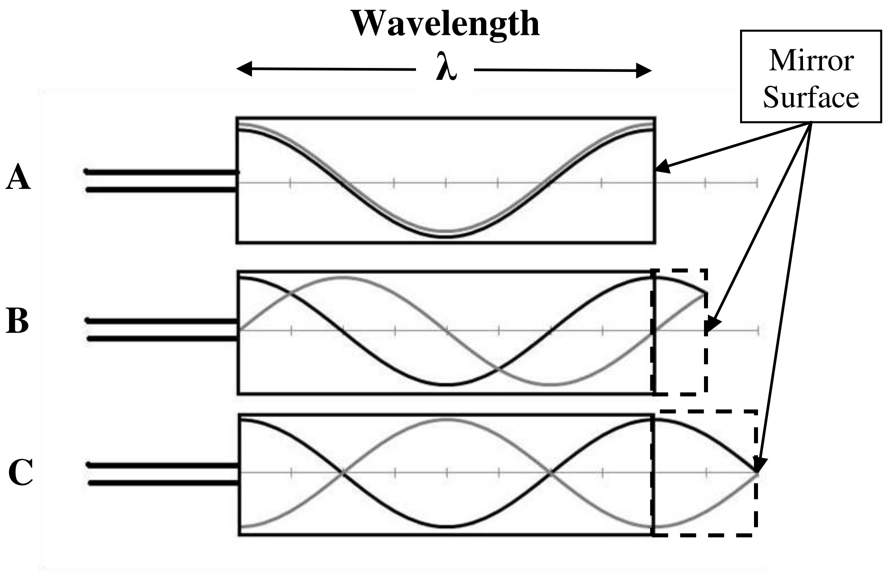

Figure 2-14: Fabry-Pérot cavity illustration A) Un-deformed state with constructive interference. B) Deformed state with a shift of λ/8 and partial interference. C) Maximum deformation to λ/4 with destructive interference. Further deformation per sampling period will repeat the cycle producing false data.

As previously stated, the nature of the Fabry-Pérot cavity is more complicated than what is shown in Figure 2-14 because a frequency range is used instead of a single wavelength. The light may also reflect multiple times inside of the cavity and the reflections may not be perfect. Compensation for these non-ideal characteristics is considered in the conditioning for commercially available sensors; further information can be obtained from the CVI Melles Griot (2011) or Physics Animations web pages.

2.2.2.2 Fiso sensor specifications

One particular sensor that uses this technology is made by FISO Technologies Incorporated. The Fiso model FOP-M-PK pressure sensors (0-150 psi and 0-1000 psi) were used in experiments with the Veloce-50 signal conditioning system. The spectral range of light used by the Veloce 50 is between 600 to 1000 nm with a peak at 850 nm (Gosselin, 2010). The Fabry-Pérot mirror surface is mounted on a linearly elastic diaphragm so deformation can be correlated to pressure through a single calibration constant (psi/nm), which is measured using the light intensity. A schematic of the physical characteristics of the sensor is shown in Figure 2-15. The Fabry-Pérot cavity and fiber optic cable are coated in a PTFE material for protection which creates a slight diameter increase.

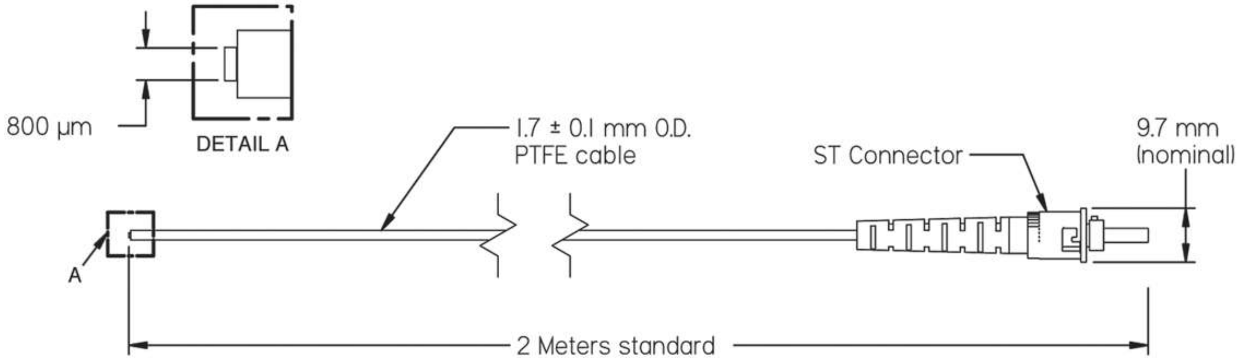

Figure 2-15: Model FOP-M-PK Fiso pressure sensor schematic (Fiso Technologies Inc.)

2.2.2.3 Sensor inconsistencies observed in a liquid at high loading rate

These sensors have been successfully used to measure intra-aortic blood pressure while sampling at a rate of 250 Hz (Pinet, Pham, & Rioux, 2005), but inconsistent measurements were observed when attempting to measure very high strain rates associated with shock waves, even with a 200 kHz sampling rate signal conditioner. One experiment performed at UNL attempted to measure pressure inside of a water filled cylinder using FOP-M-150 psi sensors, but the pressure measurements jumped unexpectedly and often settled at pressures other than ambient, as shown in Figure 2-16. The zero axis is gauge pressure (14.7 psi absolute), and measurements below 0 psi absolute were observed. The data from each shot exhibits a similar response without the skipping, but only Shot 89 does not appear to skip. Shot 86 appears to have shifted three times and Shot 87 shifted once. In this case the data could be potentially corrected since we know the actual response, but it is not practical/proper to repeat experiments until an accurate measurement is obtained. After observing poor results from several blast loading experiments, a separate set of experiments was developed to verify the exact cause of inconsistencies and develop a potential method to correct flawed data.

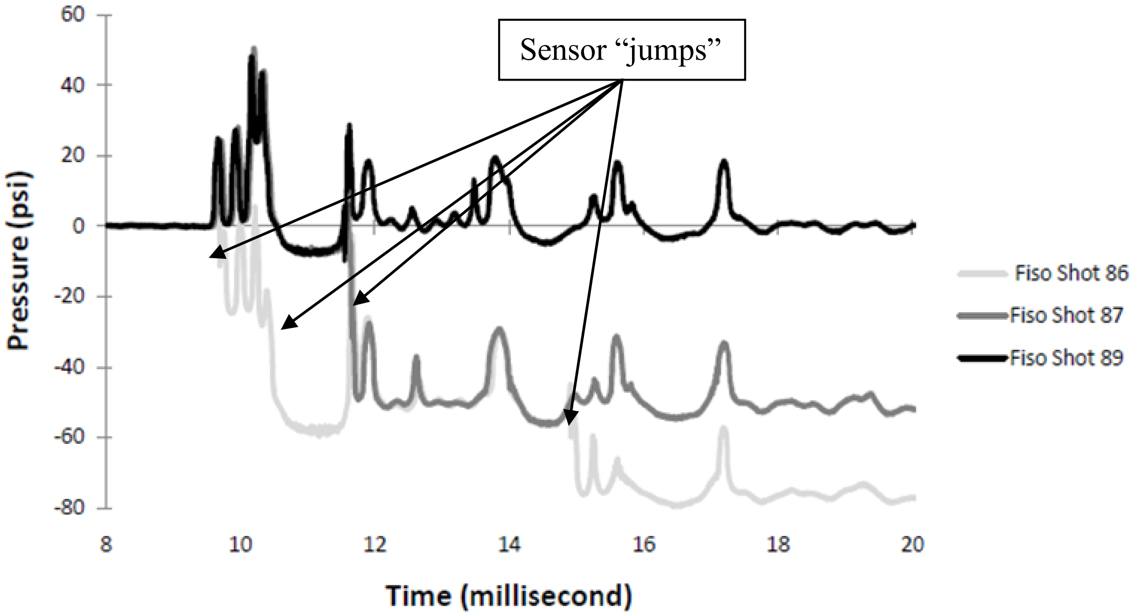

Figure 2-16: Inconsistent pressure measurements in water filled cylinder using Fiso sensors. Shot 86 and 87 show unexpected jumps. Shot 89 is assumed correct.

2.2.2.4 Experimental verification of high loading rate response

A loading rate faster than the signal conditioner sampling rate (200 kHz) is necessary to consistently replicate the sensor jumping phenomenon. Since the thickness of a weak shock front is on the order of the gas molecules' mean free path, an air shock provides a near instantaneous jump in pressure (Zel'dovich & Raizer, 2002). The actual loading rate is dependent upon the time it takes a shock wave to cross the sensor tip. A shock wave traveling at 500 meters per second will pass the sensor tip (~0.8 mm) in 1.6 microseconds. This corresponds to a loading rate of 625 kHz, which is 3 times faster than the sampling rate of the signal conditioner!

It was theorized that the use of a less sensitive sensor with a stiffer Fabry-Pérot cavity would require higher pressures before producing false measurements, so 1000 psi and 150 psi Fiso sensors were tested. The shock waves were generated in the 4 inch diameter shock tube at the University of Nebraska-Lincoln's blast wave facility. Dytran pressure measurements were used to measure the known shock profile for comparison.

Figure 2-17 shows several pressure profiles measured using Dytran and Fiso (0-150 psi) pressure sensors. The first pair of profiles were exposed to a 10 psi shock wave and match well (Figure 2-17A). Slight increases in shock wave overpressure caused the peak of the Fiso profile to abruptly shift to approximately -15 psi (Figure 2-17B). Further increases in shock wave overpressure caused the measured peak Fiso pressure to increase as shown in Figure 2-17C/D. Increases to higher shock intensities would cause the sensors to jump to a negative pressure reading again. The Fiso sensor baseline settles consistently around 26 psi which corresponds to a shift of half a wavelength (425 nm).

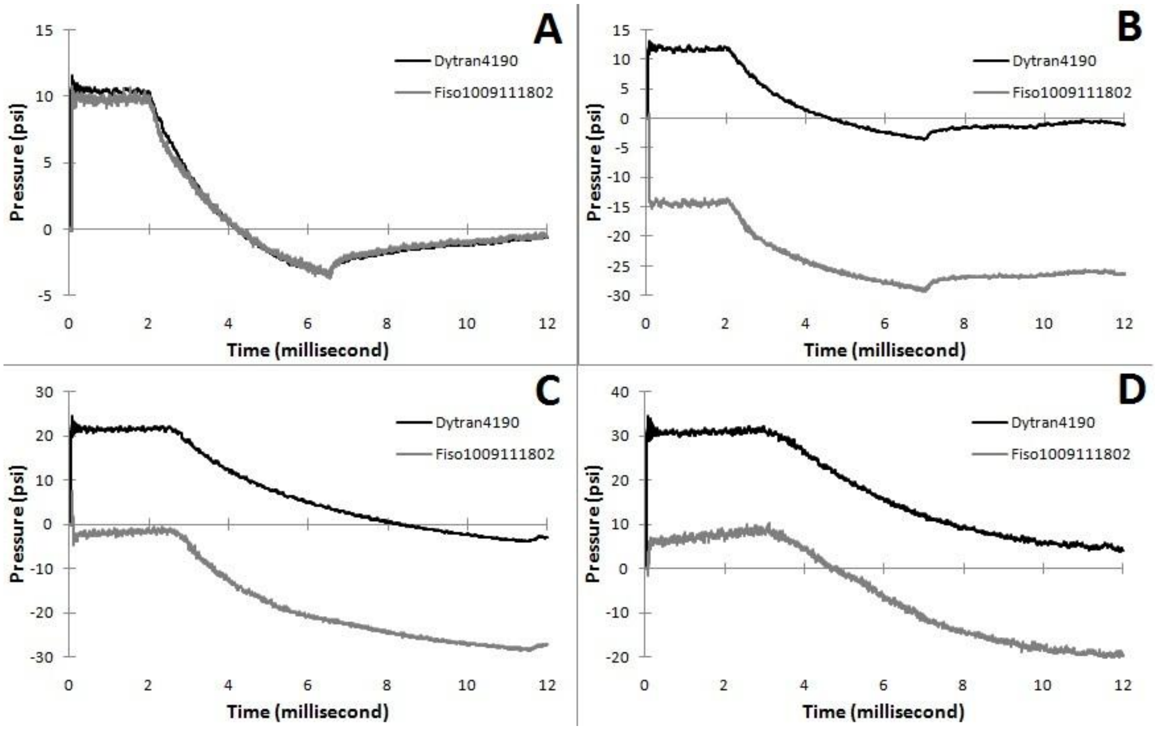

Figure 2-17: Comparison of 150 psi Fiso pressure profiles to Dytran pressure profiles from shots (A) 257, (B) 263, (C) 268, and (D) 274. The peak pressures of (A) and (B) are very similar, yet the Fiso sensor shows a distinct shift at the shock wave onset. Figures (C) and (D) demonstrate the effects of further increases in peak pressure.

An equation was derived to determine the actual change in cavity length/pressure by using the known wavelength λ and the temporary variable δ, as shown in Figure 2-18. In this figure an actual shift is shown in the positive direction, but since the shift is greater than λ/4 the signal conditioning system assumes a value at the closest location of equal intensity and phase. Although the actual shift is λ/4 + δ the observed shift is λ/4 – δ in the opposite direction.

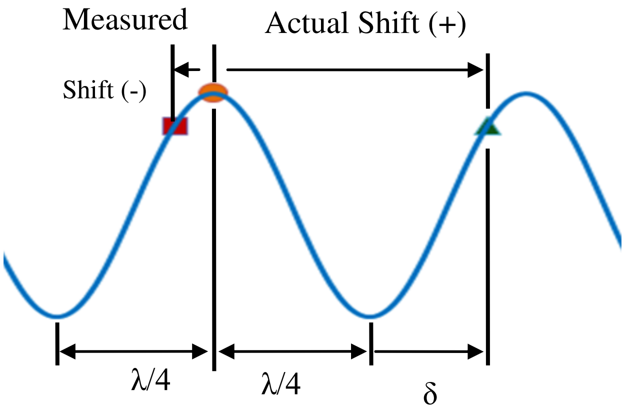

Figure 2-18: Light intensity graph showing measured shift and actual shift in light intensity

Using this thought process the following equations can be determined by inspection:

$$\text{Measured Shift } = \Delta\hat{L} = \left(\frac{\lambda}{4}\right) - \delta \tag{2.2a}$$

$$\text{Actual Shift} = \Delta L^{*} = \left(\frac{\lambda}{4}\right) + \delta \tag{2.2b}$$

Combining the previous two equations to eliminate the variable δ yields:

$$\Delta L^{*} = \left(\frac{\lambda}{2}\right) - \Delta\hat{L} \tag{2.3}$$

Likewise, for multiple jumps the actual displacement is:

$$\Delta L^{*}_{\text{Multiple Jumps}} = n\left(\frac{\lambda}{2}\right) - \Delta\hat{L} \tag{2.4}$$

$$n = Number\ of\ Jumps$$

The final result produced a method to determine the actual cavity deformation based upon the light wavelength, number of jumps, and the measured shift intensity. Correction was applied to adjust incorrect measurements using equation 2.4, the average light wavelength (850 nm), and shock profiles similar to the ones shown in Figure 2-17. The compiled data for two 150 psi sensors is summarized in Table 2-1.

Table 2-1: Measured and corrected displacements of Fabry-Pérot cavity for two Fiso sensors. The final baseline values are partially used to determine the number of shifts which occur in increments of λ/2.

	Dytran 4190	**Fiso Sensor 1010032204 (150 psi)**			**Fiso Sensor 1009111802 (150 psi)**		
Shot	**Peak Pressure (psi)**	**Measured Peak Displacement (nm)**	**Final Baseline (nm)**	**Corrected Displacement (nm)**	**Measured Peak Displacement (nm)**	**Final Baseline (nm)**	**Corrected Displacement (nm)**
261	**9.22**	**195.52**	**-0.67**	**195.52**	**129.42**	**-0.50**	**129.42**
258	**9.74**	**210.22**	**-0.44**	**210.22**	**140.34**	**-0.17**	**140.34**
259	**10.2**	**225.09**	**-0.19**	**225.09**	**148.62**	**-0.50**	**148.62**
260	**10.4**	**232.53**	**-0.43**	**232.53**	**151.76**	**-0.33**	**151.76**
257	**10.7**	**-188.61**	**-435.31**	**243.49**	**160.04**	**-0.99**	**160.04**
263	**12.3**	**-124.96**	**-435.13**	**307.14**	**-239.98**	**-425.34**	**185.61**
262	**14.3**	**-62.34**	**-434.96**	**369.76**	**-199.10**	**-425.34**	**226.49**
266	**14.5**	**-47.64**	**-434.96**	**384.46**	**-200.26**	**-425.34**	**225.33**
267	**14.7**	**-37.72**	**-434.78**	**394.38**			
264	**19.4**	**83.95**	**-433.54**	**516.05**	**-106.09**	**-426.99**	**319.50**
265	**19.5**	**94.75**	**-434.07**	**526.85**			
271	**20.7**	**138.49**	**-433.72**	**570.59**	**-81.26**	**-425.34**	**344.33**
270	**21.3**	**148.94**	**-433.54**	**581.04**	**-74.48**	**-425.34**	**351.11**
269	**22.2**	**181.53**	**-433.01**	**613.63**	**-45.18**	**-426.99**	**380.41**
268	**22.3**	**183.48**	**-433.01**	**615.58**	**-45.02**	**-428.65**	**380.57**
272	**27.8**	**16.59**	**-862.65**	**815.49**	**31.45**	**-423.68**	**457.03**
273	**27.9**	**35.07**	**-863.19**	**815.46**	**44.85**	**-422.03**	**470.44**
256	**30.8**	**150.89**	**-851.50**	**816.12**	**67.69**	**-435.27**	**493.28**
274	**31.8**	**144.87**	**-857.16**	**815.80**	**93.08**	**-422.03**	**518.67**
275	**39.3**	**-44.45**	**-1278.1**	**1224.1**	**208.86**	**-420.37**	**634.45**
276	**44.9**	**86.00**	**-1270.9**	**1224.5**	**314.62**	**8.28***	**740.21**

*This pressure trace initially shifted n=1 (Eq. 2.3), but shifted back to the approximate zero baseline during shock wave rarefaction.

The first column shows the shot number and the second column shows the peak pressure measured with a Dytran sensor. The measured "peak" displacement was determined using a 100 point (100 microseconds) average after the start of the flat topped shock profile. The shifted baseline values were used to determine the number of "shifts"; for every "shift" the baseline is lowered by half of a wavelength (850/2 = 425). Using the baseline information, the wavelength was calculated to be 862 nm with a standard deviation of 7.37 nm for sensor 1010032204 and 852 nm with a standard deviation of 7.38 nm for sensor 1009111802. These values are statistically close to the company-specified wavelength of 850 nm, confirming the accuracy of the measurements. The final column shows the corrected values from equation 2.4. All of these experiments exhibit zero or one false jumps, except Fiso 1009111802 during shot 276; a negative shift occurred upon shock arrival and a positive shift during the rarefaction causing the sensor to set itself back on the correct measurement path. For this reason the baseline shifted to approximately zero as well.

The measured and corrected shifts are shown graphically for sensor 1009111802 in Figure 2-19. Based on the factory calibration of 16.55 nm/psi the theoretical level at which a jump should occur is at approximately 12.8 psi (850/4/16.55 = 12.8 psi). Only single phase shifts occurred for this sensor, and a linear fit to the corrected data produced a slope of 16.317 nm/psi which is 1.4% different than the factory calibration of 16.55 nm/psi. This proves that the concept the theory is correct and that the data correction method works.

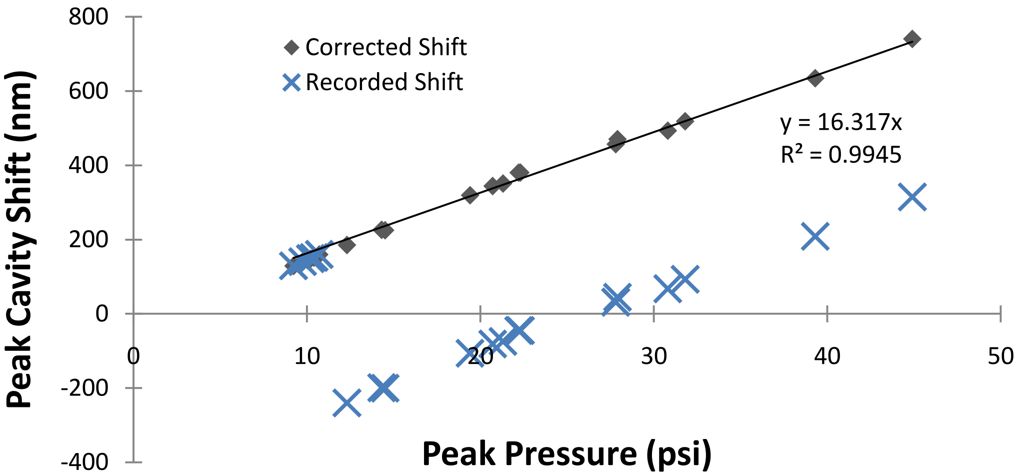

Figure 2-19: Fiso sensor 1009111802 comparison of measured cavity shift compared to the corrected cavity shift vs. the peak overpressure. The sensor's factory calibration is 16.55 nm/psi which is only 1.4% difference from the linear fit to the corrected data (16.32 nm/psi).

The other 150 psi sensor results are shown in Figure 2-20 which demonstrates up to three phase shifts. The corrected data produces a linear trend which has a slope of 29.813 nm/psi which is 41% different than the factory calibration of 17.71 nm/psi. Later inspection showed that the sensor was damaged causing sensitivity changes and increased scattering of results.

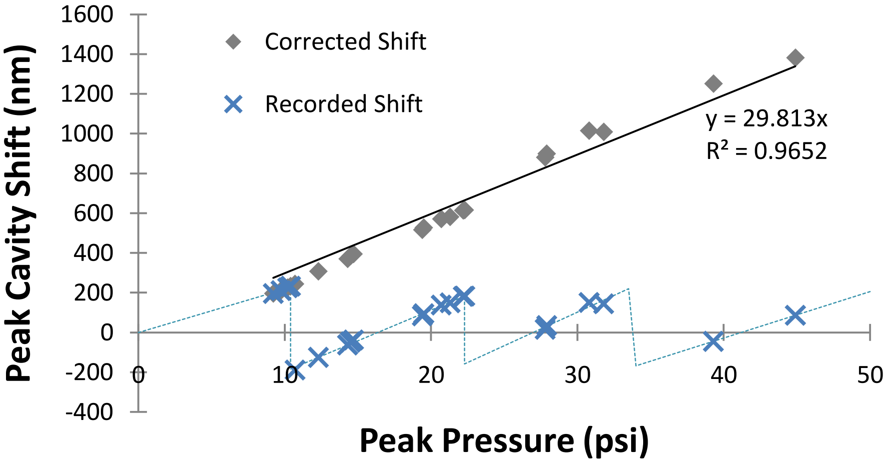

Figure 2-20: Fiso sensor 1010032204 comparison of measured cavity shift compared to the corrected cavity shift vs. the peak overpressure. This sensor was damaged and has a sensitivity of 29.8 nm/psi which is 41% higher than the factory calibration of 17.71 nm/psi.

Figure 2-21 shows hairline cracks in the Fiso sensor 1010032204 which caused increased sensitivity and less consistent results. The damage may have been caused by cavitation in water at the sensor tip during a previous experiment. The jagged cuts around the edges were caused by the sawing process during manufacturing.

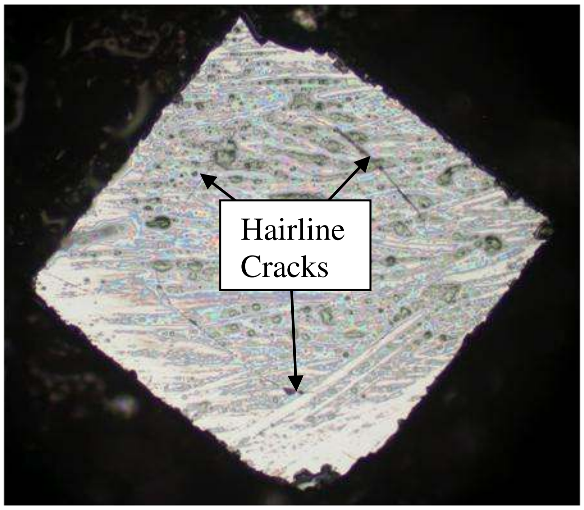

Figure 2-21: Hairline cracks on the tip of Fiso sensor 1010032204 causing increased sensitivity but not complete failure (Audet, 2011).

The 0-1000 psi sensors were tested under the same conditions but as predicted no phase shifts were measured. Based on the approximate factory calibration of 2.5 nm/psi, the 1000 psi sensors could withstand rapid loading to 85 psi without experiencing the unexpected jumps observed with the 150 psi sensors. The shock profiles matched the Dytran sensors so no data are shown. However, the lower sensitivity of these sensors caused a decrease in signal to noise ratio making signal filtering necessary.

2.2.2.5 Fiso sensor summary

The Fiso sensors have been shown to be capable of measuring shock waves accurately as long as the loading rate limit is not exceeded. High sensor loading rates cause shifts to occur which represent inaccurate pressure profiles. These false measurements can be corrected if the location, direction, and number of jumps are known. This can be a cumbersome process with some loss of data accuracy after every phase shift. The use of a sensor with a lower sensitivity requires higher pressures to cause a phase shift, but the signal to noise ratio is reduced requiring profile filtering.

Sensor dampening could theoretically be applied to the Fabry-Pérot cavity to reduce the sensor response time below the signal conditioner sampling frequency to potentially correct the problem. An increase in signal conditioner sampling frequency would also correct this problem. These issues should be carefully considered before performing high strain rate measurements using the Fabry-Pérot interferometer technique.

2.2.3 Kulite pressure sensors

The Kulite pressure sensors are small devices that implement the piezoresistive measurement technique similar to strain gauges. The sensing surface of these sensors contains a piezoresistive material mounted on a silicon diaphragm. Pressure changes to the diaphragm cause the resistance to change leading to a voltage change across a built-in Wheatstone bridge. A model 5186 strain gauge pre-amplifier from Signal Recovery Incorporated is typically used to amplify the signal by a factor of ten.

Probe and surface mount pressure sensors were both used for experiments. The probe style sensor (model XCL-072-500A) measures the absolute pressure from 0-500 psi with a nominal calibration of 0.200 mV/psi using 10 volts excitation. The diameter of this sensor is 0.075 inches allowing pressure measurements to be made using minimally invasive techniques. This sensor can also be submerged in conductive or non-conductive liquids and has an operational temperature range of 80° to 180° Fahrenheit. The surface mount style (model LE-080-250A) measures the absolute pressure from 0-250 psi with a nominal calibration of 0.400 mV/psi using 10 volts excitation. This sensor cannot be submerged in conductive liquids, but has a higher temperature range from 80° to 450° Celsius (Kulite Semiconductor Products, Inc., 2010). Further information about these sensors can be found at the Kulite web site. Figure 2-22 shows the probe and surface mount Kulite pressure sensors.

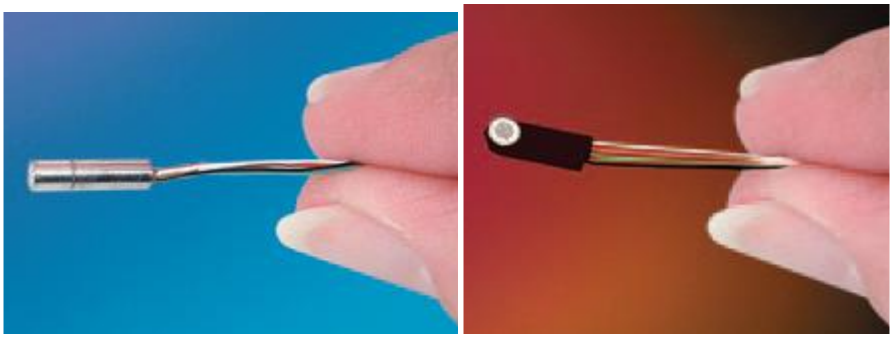

Figure 2-22: Kulite pressure sensors; probe model XCL-072-500A (left) and surface mount model LE-080-250A (right) (Kulite Semiconductor Products, Inc., 2010).

2.2.4 Strain gauges

The strain gauges used in several experiments were Vishay model CEA-13-250UN-350 gauges. These gauges have a resistance of 350 Ohms and a gauge factor of 2.130. The Wheatstone bridge was set up using the model MR1-350-130 bridge completion module from Vishay. This integrated circuit can be configured as a quarter or half bridge, but was set up in the quarter bridge configuration for all experiments. The voltage signal was amplified using the pre-amplifier model 5186 from Signal Recovery Incorporated.

Various strain gauge configurations and bridge types can be used for signal amplification, thermal compensation, etc. For high speed experiments such as shock wave tests thermally compensated circuits are not necessary since rapid loading is typically adiabatic (minimal heat transfer). Signal amplification was not necessary since large strains were observed in the experiments. Therefore a quarter bridge configuration shown in Figure 2-23 was used for all experiments outlined in this thesis.

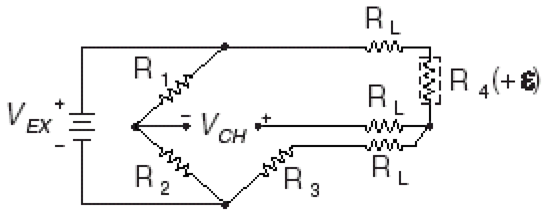

Figure 2-23: Quarter bridge strain gauge diagram. R1, R2, and R3 are resistors of the same resistance as the strain gauge (R4). RL is the lead wire resistance. (National Instruments, 2006).

The following equations are used for calculating strain based on the voltage measurements obtained using a quarter Wheatstone bridge shown in Figure 2-23. Vr is the reference voltage and is determined using the excitation, strained, and unstrained voltages. The strain can then be determined using the reference voltage (Vr), gauge factor (GF), gauge resistance (Rg), and lead resistance (RL) as shown by equation 2.5. The lead resistance is often negligible compared to the gauge resistance so the multiplier on equation 2.5 can be dropped if extreme accuracy is not required.

$$strain\ (\varepsilon) = \frac{-4V_r}{GF(1 + 2V_r)} \times \left(1 + \frac{R_L}{Rg}\right) \tag{2.5}$$

$$V_r = \left(\frac{V_{CH}(\text{strained}) - V_{CH}(\text{unstrained})}{V_{EX}}\right) \tag{2.6}$$

2.3 Summary

The majority of this chapter covered the measurement techniques used for recording blast wave experimental data. This includes information about data collection and processing as well as advantages/disadvantages of various sensors given by the manufacturers.

Most of the data collection hardware consisted of components purchased from National Instruments, with the exception of the trigger sensors. The system was set up to operate via a remote connection to a computer in a room outside of the shock facility. Programs were written in LabVIEW for collecting and processing experimental data, leading to consistent and rapid data analysis. The primary advantage of writing a custom analysis program is that it can be optimized to the user's needs.

Sensor specifications and theory of operation were covered, as well as some of the observed advantages/disadvantages. It was found that the piezoelectric pressure sensors are sensitive to accelerations, necessitating rigid sensor mounting. An in-depth study of the Fiso sensors was performed and demonstrated limitations under high loading rate conditions such as shock waves. A failure mode of the Fiso sensors was identified that can cause significant calibration errors without completely destroying the sensor. The following chapters are devoted to studies which implement these measurement methods.

Chapter 3: Dynamic Response of a Liquid-Filled Cylinder under Blast Loading

3.1 Introduction

Some components of TBI research that need to be understood are the fundamental damage mechanisms to the human head during blast exposure. Three potential blast-induced TBI mechanisms were outlined by Courtney & Courtney (2010): whole body exposure to blasts, head acceleration, and direct pressure transmission. Although these modes are likely intertwined, the topic of direct pressure transmission through the skull to the brain will be covered in this study.

The findings by Moss et al. (2009) demonstrate that significant skull flexure can occur for non-lethal blast waves which can induce potentially damaging loads in the brain. The skull flexure was observed under simulated loading without external impact inducing pressure variations in the brain.

A computational study performed by Taylor & Ford (2008) at Sandia National Laboratory used a model human head including the skull and brain to determine pressures in the brain during blast exposure. A main conclusion was reached that "significant levels of pressure, volumetric tension, and shear stress can occur in focal areas of the brain, dependent upon the orientation of the blast wave and the complex geometry of the skull, brain, and tissue interfaces" (Taylor & Ford, 2008). Figure 3-1 shows the incident shock profile as well as internal pressure measurements taken at the front, center, and back of the brain.

The internal pressure profiles are difficult to distinguish, but the waveform complexities are apparent. Pressure levels below the vapor pressure (4.6 kPa absolute at 30° Celsius (Cengel & Boles, 2006)) were recorded. Cavitation would likely occur under the tensile loading shown in Figure 3-1, especially since the brain is a water-based material with heterogeneous properties. Cavitation is one proposed injury mechanism for TBI which could induce localized brain damage (Wardlaw & Goeller, 2010). The presence of focal loading in the head model (Taylor & Ford, 2008) also supports the theory of cavitation occurring for the shown loading conditions. However, these loading conditions may not represent typical IED blast exposure seen in current military conflicts.

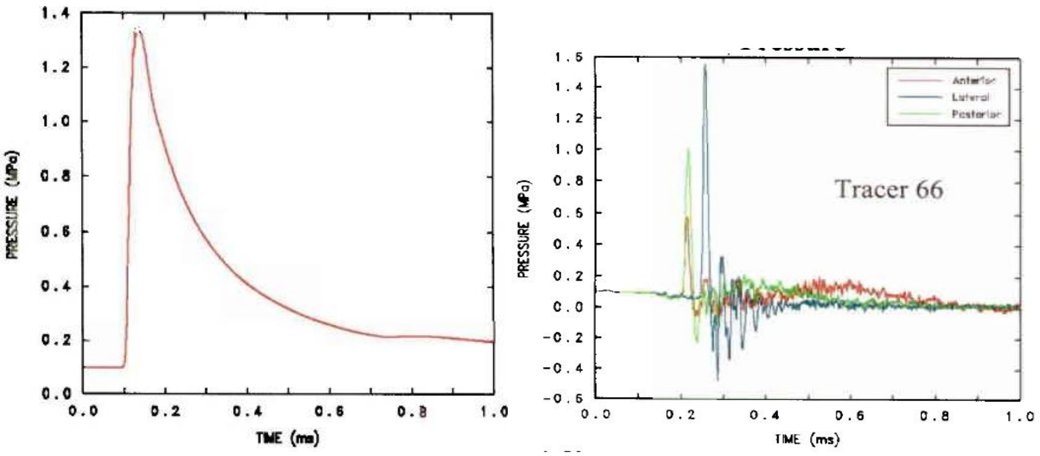

Figure3-1: (Left) Incident shock over pressure applied to a human head finite element model. (Right) Pressure profiles measured in the brain for blast loading at anterior, lateral, and posterior orientations (Taylor & Ford, 2008).

The incident profile by Taylor et al. (2008) is very intense (1.3 MPa) with a short duration (~0.6 ms) and is characteristic of exposure to an 8 pound TNT blast at a distance of four feet (Esparza, 1986). Rafaels et al. (2010) suggested that different injury mechanisms exist for short and long duration blasts, so the incident pulse should be carefully considered for TBI studies. Since typical IEDs are much larger than 8 pounds

(Dreazen, 2010) and high pressure, long duration shock waves are lethal (Bowen, et al., 1968), a lower pressure, longer duration shock wave may be more appropriate for TBI studies based on current events (Rafaels, et al., 2010).

The material and geometrical complexities of a realistic head-form make analysis of basic wave propagation modes difficult, so a cylindrical polycarbonate shell filled with mineral oil was developed as a simplified skull/brain model. Shepherd and Inaba (2010) performed similar research by impact loading a horizontally oriented, water filled polycarbonate tube as shown in Figure 3-2. They demonstrated a strong coupling between pressure waves in the fluid and structural waves in the solid. Another observation from the work by Shepherd & Inaba (2010) is the presence of cavitation shortly after the impact location. Their work was done to study the phenomenon called water hammer but could potentially be related to TBI studies. The oil filled cylinder was vertically oriented for blast loading, but the results by Shepherd & Inaba (2010) may be correlated to blast loading events.

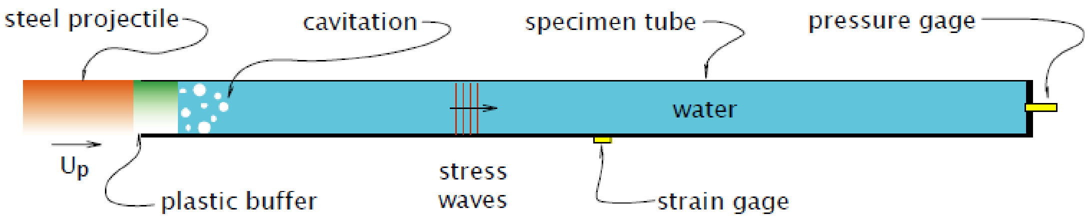

Figure 3-2: Structural testing of wave propagation in water filled tube by Shepherd & Inaba (2010)

One of the goals of this study is to understand the primary pressurization modes in the cylindrical sample. Wave propagation timing data was collected to determine correlations between surface pressure, surface strain, and internal pressure. The flexural rigidity and its correlation to internal pressure will be studied. The presence of negative pressure phases will also be monitored to determine the potential for cavitation to occur. Diffuse axonal injury is caused by high pressure loading (Taylor & Ford, 2008) which may not occur under typical blast loading except from the high pressures associated with the collapse of a cavitation bubble (Wardlaw & Goeller, 2010).

The potential injury mechanisms previously mentioned will be considered during the analysis of the loading experienced by the cylinder/oil model. Wave propagation timing, flexural loading, and cavitation are the primary topics covered by this study.

3.2 Experimental configuration

The simplified head model was developed using a polycarbonate cylinder filled with mineral oil. The cylinder length was 7 inches long with a 0.5 inch thick plug glued on each end which produced a liquid column length of 6 inches. The outer diameter is 2 inches. Experiments were done using cylinder wall thicknesses of 0.063 and 0.125 inches, which increases the structural stiffness by nearly a factor of 2. Previous cylinder experiments were mounted rigidly and experienced significant loading due to bending and circumferential strains. Bending strains associated with a rigidly mounted cylinder add complexity which was minimized by allowing the cylinder to linearly translate with minimal friction. This is also more representative of the free-field blast loading seen by an unconstrained individual. This translational model is also simplified since it incorporates linear translation, but not rotation.

Figure 3-3 shows the cylinder mounted on sliding tracks, which have rubber bumpers to absorb kinetic energy upon impact. The duration of the recorded data is less than the time to impact the bumpers, so the data is not affected by impact. The end-cap's rigidity prevents deformation, so the sensors were mounted centrally between the ends to minimize boundary effects and to maintain symmetry.

Figure 3-3: Polycarbonate cylinder mounted with sliding mechanism.

Figure 3-4 shows the sensor positions on/in the cylinder including surface pressure, circumferential strain, and internal oil pressure. Free field pressure measurements were also taken on the side of the shock tube. The sensor configuration consisted of surface mounted pressure sensors (Kulite model LE-080-250A) and circumferentially mounted Vishay strain gauges (model CEA-13-250UN-350) located at 0°, 90°, and 180° with respect to the incoming shock wave. The strain gauges were glued on using standard practices which can be described in full on the Vishay web site. The surface pressure sensors were glued and taped using rubber cement and duct tape with the sensing surface exposed.

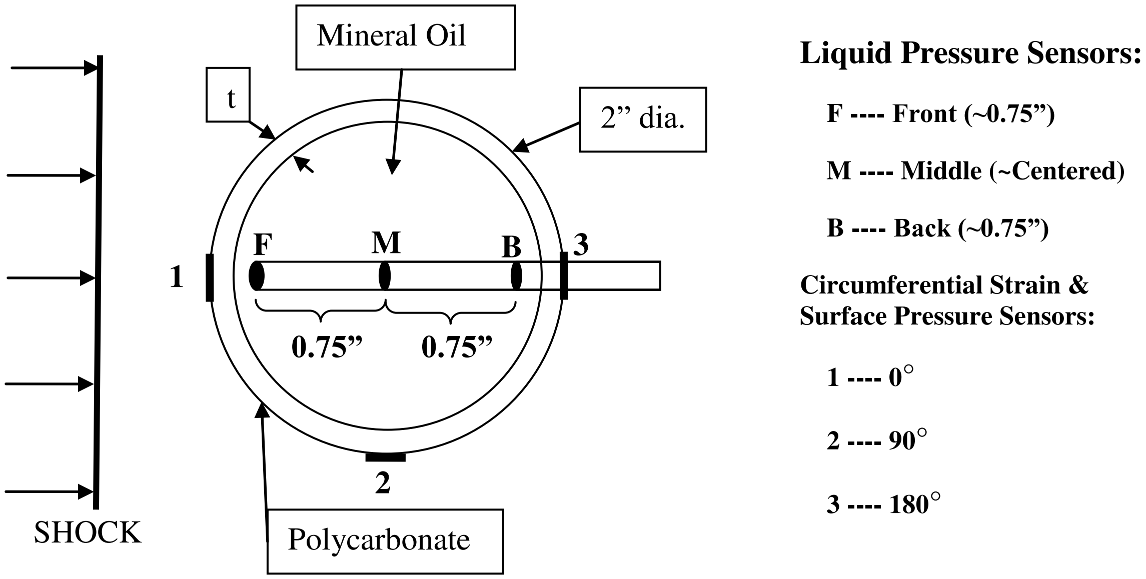

Figure 3-4: Illustration of mineral oil filled polycarbonate cylinder equipped with internal liquid pressure sensors, surface pressure sensors, and surface mounted circumferential strain gauges. Liquid sensors were placed using steel tubing with the sensor face normal to the shock front shown. 0.125" and 0.063" wall thicknesses were used.

Probe-style Kulite pressure sensors (model XCL-072-500A) were mounted at the center of the tube as well as at offsets of 0.75 inches in front of and behind the center sensor. These liquid sensors were mounted inside three thin-walled steel tubes through the back of the cylinder at an orientation perpendicular to the incoming shock front. The sensor tips were mounted flush with the front of the mounting tubes. The three sensor tubes were vertically aligned 0.30 inches apart with the front sensor above center and the back sensor below center.

One concern associated with this sensor setup is the rigid-mounted, head on orientation of the liquid pressure sensors. The head on orientation was considered negligible after testing by Matthew Nienaber showed insignificant variations for sensors mounted normal and parallel. One advantage of this placement method is that accurate positions can be determined.

3.3 Material properties

Polycarbonate and mineral oil were chosen for the two dimensional “head” model because their properties are similar to the skull and brain properties. The density, Young's modulus, bulk modulus, and sound speed are shown in Table 3-1 for these materials. Mineral oil was used as a brain substitute because of its uniform, well characterized properties and its similarity to actual brain matter. Water has a density and sound speed which is closer to brain matter, but mineral oil was chosen because cavitation in water caused sensor damage during previous experiments. A polycarbonate cylinder was used for the skull simulant because it has similarities with skull and is a common, well-characterized material. Common metals such as aluminum and steel were considered but they both have much higher stiffness properties so they were not used.

Table 3-1: Brain and skull material properties (Taylor & Ford, 2008) as well as mineral oil and polycarbonate material properties (Selfridge, 2009).

Material	**Density (ρ) kg/m^3**	**Young's Modulus (E) MPa**	**Bulk Modulus (K) MPa**	**Sound Speed (c) m/s**
Brain	**1040**	**0.123**	**2370**	**1509***
Skull	**1710**	**5370**	**4820**	**1679***
Mineral Oil	**825**	**---**	**1711***	**1440**
Polycarbonate	**1222**	**2400**	**6297***	**2270**

(*) Calculated value using C = sqrt (K/ρ)

The skull and brain properties were obtained from Taylor & Ford (2008) and the mineral oil and polycarbonate properties were obtained from Selfridge (2009). The sound speed was not published for the brain and skull, and the bulk modulus was not given for the mineral oil and polycarbonate. The sound speed is the square root of the quantity bulk modulus divided by density, so these unknown values were calculated.

3.4 Results

The timing of the surface pressure, circumferential strain, internal oil pressure, and the free field shock profiles are shown and discussed in the first section. The timing comparison is useful for understanding initial propagation modes and for making correlations between measurements.

The second portion of the results is devoted to understanding the connection between surface pressure and strain to the internal pressure. The internal pressure and surface strain profiles are compared for a thick (0.125”) and thin (0.063) walled cylinder, and the causes of variation is discussed.

3.4.1 Timing comparison of surface pressure, circumferential strain, internal oil pressure, and free field shock wave

A comparison of arrival times for pressures and strains at the locations shown in Figure 3-4 can lead to better understanding the basic wave propagation modes of transmitting pressure to the brain. The arrival times were determined for surface pressures, surface strains, and internal oil pressures using the first point that visually deviates from the signal baseline. The free field shock profile timing was assumed from free-field shock velocity measurements on the shock tube wall 10 inches upstream from the cylinder. All timing measurements correspond to planes parallel to the shock front passing through locations 1, 2, and 3 shown on Figure 3-4 except for the oil pressure measurements which were taken at locations F, M, and B. All measurements were normalized to the arrival at the front surface pressure sensor (location 1). Table 3-2 shows the timing summary using incident shock waves with approximate overpressure intensities of 24 psi for a 2 inch diameter oil filled cylinder with a 0.063 inch wall thickness. Measurements from seven shots are compiled with the averages and standard deviations shown at the bottom of the table.

One important point is that the surface pressure front travels faster than the free field shock from location 1 to 2. The higher reflected pressure on the cylinder surface caused a higher propagation velocity in this region. However, the free field shock velocity is higher than the surface pressure front from locations 2 to 3 because of a pressure drop due to expansion around the latter side of the cylinder. The free field shock continues to propagate at the same velocity, and overtakes the surface pressure front. This demonstrates a delay in surface pressurization compared to the free-field shock front.

Table 3-2: Normalized arrival timing for thin-walled (0.063") cylinder experiment using 24 psi incident shock waves.

	Free Field Shock			**Surface Pressure**			**Surface Strain**			**Oil Pressure**		
Shot #	**1**	**2**	**3**	**1**	**2**	**3**	**1**	**2**	**3**	**F**	**M**	**B**
659	0	52.1	104.2	0	45	137	xxx	xxx	xxx	6	21	34
660	0	52.5	105.0	0	48	139	xxx	xxx	xxx	5	19	33
661	0	52.3	104.7	0	47	139	xxx	xxx	xxx	7	22	34
662	0	52.9	105.8	0	47	140	xxx	xxx	xxx	5	20	33
663	0	52.1	104.2	0	46	136	4	21	37	6	20	33
664	0	52.2	104.5	0	46	138	4	21	37	6	20	33
665	0	52.8	105.7	0	47	140	4	21	38	6	20	33
Average	**0.0**	**52.4**	**104.9**	**0.0**	**46.6**	**138.4**	**4.0**	**21.0**	**37.3**	**5.9**	**20.3**	**33.3**
Std Dev	**0.00**	**0.33**	**0.66**	**0.00**	**0.98**	**1.51**	**0.00**	**0.00**	**0.58**	**0.69**	**0.95**	**0.49**

The similar arrival times at the side strain gauge (location 2) and the middle oil pressure sensor may show a correlation between the surface strain and oil pressure waves. The propagation speed of the surface strain was calculated to be 2400 +/-100 meters per second using one fourth the cylinder's outer circumference and the timing between two locations. This is approximately the measured longitudinal sound speed of 2270 m/s in polycarbonate. The variation of the measurements is due to the strain gauge size (1/4 inch), discrete time resolution (1 microsecond), material property differences, and recorded arrival time errors due to signal noise. It is also possible that the surface strain wave is induced by the internal oil pressure wave.

The velocity in the mineral oil was calculated using the direct distances between oil sensors and the arrival timing. Oil wave speeds were calculated to be 1450 +/- 110 m/s which is close to the longitudinal sound speed of 1440 m/s stated by Selfridge (2009). Since the surface strain wave and the internal oil wave timings are very close, the surface strain is likely caused by the internal fluid pressurization. However, this is not definite since the strain propagation speed is close to the longitudinal wave speed in polycarbonate. Experiments using a shell material with a higher longitudinal sound speed could verify this conclusion.

The arrival of the internal pressure wave at the front oil sensor was 6 microseconds after the arrival of the surface pressure. These results demonstrate that pressure waves in the oil are rapidly initiated by the surface pressure on the cylinder. However, the initial internal wave is primarily dominated by the front pressurization since the surface pressure wave is much slower than the internal pressure wave.

Table 3-3 summarizes the arrival timing for the lower pressure loading (12 psi) of the thin-walled cylinder. The only significant difference with the high pressure shots is the free field shock and the surface pressure timing. The incident shock is slower, so the surface pressure also propagates at lower velocities. The propagation speed of the internal oil pressure and surface strain are comparable to the higher pressure (24 psi) shot.

Table 3-3: Normalized arrival timing for thin-walled (0.063") cylinder experiment using 12 psi incident shock waves.

	Free Field Shock			**Surface Pressure**			**Surface Strain**			**Oil Pressure**		
Shot #	**F**	**M**	**B**	**F**	**M**	**B**	**F**	**M**	**B**	**F**	**M**	**B**
666	0	61.7	123.4	0	55	161	5	23	38	7	20	35
667	0	62.0	123.9	0	56	161	4	22	38	8	20	35
668	0	61.6	123.2	0	56	159	5	21	40	7	21	34
669	0	61.1	122.2	0	55	159	4	22	38	7	21	34
670	0	62.1	124.1	0	55	161	5	21	38	7	20	34
671	0	60.9	121.7	0	54	159	5	22	38	7	21	34
Average	**0.0**	**61.5**	**123.1**	**0.0**	**55.2**	**160.0**	**4.7**	**21.8**	**38.3**	**7.2**	**20.5**	**34.3**
Std Dev	**0.00**	**0.48**	**0.95**	**0.00**	**0.75**	**1.10**	**0.52**	**0.75**	**0.82**	**0.41**	**0.55**	**0.52**

The arrival timing chart for the thick-walled (0.125") cylinder loaded with a 24 psi shock front shows similar results as the thin-walled cylinder (0.063") under identical surface loading. The surface strain timing for the thick-walled cylinder was difficult to obtain because of a poor signal to noise ratio, leading to very rapid wave propagation measurement (~2700m/s), which is not likely correct. For this reason the timing of the low pressure loading of the thick-walled cylinder is not shown.

Table 3-4: Normalized arrival timing for thick-walled (0.125") cylinder experiment using 24 psi incident shock waves.

	Free Field Shock			Surface Pressure			Surface Strain			Oil Pressure		
Shot #	**F**	**M**	**B**	**F**	**M**	**B**	**F**	**M**	**B**	**F**	**M**	**B**
681	0	53.1	106.2	0	46	139	3	19	29	6	16	32
682	0	54.5	109.0	0	48	143	3	17	33	6	17	32
683	0	52.9	105.9	0	46	137	2	16	33	6	17	30
684	0	52.9	105.9	0	47	139	0	16	31	6	17	31
Average	**0.0**	**53.4**	**106.7**	**0.0**	**46.8**	**139.5**	**2.0**	**17.0**	**31.5**	**6.0**	**16.8**	**31.3**
Std Dev	**0.00**	**0.76**	**1.52**	**0.00**	**0.96**	**2.52**	**1.41**	**1.41**	**1.91**	**0.00**	**0.50**	**0.96**

3.4.2 Surface strain, surface pressure, and internal pressure profile comparison

Timing analysis suggested that the surface pressure loading causes significant and rapid changes to the oil pressure. The surface pressure measurements were equal for the thick and thin cylinder tests with equal incident overpressures. Figure 3-5 shows the surface pressure measurements at 0°, 90°, and 180° on the 2 inch diameter cylinder placed inside the 9 inch square shock tube using three 0.010 inch Mylar membranes.

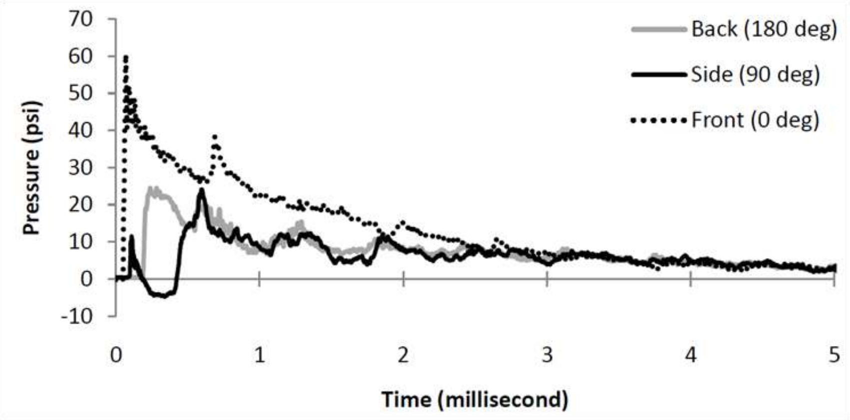

Figure 3-5: Surface pressure measurements on the cylinder surface at 0°, 90°, and 180°

The front pressure sensor (0° orientation) exhibits a decaying profile characteristic of the reflected pressure from a Friedlander profile. The 90° and 180° orientations do not experience reflected pressure loading so the peak pressure is significantly less than on the front surface. The wave timing showed the initial pressure wave in the oil was induced by the abrupt change in pressure on the front surface. Therefore, changes in oil pressure should be affected by the pressure gradients on the entire surface.

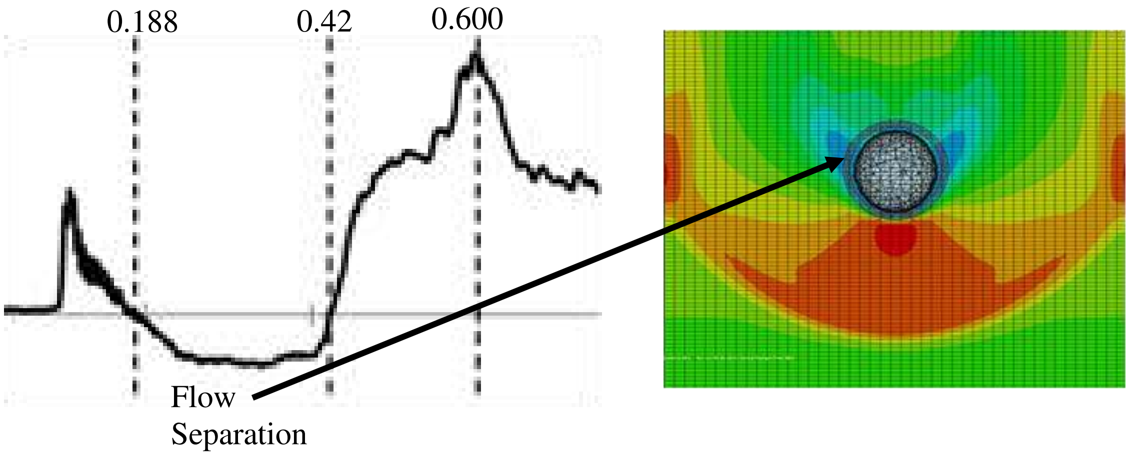

Figure 3-6: Surface pressure history at 90° (left). Pressure field obtained from simulation at 0.25 milliseconds (right) obtained from Veera Selvan (2011)

Figure 3-6 shows the experimental 90° pressure history as well as the pressure field on the cylinder surface at 0.25 milliseconds, obtained from simulation (Selvan, 2011). The 90° orientation profile has a small pressure spike followed by a significant negative pressure phase beginning at 0.188 milliseconds and ending at 0.422 milliseconds. This negative phase is caused by flow separation from the cylinder and ended upon equilibrating with the surroundings. The flow separation is apparent on the cylinder sides. It will be seen that this negative surface pressure phase corresponds to degradation in internal oil pressure.

Shortly after a pressure spike of approximately 10 psi appears in all pressure profiles at 0.600 milliseconds; this is caused by reflection from the shock tube wall. This small reflection represents a loading error created from obstructing the shock tube, which can be minimized by reducing sample size or increasing the shock tube size. It is important to understand the majority of secondary re-pressurization in the 90° profile is caused by recompression of the separated flow, and not from the reflection inside the shock tube.

Strain profiles for the thick and thin-walled cylinders are shown in Figure 3-7. The circumferentially mounted gauges initially experience a low-intensity surface wave which travels at approximately 2400 m/s, which is relatively close to the published longitudinal wave speed. However, the initial strain wave may not be a longitudinal wave, but may be caused by the internal pressure wave.

A higher intensity, low frequency structural oscillation occurs in the cylindrical shell after the low intensity, high speed surface wave passes. The loading on this cylinder is dynamic with abrupt changes in surface pressure as shown by Figure 3-5 which causes the cylinder to deform in an elliptic manner. Initially the front and back strain gauges experience compression while the side gauge undergoes tension. The shell then oscillates in an elliptic manner due to the stored strain energy in the shell. Peak oscillation frequencies were determined using Fourier transforms and were found to be 300 and 700 Hz for the thin and thick-walled cylinders respectively at all three strain gauge locations. The oscillation frequency is dependent upon the structural rigidity of the cylinder; a more rigid cylinder oscillates at a higher frequency. Timing was not determined for the low frequency oscillation because of the ambiguity of the arrival times/peak intensities.

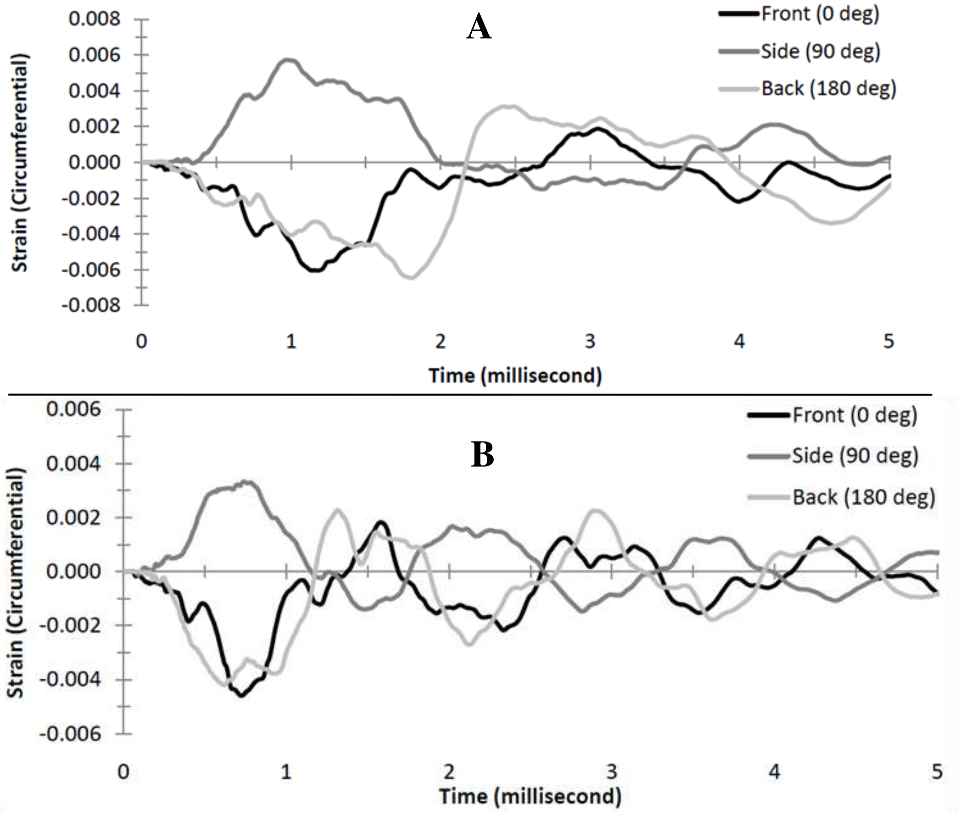

Figure 3-7: Strain measurements for the thin-walled (A) and thick-walled (B) cylinders.

Since the strain signals primarily exhibit low frequency response and the liquid response can travel at the longitudinal wave speed (~30 microsecond cylinder traversal time), the net effect of strain loading was compiled into a lumped sum. Since the side gauge typically oscillates with an opposite sign as the front and back gauges, the elliptic change was defined and calculated to be *approximately proportional* as described in equation 3.1. Double weighting was applied to the side strain measurement to balance the weighting of the front and back strains.

$$\text{Elliptic Changes} \approx\propto (\text{Front} + \text{Back} - 2 * \text{Side})/4 \qquad (3.1)$$

If the strain values are directly added (using a double weighted side strain) the elastic volume change is determined by equation 3.2. Since the mineral oil is approximately incompressible, the volume change should be zero if the cylinder deforms into a symmetric ellipse. Some variation will exist because point-wise measurements were taken at only three locations, the cylinder does not deform symmetrically, and the loading is dynamic.

$$\text{Elastic Volume Change} \approx \propto (\text{Front} + \text{Back} + 2 * \text{Side})/4 \qquad (3.2)$$

Figure 3-8 shows the approximate elliptic and elastic volume changes for the thick and thin-walled cylinders. The average elliptic strain profiles oscillate in a damped sinusoidal manner. The oscillation frequency of the thick-walled cylinder is around 675 Hz and the oscillation frequency of the thin-walled cylinder is around 285 Hz. As expected the approximate elastic volume change is nearly zero with some fluctuation due to the dynamic conditions.

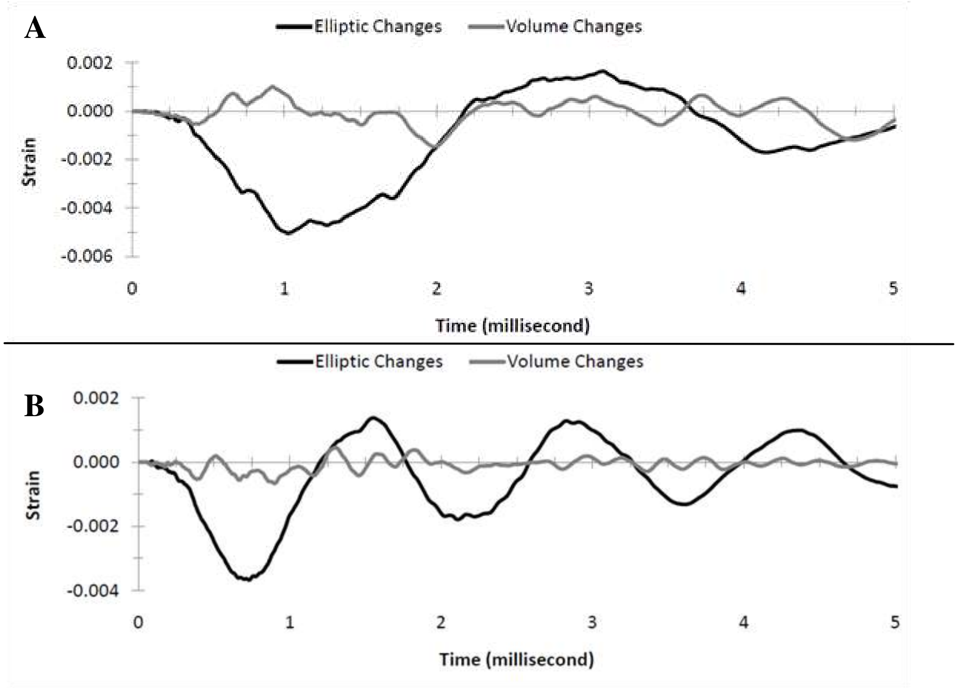

Figure 3-8: Averaged strain measurements for the thin (A) and thick (B) walled cylinders. A rough calculation of the elliptic changes and the elastic volume changes were calculated.

The vertical timing markers shown in Figure 3-6 are used for comparison to the internal oil pressure profiles shown in Figure 3-9 for the thick- and thin-walled cylinders at the three fluid locations. The front oil pressures shown in Figure 3-9A exhibit rapid pressure jumps followed by pressure decay. The sharp rise in pressure can be attributed to the pressure wave transmitted from the front surface pressurization. The pressure release from 0 to approximately 0.422 milliseconds is strongly influenced by the rapidly decaying pressure on the side surface of the cylinder shown in Figure 3-5. The initial decay is attributed to surface pressure decay. The sharper, secondary decay is strongly influenced by the negative pressure release on the side surface of the cylinder.

The back oil pressure trace shown in Figure 3-9C experiences an initial pressure spike with a generally gradual pressure rise. The initial oil pressure spike is induced by the reflected pressure on the front surface of the cylinder. The center oil pressure shown in Figure 3-9B demonstrates significant oscillation with intensities between the degrading front pressure and the increasing back pressure.

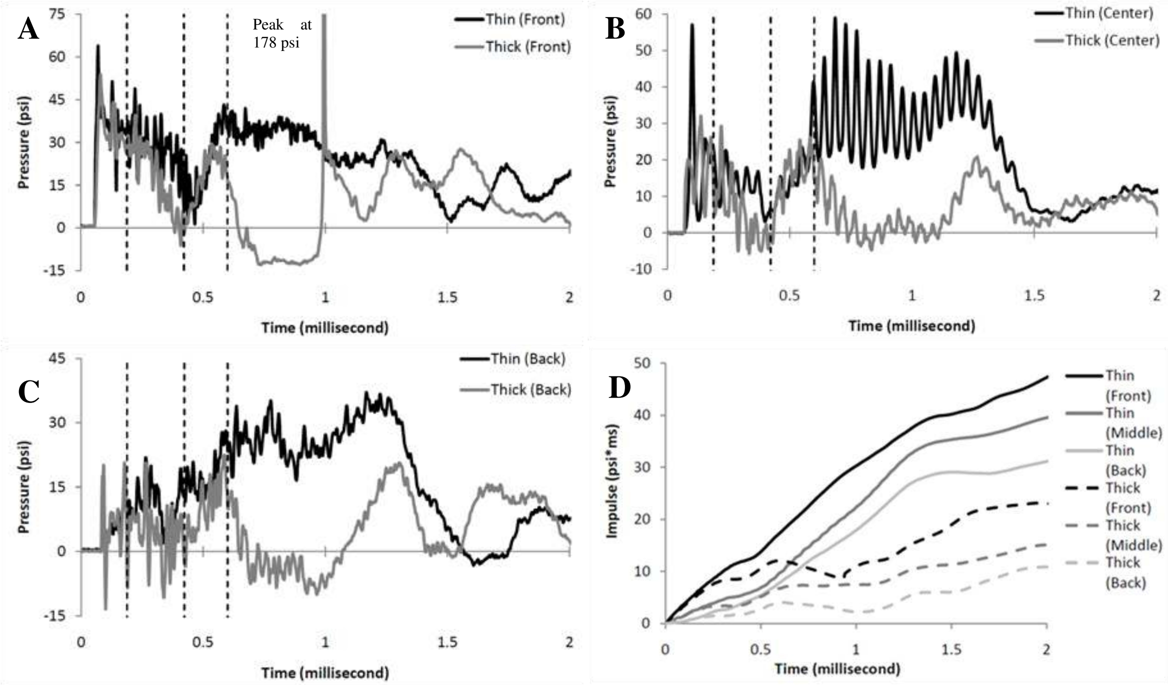

Figure 3-9: Comparison of internal oil pressure profiles at (A) Front, (B) Middle, and (B) Back of the cylinder for 0.125" and 0.063" wall thicknesses. Figure (D) shows the integration of the pressure profiles for the thick and thin cylinder.

The initial peak pressures were difficult to determine due to ambiguity and pressure oscillation, so integration of the pressure profiles was done to show the trend of higher averaged peak pressures near the front of the oil (brain), as shown in Figure 3-9D. Taylor et al. (2008) found the highest pressure levels on the side of the brain closest to the blast source.

The oil pressure variations are due to the pressure gradients on the surface (see Figure 3-5) causing pressure waves in the liquid to attempt to equilibrate. The front oil pressure primarily experiences effects from the high surface pressure at the front of the cylinder, but experiences degradation from the low vacuum pressure on the side surface. Since the back half of the cylinder primarily experiences low pressures, the back oil pressure sensor experiences stronger effects from the low surface pressures. The high frequency oscillations seen in the signals are due to competing effects from surface loading conditions. These competing effects can be seen in the oscillation of the center oil pressure shown in Figure 3-9B; the peaks follow the decreasing trend of the front pressure profile (Figure 3-9A) and the valleys follow the increasing trend of the back pressure profile (Figure 3-9C). It must be kept in mind that the internal pressures are affected by all surface pressure gradients, making definite analysis difficult.

Recompression in the oil is distinctly shown for both cylinder thicknesses and at all locations from approximately 0.422 to 0.600 milliseconds as shown in Figure 3-9A-C. This is influenced by the increased pressure on the side of the cylinder, as shown by the 90° surface pressure in Figure 3-5. The convergence of the surface pressure gradients causes the internal oil pressures to follow similar trends. If only the surface pressure contributes to the internal oil pressurization, the oil pressure at all locations should converge around the surface pressures. However, the internal pressure profiles for the thick-walled cylinder deviate from the thin-walled cylinder after approximately 0.600 milliseconds.

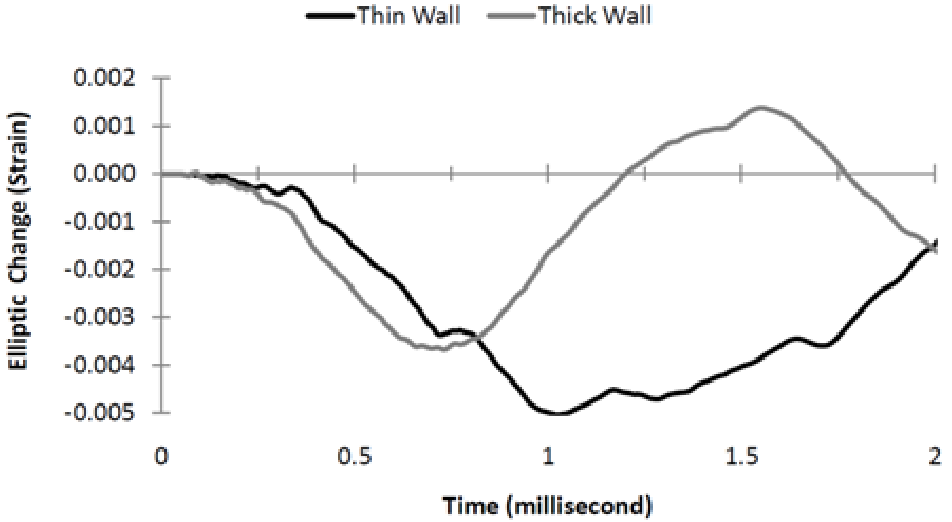

Figure 3-10: Average elliptic strain profile comparison for the thin and thick-walled cylinders

The deviation of internal oil pressure is likely caused by surface strain differences demonstrated by the comparison of average elliptic strains shown in Figure 3-10. Since the surface pressure loading and body accelerations are equivalent, the only explanation is that the oil pressure deviations must be caused by structural oscillation differences. The strain values do not significantly deviate until approximately 0.8 milliseconds, but the strain rate may also have a contributing effect because the slope of the strain profile begins deviating at approximately 0.6 milliseconds. The higher frequency oscillation of the thick-walled cylinder may cause more prominent oscillation in the oil because of the differences in structural response of the oil at higher loading rates. This would also explain some of the minor internal loading differences between the thick- and thin-walled cylinders before the drastic deviation.

The internal pressures are not entirely dominated by the low frequency structural oscillation. The surface pressure, surface strain, strain rate, and acceleration may all be contributing factors to the internal pressure, making long-term analysis difficult. Three dimensional effects may cause some unknown loading. However, it is apparent that the differences in structural rigidity produce significantly different loading characteristics.

The impulse graph shown in figure 3-9D initially shows similar results for the thick and thin cylinders, but deviates significantly after approximately 0.6 milliseconds. This shows that the cylinder thickness does not initially affect the internal pressures, but has an important role for the later affects. The initial internal pressurization was dominated by the surface pressure gradients, but after approximately 0.6 milliseconds structural effects dominate. Once again, it must be recalled that although different effects dominate, other effects may also cause significant loading. Separation of the various effects could lead to better understanding of different propagation modes within an enclosed, fluid-filled shell.

A cavitation bubble was formed and collapsed on the front sensor in the thick-walled cylinder as shown by the negative pressure phase and large pressure spike shown in Figure 3-9A. The pressure spike has a peak value near 180 psi and a short duration of approximately 10 microseconds. This peak pressure is not necessarily accurate due to measurement errors caused by overshoot and/or sensor dynamics, but the pressure is likely quite high for a short duration. The occurrence of cavitation at this location was consistently observed for 3 tests at the front location of the thick-walled cylinder, but was not observed in the thin-walled cylinder. Although the thin-walled cylinder experiences a higher average pressure (impulse), the thick-walled cylinder experiences a greater occurrence of negative pressure which could lead to cavitation.

Cavitation in a previous cylinder experiment was observed on the tip of a Fiso sensor submerged in water as shown in Figure 3-11A. This cavitation pressure profile shown in Figure 3-11B is similar to the cavitation pressure profile on the Kulite sensor shown in Figure 3-9A. Although the sensor was likely an initiation point for the formation of cavitation bubbles, the low liquid pressure is an initiation factor. Also, the brain has heterogeneities that could serve as cavitation initiation points. Cavitation has also been induced from slight impurities such as carbon fiber and wheat flour in water filled cylinder experiments.

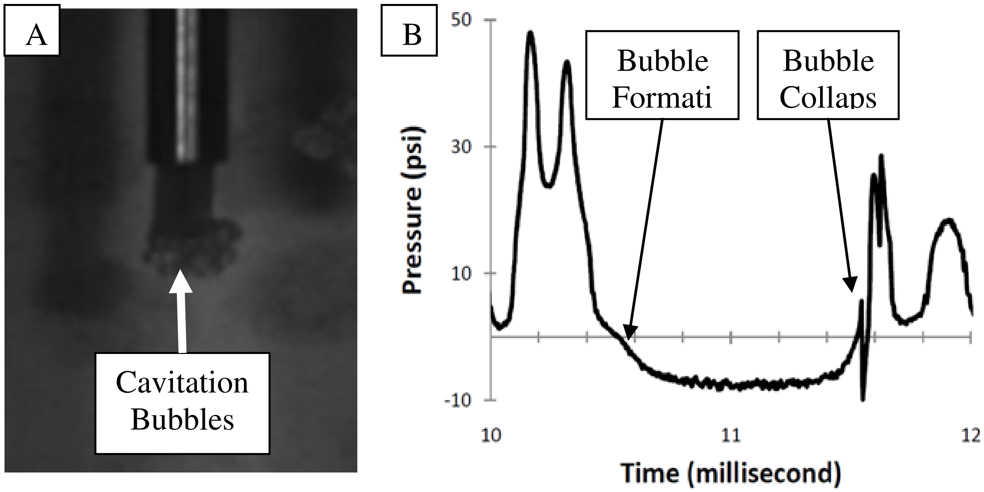

Figure 3-11: (A) Cavitation bubbles forming at the tip of a Fiso sensor. (B) Recorded pressure profile during formation and collapse.

Damage to the Fiso sensor occurred from the experiment shown in Figure 3-11, which leads to the conclusion that high pressures associated with cavitation could induce localized diffuse axonal injury in the brain. This is based on the idea that cavitation occurs in the brain under blast loading. Cavitation was observed at the front of a horizontally mounted water-filled tube under impact loading (Shepherd & Inaba, 2010). This further supports the theory that cavitation can be induced in a fluid filled structure.

Further research is needed to show the existence of cavitation in the human brain. Realistic models/cadavers could potentially be used to study this effect.

3.5 Discussion

A simplified head model was developed using an elastic shell (polycarbonate cylinder) filled with a viscous fluid (mineral oil). The cylinder had a two inch diameter with wall thicknesses of 0.125 and 0.063 inches. This model measured surface pressure and circumferential strain on the front, side, and back surfaces. Internal oil pressure measurements were taken at the front, center, and back of the cylinder. The primary objective of the study was to understand the links between surface pressures and strains to internal fluid loading.

Analysis was performed to understand the timing of the free-field pressure, surface pressure, surface strain, and internal oil pressure waves which had cylinder traversal times of 105, 138, 37, and 33 microseconds, respectively. The surface pressure wave was faster than the free-field shock until reaching the side of the cylinder, but decreased as it expanded around the back of the cylinder causing the surface pressure wave to lag the free-field wave. The internal oil pressure and the surface strain waves initially propagated independently near their respective longitudinal wave speeds, which is much faster than the surface and free-field pressure waves. Due to timing similarities, it is uncertain whether the initial stress wave in the polycarbonate is a longitudinal stress wave or if it is induced by the internal oil pressure wave. It is believed that the internal pressure wave induces the initial surface stress wave. The timing also showed that these waves were initiated by the abrupt shock loading at the front of the cylinder, which demonstrates that the internal oil pressures are affected by the dynamic surface pressure conditions.

The surface pressures on the cylinder were measured at the front (0°), side (90°), and back (180°). The front location experienced a peak intensity correlating to the reflected shock pressure followed by gradual decay associated with a Friedlander profile. The back pressure profile had similar characteristics, except the peak pressure was lower. The side pressure profile had a short duration pressure spike followed by a negative pressure phase caused by flow separation. The negative pressure phase ended around 0.42 milliseconds, causing an abrupt jump in surface pressure to a similar intensity as the back location. These surface pressure gradients significantly affected the internal oil pressures.

The front oil pressure rapidly peaked followed by pressure degradation during the first 0.42 milliseconds. On the contrary, the back oil pressure generally experienced a gradual pressure increase, with sharp pressure oscillations intertwined. The center oil pressure experienced the most significant oscillations with peak intensities similar to the degrading front oil pressure and valley intensities similar to the increasing back oil pressure. The internal pressure differences/oscillations are likely attributed to the competing effect caused by the strong surface pressure gradients.

From 0.42 to 0.6 milliseconds, the internal oil pressure experienced a rise in pressure. This is attributed to the jump in surface pressure seen on the side of the cylinder. After 0.42 milliseconds, the lack of any low pressure surfaces minimizes the occurrence of negative pressurization of the liquid. However, structural oscillations appear to cause significant loading effects after 0.6 milliseconds.

The internal pressure in the thick and thin cylinder exhibited abrupt deviations after 0.60 milliseconds, which was strongly influenced by structural oscillations indicated by circumferential strain. Since the structural oscillations are primarily low frequency, an averaged elliptical strain was calculated. The strain rate is likely an important factor because the internal pressure deviation occurred around 0.6 milliseconds. At this time, the strain slopes (strain rate) significantly deviated.

Although the sudden changes after 0.6 milliseconds are attributed to the circumferential strain and strain rate, the surface pressure and body acceleration also continue to contribute to the internal pressure. This is apparent because the internal pressure oscillates around the decaying trend of the surface pressure. Because of loading complications, in-depth analysis was not carried out for the long duration pressurization. The injury mechanisms for the initial loading of the brain appear to be dominated by the surface pressure gradients, but the later oil pressure oscillation is caused by structural oscillation after the surface pressures semi-equilibrated.

The peak internal pressures were not determined directly, but integration was used to demonstrate peak pressures at each location. The slope of the impulse demonstrates the higher peak pressures in a clean manner. The front sensor exhibited the highest peak pressure, followed by the middle, and then the back sensor. The front sensor had a shock-like rise in pressure, but the back sensor had a more gradual pressure change.

Overall the average positive pressure was significantly higher for the thin-walled sample, but tension phases were more prominent in the thick-walled sample. This is very interesting because internal pressurization and cavitation are two of the proposed modes for TBIs. Based on these findings the stiffer cylinder is more likely to experience cavitation but the more flexible cylinder is more likely to see higher pressure loading induced by structural oscillation. Further testing needs to be conducted to better understand and confirm these findings.

Testing small-scale, simplified models is an important step towards understanding traumatic brain injury, but experimental testing of wave propagation modes in full-scale, realistic head models is a step that must be taken to fully understand the puzzle. Historically, testing of large-scale experiments has been performed outside of shock tubes, but this location may not be best suited for replicating explosive driven shock waves. It was hypothesized that the flow discontinuity from 1- to 3-dimensional expansions could cause significant disturbances and flow characteristics that are not representative of a Friedlander profile. The results of this liquid-filled cylinder study show a strong correlation between surface pressure gradients and internal “brain cavity” pressurization. Therefore an experiment was designed to test the loading inside and outside of a shock tube to determine if significant variations in surface loading exist.

Chapter 4: Wave Profile Evolution outside a Shock Tube

The effects of shock wave loading upon exiting a shock tube are studied using a cylinder positioned at various locations outside and inside a shock tube. The goal of this study is to determine ideal sample placement for blast induced traumatic brain injury experiments. It was found that peak pressures as well as the shape of the pressure profiles changed significantly at various distances from the shock tube exit. The shock waves are planar at the shock tube exit, but become increasingly non-planar to a peak level, and finally progress to an increasingly planar state. Pressure gradients on the cylinder surface also confirmed the non-uniformity of the shock wave and the 3-dimensional expansion outside of the shock tube. The conclusion was reached that blast waves are best replicated inside the shock tube as opposed to outside.

4.1 Background

Shock tubes are regularly used for generating shock waves to simulate the effects of an explosive. In the past there has been significant variance in the placement of samples for blast experiments. A study using swine in a 71 inch diameter shock tube by Bauman et al. (2009) placed samples inside of the shock tube shortly after the driver section. A study involving rats and blast exposure by Richmond et al. (1966) placed the samples at the end of a closed shock tube, causing the rats to be loaded with a reflected shock pulse. Another experiment on rats by Long et al. (2009) also placed the rats at the exit of an open ended shock tube.

This variation in sample placement leads to the question of where a sample should be placed for blast related shock experiments. The scattered test placement has produced a lack of uniformity among researchers performing TBI oriented blast wave research. It is known that pressure histories change at various locations in a shock tube, but careful consideration of sample placement must be taken to ensure the loading accurately represents blast loading.

In a typical free field explosion, a shock wave propagates radially from the source of the explosive and has a three dimensional flow field. Although the shock front has significant curvature close to the explosive source, at greater distances the shock front can be assumed to be planar. Shock tube generated blast waves, however, have a planar form. Due to the increased size of improvised explosive devices in Afghanistan (Holmberg, 2010), direct exposure to near-field blast conditions would be lethal. Therefore, a majority of blast-induced mild TBIs occur from far-field blast exposure, so laboratory generated planar shock waves will accurately simulate primary loading from an IED.

One example of the power of IEDs in Afghanistan is given in an article by the Associated Press titled “Roadside bomb kills 10, wounds 28 in Afghanistan” (Shah et al., 2011). This demonstrates the power of these explosives and the lethality at close ranges, giving credibility to the planar shock wave assumption. A typical free-field blast wave takes the form of a planar Friedlander wave at a significant distance from the explosion source location. This wave has the characteristics of positive-pressure phase decaying to ambient pressure, followed by a negative pressure phase as shown in Figure 1-2.

A developed blast wave generated by a shock tube takes the Friedlander form inside the shock tube and is constrained to propagate in a single direction. Upon exiting the shock tube, the lateral constraint of the shock tube is no longer present, and the wave is allowed to propagate in all directions. Although a free field blast propagates in 3 dimensions, it does so continuously. The shock wave exiting a shock tube has a discontinuity to overcome, and preliminary research has shown the flow outside a shock tube is very turbulent as shown in Figure 4-1 (Jiang, et al., 1999). Based on the previous statements it was hypothesized that the wave properties will significantly change upon exiting the shock tube and will not effectively represent blast waves generated by IEDs.

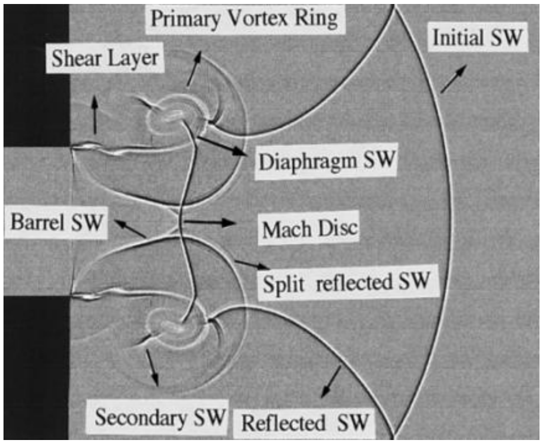

Figure 4-1: Turbulent flow induced by abrupt change in area at a shock tube exit (Jiang, et al., 1999).

4.2 Experimental setup

The shock waves generated for this experiment used the 9 inch square shock tube which is 20 feet long and driven by a 4 inch diameter driver section with a length of 11.625 inches. Pure pressurized nitrogen was used as the driver gas, and the driven gas was air at ambient laboratory conditions (temperature range of 72° +/- 2° Fahrenheit).

The comparison of shock wave loading was done inside and outside the shock tube using an aluminum cylinder as demonstrated in Figure 4-2. The cylinder was 9 inches long with a diameter of 1.625 inches. Seven holes were drilled and tapped through a central plane for mounting the Dytran model 2300V1 piezoelectric pressure sensors, as shown in Figure 4-2a. The location labeled t0 was centered on the cylinder, and the rest of the holes were evenly spaced for a total span of 3.30 inches. The cylinder was placed at various offsets from the exit of the shock tube both external (+d) and internal (-d) as shown in Figure 4-2b. Similarly, testing was done at the orientations of 0°, 45° and 90°. The cylinder was externally mounted using a bracket made out of 1.5" × 0.25" steel flat bar to space the cylinder at various distances.

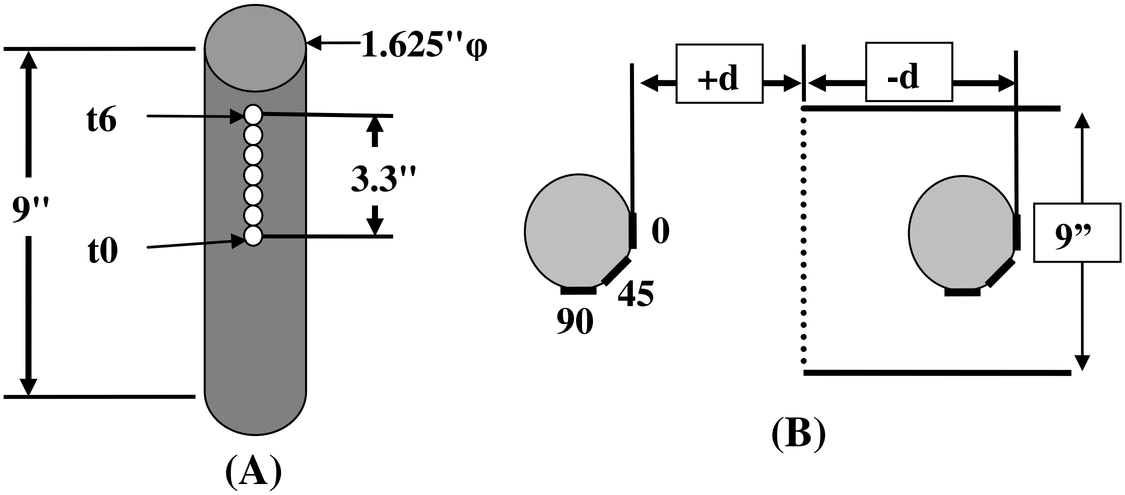

Figure 4-2: (A) Cylinder with 7 pressure sensor array with t0 located at center, t6 located 3.3 inches above center and even spacing in between. (B) Cylinder test configuration at various distances and orientations from the exit of the 9 inch square shock tube.

A typical shock wave profile taken in the test section (120 inches from the shock tube exit) is shown in Figure 4-3 and has the main characteristics of a Friedlander profile. Due to consistent burst pressures the average peak pressure (100 point peak average) for all shots was determined to be 16.6 psi with a standard deviation of 0.65 psi.

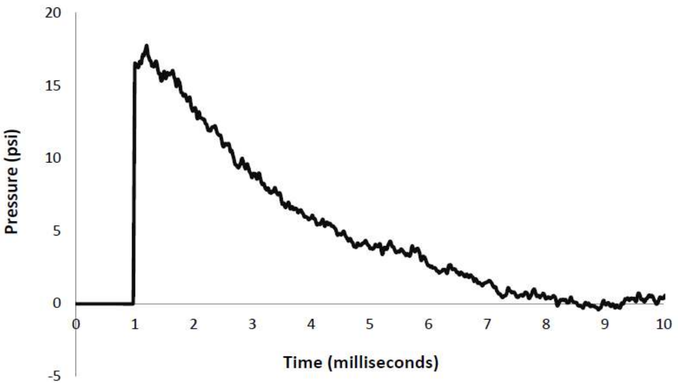

Figure 4-3: Incident shock wave profile measured on the side wall of the 9 inch shock tube with no sample in place. Typical profiles have a peak pressure of 16.6 psi with a standard deviation of 0.65.

4.3 Results

The cylinder loading is compared using three different methods in this section. The first section directly compares pressure and impulse profiles at various locations and orientations. The second comparison technique looks at the peak pressures observed at various sample locations. The final comparison technique measured the planarity of the shock front with varying distance from the shock tube exit. The shock wave profiles shown have been filtered using a running average of 25 points to reduce the noise associated with the Dytran sensors.

4.3.1 Pressure and impulse profile comparison

A comparison of the pressure profiles at various offsets at the 0° orientation is given in Figure 4-4. This includes several tests placed outside the shock tube and one test taken in the test section (120 inches from the exit). One important feature of this comparison is that the sample placed inside the shock tube displays gradual pressure decay while the external samples experience a rapid pressure drop (A) followed by a long duration, relatively constant low pressure regime (B). This rapid pressure drop for external sample placement is induced by the lack of the shock tube constraint, allowing gas expansion in three dimensions. The short duration spike is characteristic of close proximity to a very small explosive, which is not characteristic of typically large IED's. The lower pressure regime that follows the pressure spike is induced by the high velocity expansion jet imparting kinetic energy on the cylinder surface, which is likewise not characteristic of a blast wave in general. Verification of the jet flow component is given by the following statement: "it can be concluded that the jet-flow exiting from the shock tube is high velocity, very turbulent, relatively narrow, and can add significantly to target loading (Kingery & Gion, 1989)."

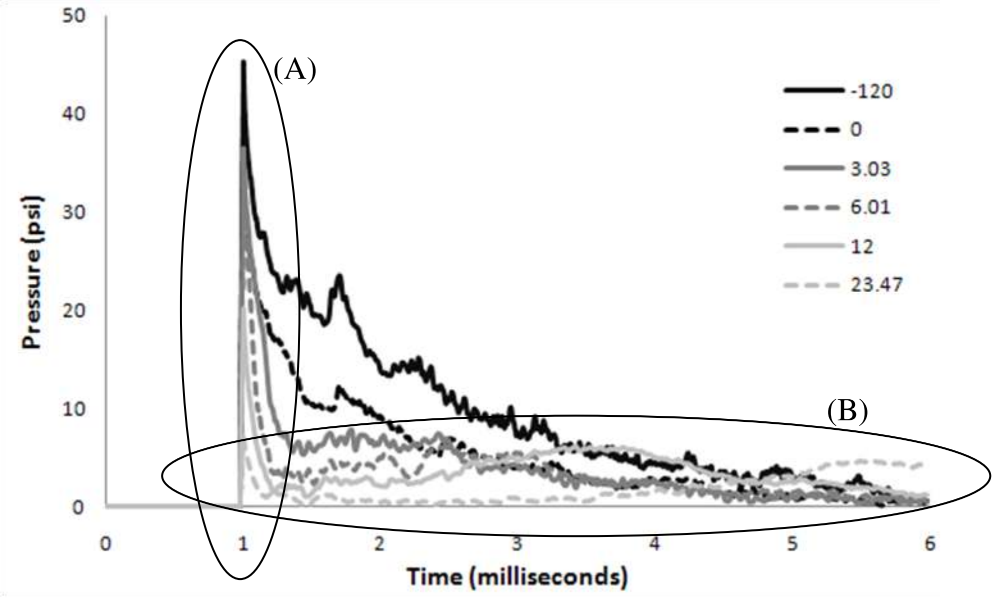

Figure 4-4: Pressure measurements at the center sensor (t0) at 0° orientations with multiple offsets including the test section (-120”).

One disadvantage of placing samples inside the shock tube is the internal reflections which can be seen in the small pressure spikes in the -120" and 0" pressure profiles shortly before the 2 millisecond marker. The internal reflections can be minimized by using a small sample relative to the shock tube cross sectional area. A rule of thumb mentioned by Ritzel (2009) is to block no more than 10% of the shock tube cross sectional area to achieve minimal interference. This could pose a problem towards performing large-scale experiments inside of a shock tube due to the required shock tube size.

The total impulse of shock profiles is another method of examining the energy through integration of a pressure history, and is demonstrated for the center sensor (t0) at the 0° orientation with multiple offsets in Figure 4-5. Not only are the peak magnitudes of the impulse significantly different, but the shapes of the impulse profiles are also significantly different. The extreme loading difference at small offset changes shows that the flow does not represent a planar shock wave, which is an accurate representation of a far-field blast. At offsets of 12” and 23.47” the primary sample loading is induced by jet flow, which is not a good representation of primary blast loading. The initial pressure spike has very little contribution to the loading. Impact induced TBIs have different symptoms than blast induced TBIs, so it is likely that the injury mechanisms are also different for “jet flow” induced TBIs.

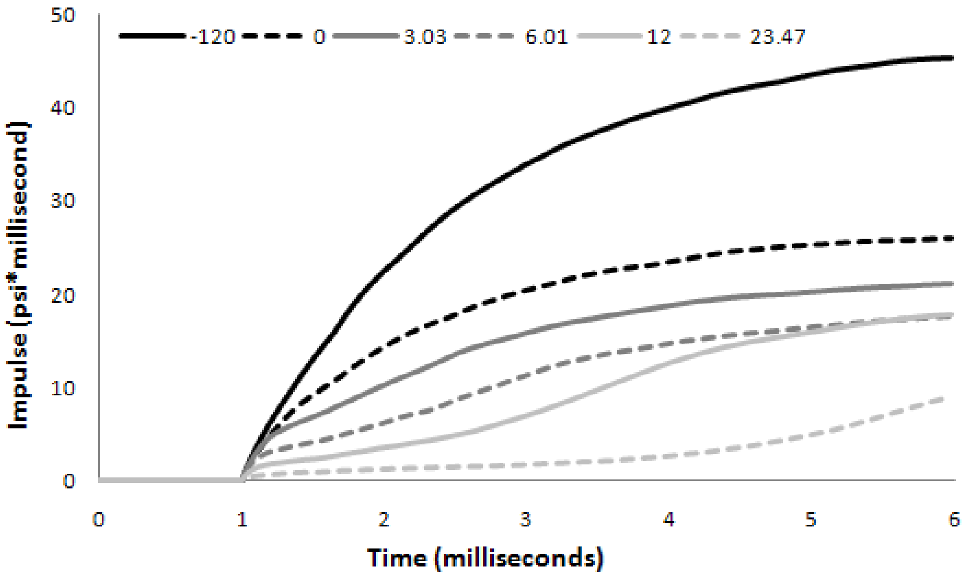

Figure 4-5: Impulse profiles taken at the center sensor (t0) from the 0° orientation with multiple offsets including the test section at -120".

A comparison of the pressure and impulse histories at various orientations in the test section is shown in Figure 4-6. The 0° and 45° orientation shows gradual pressure decay, but the 90° orientation shows flow separation from the cylinder causing a negative pressure phase. This negative phase cannot be sustained and the pressure profile oscillates twice before semi-equilibrating around the other profiles. A slight internal reflection in the 90° profile coincides with the first positive pressure rebound around 1.5 milliseconds, but the significance of this can be minimized by using a sample that does not excessively block the shock tube cross section (~10%). The 0° orientation experiences the highest pressure because of the kinetic energy contribution from the reflected pressure.

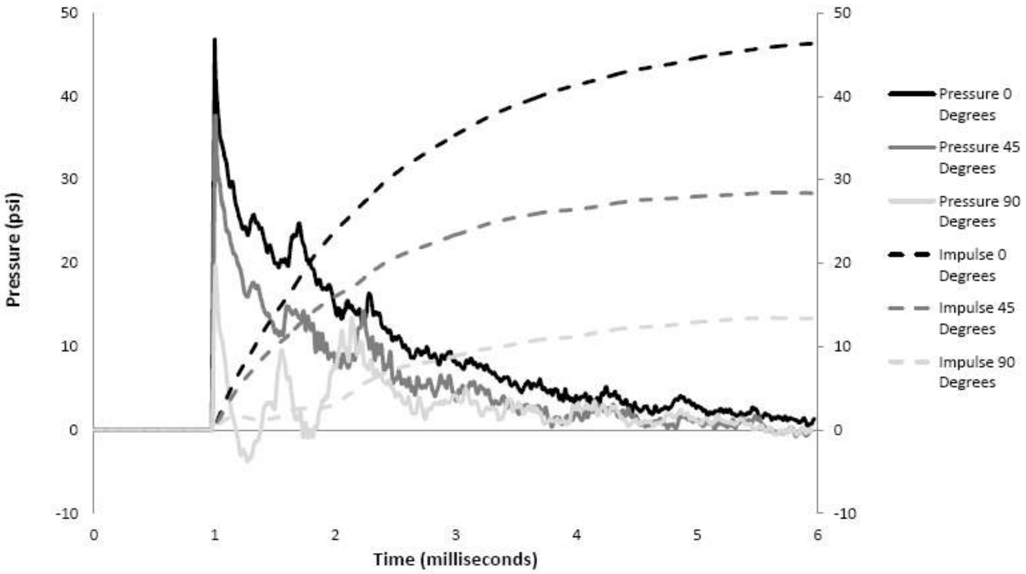

Figure 4-6: Pressure and impulse histories at the middle sensor (t0) on the cylinder at 0°, 45°, and 90° taken in the test section (120 inches from the shock tube exit).

Figure 4-6 shows the pressure and impulse profiles at the center sensor (t0) for the three orientations at a three inch offset from the shock tube exit. All three orientations show a rapid pressure drop after the peak pressure. Following the short pressure spike the 0° orientation experiences pressurization caused by jet flow but the 45° orientation pressure drops to zero with a slight vacuum. The sensor at the 90° orientation also exhibits flow separation and oscillation, but the pressure mainly remains negative due to the lack of lateral constraints. The high velocity air passing by the cylinder in combination with the 3-D expansion causes the pressure to drop based on Bernoulli's principle. The loading on the back cylinder surface is unknown, but likely has large vacuum pressures as well.

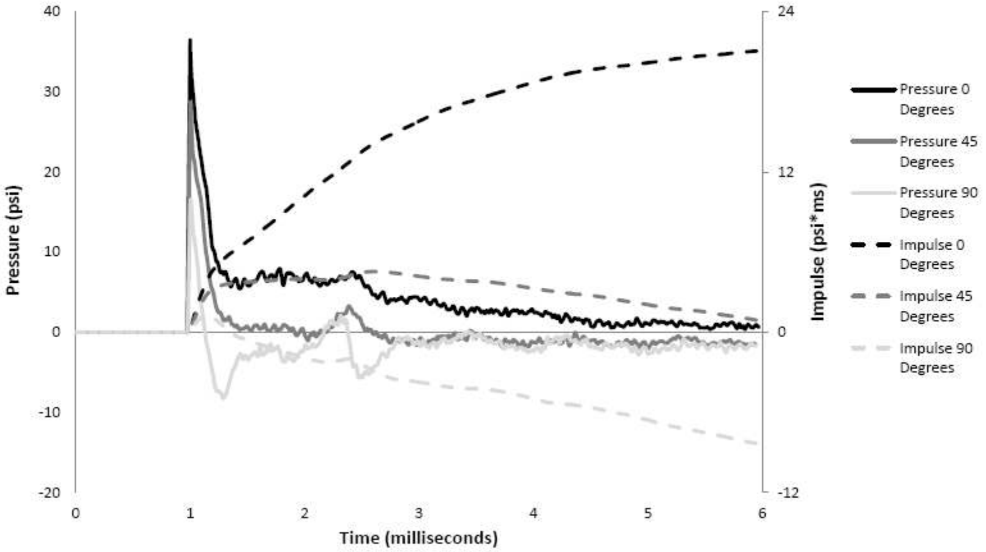

Figure 4-7: Pressure and impulse histories measured using sensor t0 at 0°, 45°, and 90° placed 3 inches from the shock tube exit.

4.3.2 Peak pressure comparison

A summary of the peak pressures measured at the center and edge sensors t0 and t6 respectively is given in Table 4-1. The peak values were determined by using a 10 point average after the first local maximum after the shock front arrival. More data points were not used because the peak pressure dropped rapidly at the 90° orientation and all other orientations outside of the shock tube.

Table 4-1: Summary of peak pressures at sensors t0 & t6 (see Figure 4-2)

Distance (inch)	**Peak Pressure t0**			**Peak Pressure t6**		
	0°	**45°**	**90°**	**0°**	**45°**	**90°**
23.5	**7.30**	**6.11**	**3.85**	**7.36**	**6.39**	**4.26**
17.9	**11.5**	**9.26**	**5.52**	**11.7**	**9.73**	**6.15**
15.4	**14.3**	**10.6**	**6.46**	**14.4**	**11.1**	**7.22**
12.0	**20.3**	**15.6**	**8.75**	**19.5**	**15.7**	**9.31**
9.0	**31.0**	**21.6**	**11.7**	**25.6**	**19.2**	**11.1**
6.0	**34.1**	**28.2**	**17.0**	**26.0**	**22.4**	**13.4**
6.0	**36.3**	**28.4**	**16.9**	**27.7**	**22.7**	**13.3**
5.0	**35.9**	**26.4**	**17.1**	**27.6**	**20.9**	**13.5**
4.0	**35.6**	**26.7**	**16.4**	**28.2**	**21.5**	**13.0**
3.0	**36.5**	**28.7**	**16.6**	**31.6**	**24.7**	**13.5**
2.0	**40.0**	**28.8**	**17.4**	**39.1**	**27.1**	**15.2**
1.0	**36.6**	**31.0**	**16.5**	**38.2**	**32.3**	**15.9**
0.0	**35.3**	**28.8**	**16.2**	**36.8**	**30.4**	**16.4**
-2.3	**38.2**	**27.4**	**17.0**	**40.9**	**30.1**	**18.4**
-12.3	**37.4**	**29.6**	**15.6**	**39.6**	**32.8**	**17.8**
-22.3	**38.0**	**31.7**	**16.9**	**40.8**	**35.4**	**18.6**
-120	**46.8**	**37.6**	**19.7**	**50.1**	**43.7**	**23.4**
-120	**45.3**	**37.1**	**18.6**	**49.2**	**43.0**	**22.0**

A graphical representation comparing the peak pressures at sensors t0 and t6 in the 0° orientation demonstrate the pressure gradients outside of the shock tube. Figure 4-8 shows significant pressure gradients at increasing distances along the shock propagation direction (A) as well as along the axis of the cylinder (B). The non-uniformity between the two sensors between the 2” and 12” offsets demonstrates the radial flow expansion (B), followed by the development of a uniform shock front after 12 inches. However, the results from the previous section show that the primary loading at these offsets is caused by jet flow, which is not even characteristic of a blast wave. The blast energy has also greatly diminished at greater distances. These conclusions explain the presence of the turbulent flow, excessive vacuum, and vortices present around a shock tube exit.

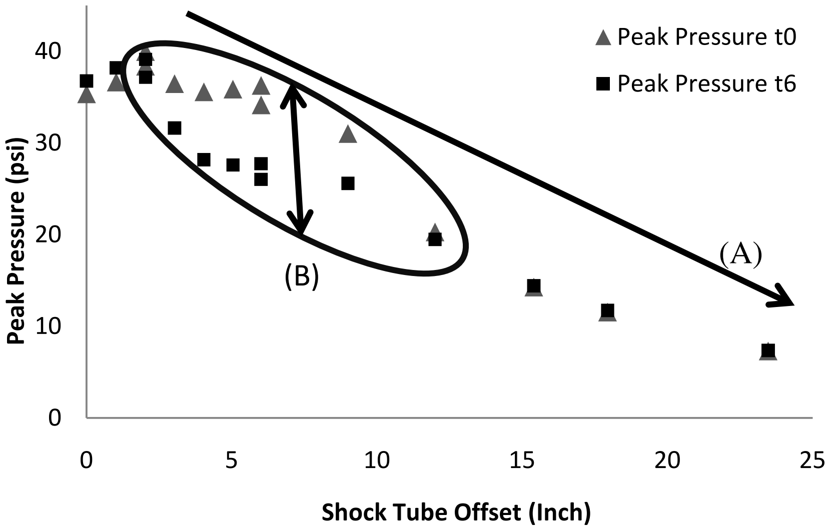

Figure 4-8: Peak pressure summary for cylinder offsets of 0 to 24 inches from the shock tube exit using sensors located at t0 and t6.

A comparison of the actual pressure profiles at t0 and t6 is shown in Figure 4-9 for offsets of 0 and 6 inches. These profiles are shown to demonstrate the actual differences shown in Figure 4-8. The profiles are nearly identical for the zero offset, but show significant differences at the 6 inch offset. The 12 inch offset profiles are not shown, but the peak pressures re-stabilized to identical levels. The oscillations in sensor t6 are likely due to sensor imperfections and are not considered to accurately represent reality.

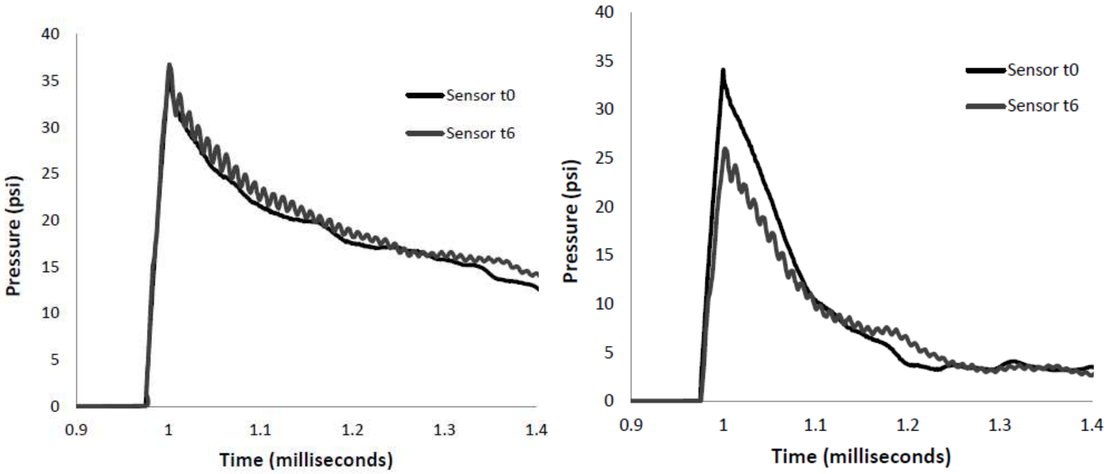

Figure 4-9: Comparison of the 0° profiles at locations t0 and t6 (see Figure 4-2). The left figure had an offset of 0 inches and does not have a significant pressure difference between sensors. The right figure had an offset of 6 inches and exhibits a peak pressure decrease of 25% for sensor t6.

4.3.3 Shock front planarity test (arrival time)

The results from both of the previous sections suggest non-uniform expansion which would potentially create a non-planar shock front. Verification of this hypothesis is done by measuring the shock front planarity by measuring the arrival times at each sensor and normalizing them to the arrival time of the center sensor (t0). The arrival time differences were plotted in Figure 4-11 in 1 millisecond increments. The results show later arrivals with increased distance from the center sensor (t0), leading to the conclusion that the shock front is non-planar.

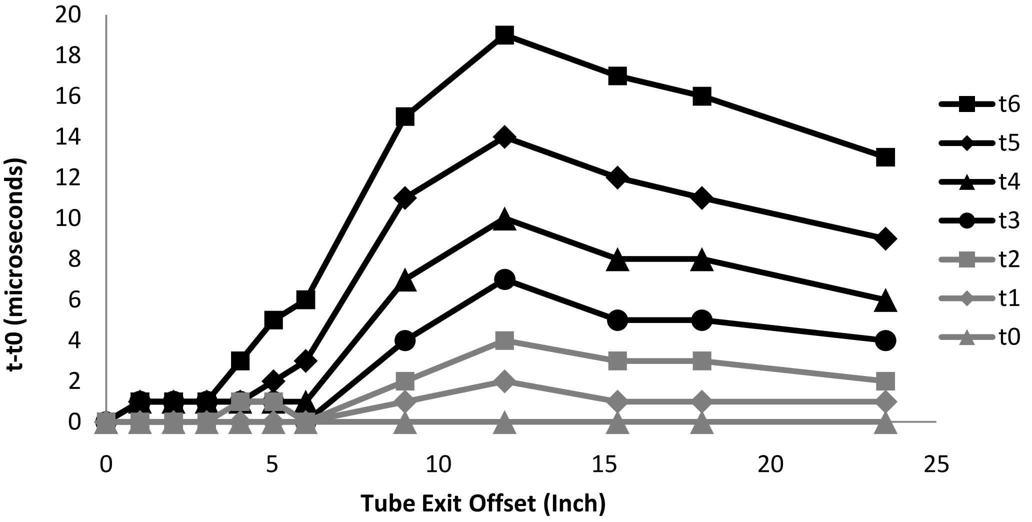

Figure 4-10: The normalized arrival times at all sensor locations t0 to t6 are shown to demonstrate the non-planarity outside of a shock tube. Upon exiting the shock tube a planar wave becomes progressively non-planar until peaking at a 12 inch offset and then becomes increasingly planar.

It was observed that the arrival times increased out to a distance of 12 inches, and then decreased after that. The non-planar trend out to 12 inches shows the shock front transitioning from 1- to 3-D expansion. The increasing planarity after the 12 inch offset also makes sense because the planarity of spherical expansion increases with increasing radius from the source. The maximum out of plane distance between sensors t0 and t6 is conservatively 10 mm (potentially more) which corresponds to a blast radius of approximately 14 inches, which is not pertinent to typical blast loading in the mild TBI range. The diagram shown in Figure 4-11 illustrates the planarity of the shock front as it progresses outside of a shock tube.

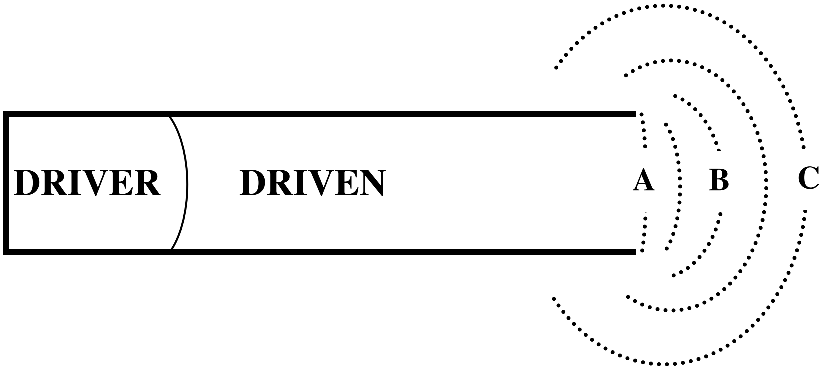

Figure 4-11: Planarity development outside a shock tube. (A) Planar shock front at the shock tube exit. (A to B) Decreasing shock front planarity until a maximum non-planar state. (B to C) Increasing shock front planarity with progressive distance.

4.4 Discussion

The shock wave loading on a cylinder was shown to be significantly different for tests inside and outside a shock tube. Outside the shock tube and near the exit, an expansion wave significantly degrades the blast profiles measured on a cylinder surface.

For tests placed close to the shock tube exit the peak pressures did not significantly change, but the profile after the peaks are drastically different. Samples placed outside the shock tube also experienced excessive vacuum pressures induced by the discontinuous 3-D expansion and jet flow. The positive pressure that was experienced by samples placed outside the tube was significantly caused by kinetic energy buildup from high speed jet flow. The shock front transitioned from planar to a maximum non-planarity out to 12 inches from the exit and then became increasingly planar at further distances. Data from Jiang et al. (1999) was used to visually indicate the presence of vortices and turbulence of a shock wave exiting a shock tube. The pressure histories at different orientations on a cylinder were observed and it was found that flow separation occurs at the 90° orientation and oscillates until semi-equilibrating with the 0° and 45° pressure profiles.

Based on these measurements, it is suggested that caution is taken when testing samples outside of a shock tube because of the non-uniform loading in this region. Excessive vacuum pressures associated with external jet flow do not effectively replicate the loading scenarios caused by IEDs during current military conflicts. The most realistic approach to generating blast waves for TBI studies would be to use actual explosives in field conditions. This is not always practical, so a very good approximation to far-field blasts can be obtained by placing samples inside of a shock tube.

Chapter 5: Development and Characterization of a 28-inch Shock Tube

This chapter discusses the development of a 28-inch shock tube for testing full-scale head models for researching traumatic brain injuries. Previous research has shown that the significant differences in loading exist between sample placements inside vs. outside a shock tube. The overall design considerations and component details are discussed along with operational procedures. Several characterization experiments were performed to generate shock profiles with varying overpressure, impulse, duration, and shape.

5.1 Introduction

Chapter 4 discussed the significant changes to shock wave and flow properties near the exit of a shock tube. These conclusions led to the idea that simulated blast waves optimally match a Friedlander wave if the experiment is placed inside a shock tube. One disadvantage of performing experiments inside of a shock tube is the presence of reflections from the tube walls, which can be minimized by reducing the size of the experimental sample. A rule of thumb was suggested by Ritzel (2009) that the area of the sample blocking the shock tube should be less than approximately 10% of the shock tube cross sectional area.

The research goal of the shock facility is to better understand the mechanisms that cause TBIs, so the development of a large-scale shock tube began because of the necessity to test a full-scale human head model under blast conditions. Approximate measurements determined that the frontal cross sectional area of a human head is roughly 65 square inches. A 28-inch square shock tube has a cross sectional area of 784 square inches, providing adequate area for testing a full-scale head model without experiencing significant internal reflections.

5.2 Component designs

The final design for the 28-inch shock tube is shown in Figure 5-1. The four main components to the shock tube are the driver, transition, straight sections, and the catch tank. The straight section includes the test section as well as extension sections. The driver contains pressurized gas which is separated from the transition by several membranes. Upon membrane rupture a shock wave expands through the transition and develops in the extension section(s). Experiments are placed in the test section which is strategically placed to produce a desired shock wave profile. Finally the shock wave exits the shock tube and enters the catch tank which absorbs and "slowly" releases most of the shock energy and reduces the noise intensity. Component information is given in greater detail in the following sections.

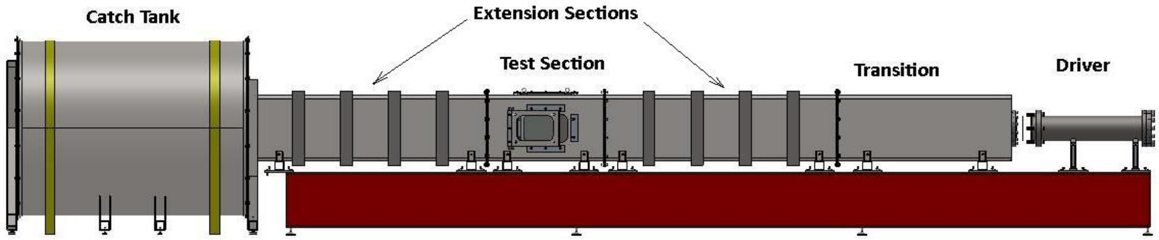

Figure 5-1: Schematic of the 28-inch shock tube system

5.2.1 Driver section

The shock tube driver is the section where the energy for the shock wave propagates from. There are two widely used methods for generating high pressure in the driver, rupture membranes and combustion, although a third method using fast acting valves has been considered. For safety purposes, the combustion method is not used in UNL's shock facility. Likewise, a fast acting valve for shock tube applications has not been researched in detail and the use has not been attempted at UNL. Therefore, the rupture membrane method has been employed to drive the 28-inch shock tube. A larger diameter driver was needed for the 28-inch shock tube, so an inner driver diameter was chosen to be 8 inches. A larger diameter could have been chosen, but larger membranes tend to burst with less uniformity and produce more fragmentation upon rupture.

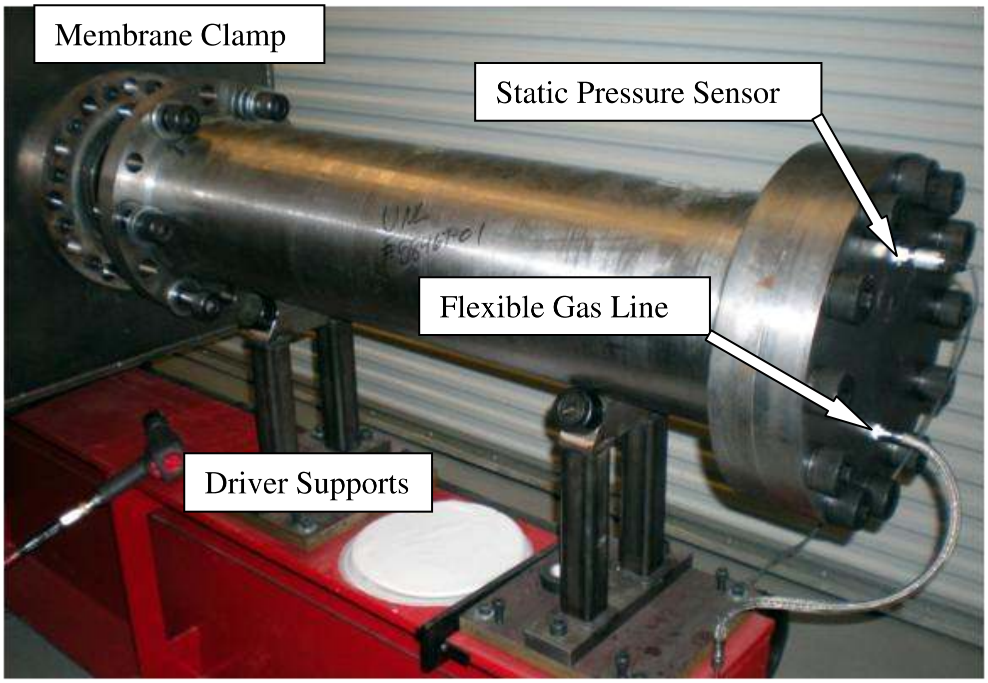

Figure 5-2: Driver section (8 inch inner diameter, 48 inches long) for 28-inch shock tube. The driver rests on rolling supports and is pressurized through a flexible gas line using Mylar rupture membranes. Pressure data is measured using a static pressure sensor.

Although breech pressures above 1000 psi were not expected using Mylar membranes, the maximum breech pressure was designed to be 3000 psi so the system could be easily adapted if higher pressures were desired through the use of metallic membranes. The breech material is mild steel with a yield strength of 36 ksi, which produces a safety factor of approximately 3.5 using thick wall pressure vessel calculations (Engineering ToolBox) and maximum octahedral stress criteria (Boresi & Schmidt, 2005). Mild steel was chosen because of its low cost, ease of machining, availability, and ductile properties. The breech flanges were welded using multiple pass groove welds and ground smooth. One flange is used for the membrane clamping and the other flange is used for closing the back of the driver. Figure 5-2 shows the completed driver section. The driver is pressurized via a flexible gas line which is threaded into the back of the breech. The back plate is sealed with a 1/8" face sealing O-ring as specified by allorings.com (2003).

5.2.1.1 Driver Supports

The driver supports consist of a weldment and roller assembly designed to align the driver section with the 28" shock tube. The driver rests on 2 inch diameter rollers allowing it to be slid back for membrane loading. There are four adjustment bolts mounted in the part labeled "base plate" which are used for aligning and leveling the breech, as shown in Figure 5-3. The other set of four bolts are used to anchor the supports to the I-beam after the driver is properly aligned with the transition section.

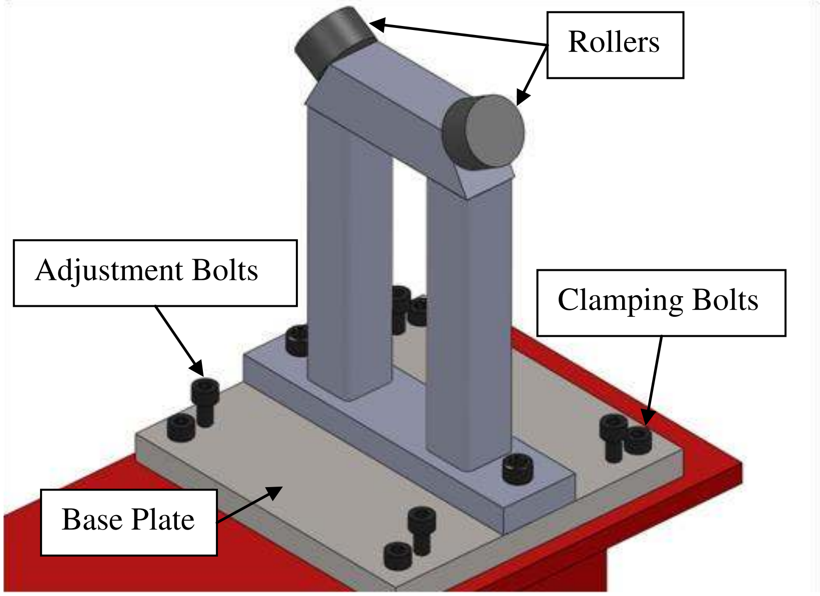

Figure 5-3: Support assembly for the 8 inch driver section

5.2.1.2 Driver length adjustment

Previous experience with UNL's 9 inch square shock tube using a 4 inch diameter driver showed that a 12 inch driver length using nitrogen was sufficient for generating a Friedlander wave. Longer driver lengths produced flat topped waves, which were not the goal of the 28-inch shock tube system. Longer driver sections could be used to generate a Friedlander wave with helium, but the full length of 6 feet was not necessary. Based on this previous knowledge the driver length was chosen to be 4 feet.

Although the driver is 4 feet long, the ideal driver lengths to generate a Friedlander wave were unknown. Therefore, 8 inch diameter aluminum inserts were machined in lengths of 18, 12, 6, 4, and 2 inches. These inserts can be used individually or connected together using 1”-8 threaded studs to set the driver length from 48 inches to 6 inches in increments of 2 inches. Figure 5-4 shows a cross section of the breech using the 18, 12, and 6 inch breech plugs to create a driver length of 12 inches. The inner diameter of the driver is approximately 0.030 inches larger than the breech plugs which creates a path for incoming gas to flow to the main driver volume.

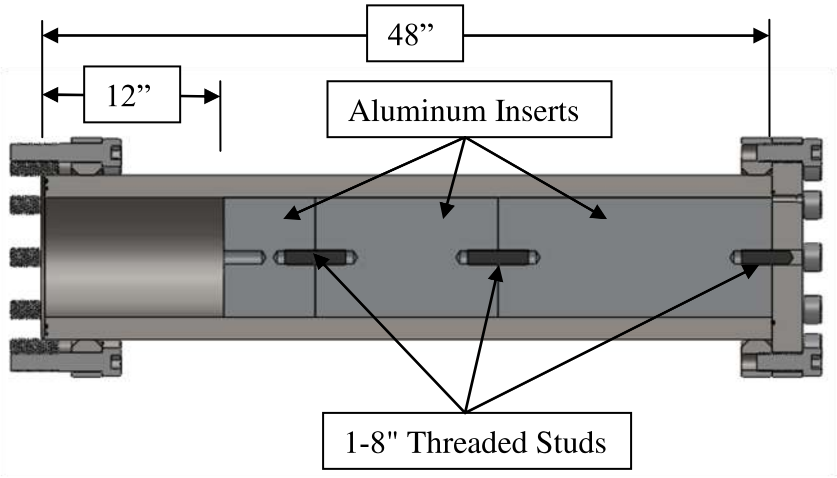

Figure 5-4: Cross sectional illustration of the driver section showing the use of the 18, 12, and 6 inch inserts to create a 12 inch driver length. The driver length can be adjusted from 6 to 48 inches in 2 inch increments.

5.2.1.3 Membrane clamping mechanism

Typical materials for rupture membranes are Mylar or ductile metals such as stainless steel and aluminum. One of the drawbacks of using metallic membranes is the possibility of high density fragments which could destroy sensors or experiments. Metallic membranes are also expensive. Therefore, Mylar was chosen as the membrane material for ease of use, consistency, and low cost. Fragmentation of Mylar does occasionally occur, but the material is significantly less dense and has not caused any sensor damage.

Figure 5-5 is an illustration of the membrane clamping mechanism. One clamping surface is machined directly into the driver section, which contains two o-rings of 9” and 10” inner diameters respectively. The mating surface has two o-rings with inner diameters of 8.5” and 9.5”. This alternation of o-rings crimps the membranes and prevents slipping when the clamping bolts (1.25”-12 × 6” length) are tightened. A lip on the breech ensures proper alignment of the membrane clamps.

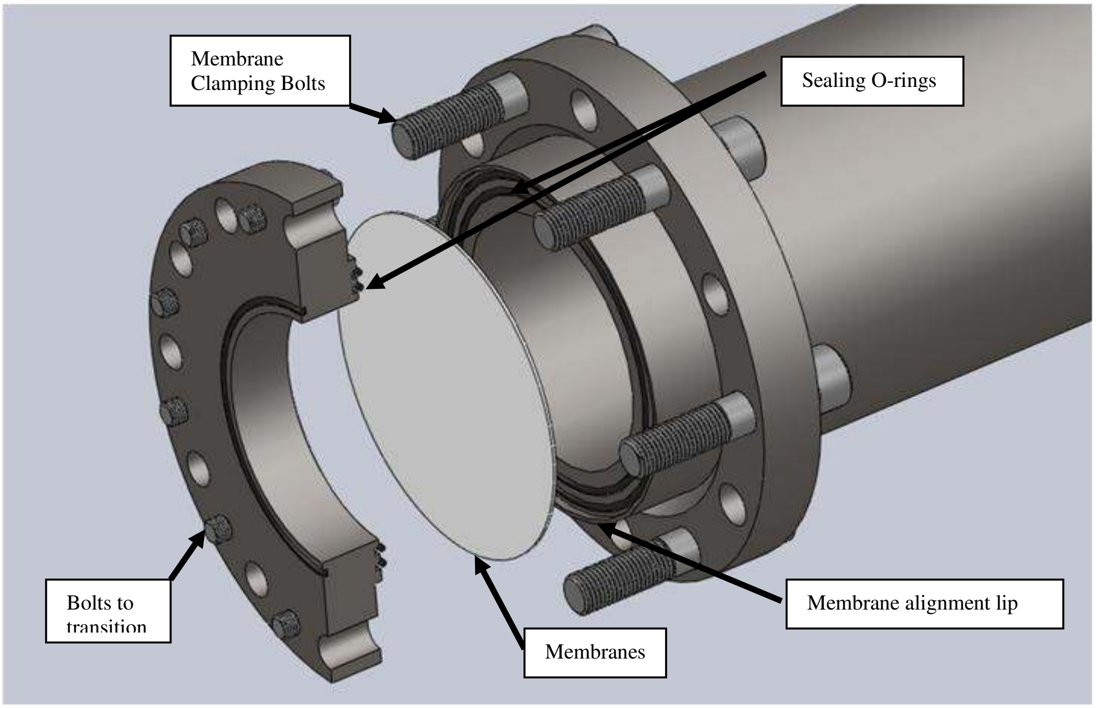

Figure 5-5: Partial cross section of the membrane clamping device for the 8 inch driver. Up to twelve 1.25” dia. bolts are used to clamp membranes together while four O-rings are used to seal in pressure and prevent the membranes from slipping.

When membranes are installed the bolts should be tightened in a star pattern to ensure uniform torque and proper sealing. For experiments with burst pressures under 1000 psi it is sufficient to use only six of the twelve clamping bolts with an applied torque of approximately 400 ft-lbs. Higher pressure tests would require use of all of the clamping bolts to prevent the driver gas from leaking. Similar to the tightening procedure, the bolts should be loosened gradually in the star pattern to prevent load concentrations in single bolts.

5.2.2 Transition

The transition section connects the 8 inch diameter driver to the 28-inch square driven section, and is shown in Figure 5-6. The transition was designed with a gradual expansion to minimize flow separation and turbulence associated with abrupt changes in cross sectional area. The transition was fabricated in two sections using brake forming and was welded at the seams. The length of the transition is 72 inches which produces an expansion angle between 8.0° and 11.25°, depending upon the angular position. The 11.25° angle is measured between the outer 8 inch diameter and the corner at the far end of the transition and the 8.0° angle is measured along the cut-plane shown in Figure 5-6.

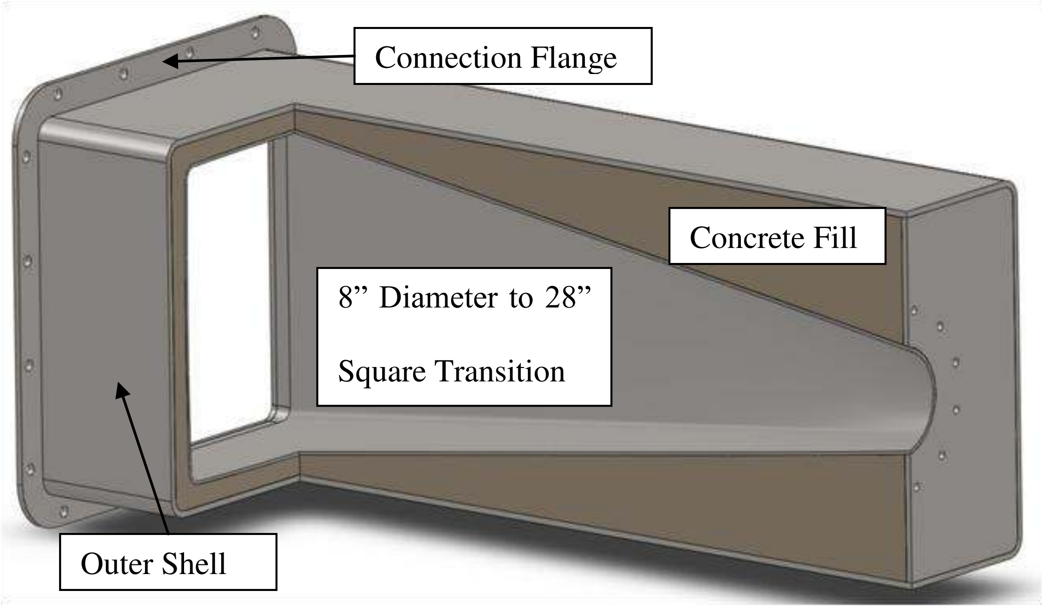

Figure 5-6: Cross section view of transition which connects the 8 inch diameter driver to the 28-inch square driven section. The transition was formed from ¼” steel sheet and was designed to be filled with concrete to improve rigidity if necessary.

The transition shell is mounted inside of a 6 foot long straight section of 28” square tube for ease of alignment with the other tubes. Filling the space between the 28-inch tube and transition with concrete has been considered to improve rigidity and decrease vibration, but has not currently been done because of the increased weight to the system. Approximately 3000 pounds of concrete would be required to fill this space making it impossible to lift with the two hoists in the lab (1000 pound capacity each). The connection flange is used for fastening the transition to the straight 28-inch sections.

5.2.3 Modular 28-inch sections

The 28-inch shock tube has a modular design so the test section could be placed at various locations by switching the tube layout. Six sections of the 28-inch tube were manufactured: two 8 foot sections, three 4 foot sections, and one 2 foot section. Using these components the test section can be placed from 0 to 20 feet from the transition, although 2 feet and 8 feet are the advised locations that were tested.

The sections of the 28-inch shock tube were each fabricated out of two 29 inch wide and 14.5 inch high channel shaped sections with half inch thickness. These were welded with a full penetration weld at the seam and ground smooth on the inner surface. Flanges were welded to the ends of each section for bolting sections together using sixteen ¾ inch bolts. The extension sections and the test section will be described in further detail.

5.2.3.1 Extension sections

Finite element analysis for the original shock straight extension sections is shown in Figure 5-7A. Finite element analysis showed that pressurizing an 8 foot section to 20 psi produces a stress of 18,700 psi which corresponds to a safety factor of approximately 1.93 for the imposed loading. The analysis also showed a maximum out-of-plane deformation of 1.89 mm. Initial shock testing of these tubes showed excessive vibration of sensors and stress levels of approximately 21,000 psi using a 20 psi Friedlander wave. The rigidity was improved significantly by adding four “circumferential” braces made of 5×9 channel iron (5 inches wide & 9 lbs per foot). The finite element comparison produced a maximum stress of 7,700 psi with a maximum deflection of 0.265 mm. This produces a safety factor of approximately 4.68 which is a strength improvement of 2.4 times. The highest peak pressure that has been generated is 42 psi, but experimental verification should be carried out if pressure levels above 50 psi are attempted.

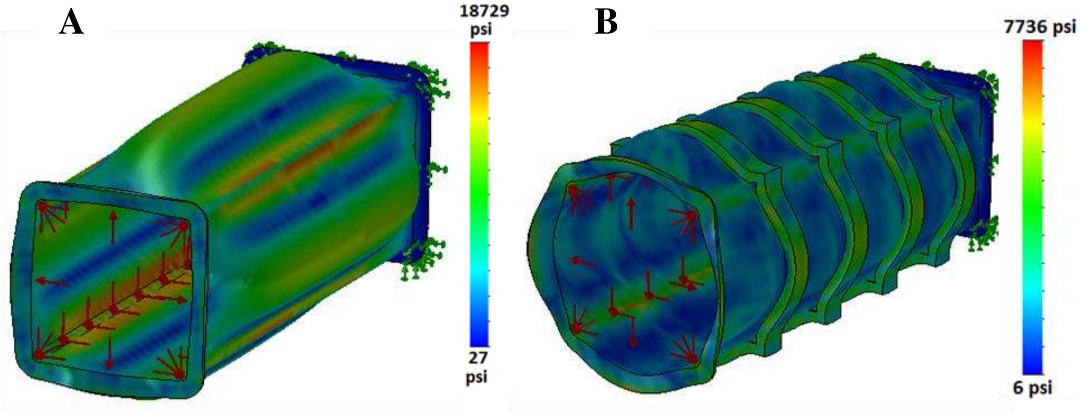

Figure 5-7: Von Mises stress distribution in 28-inch tubes under 20 psi static pressure loading. Adding supports as shown in Figure B reduced the stress from 18,700 psi to 7,700 psi and the maximum displacement from 1.89 mm to 0.265 mm. Material yield strength is 36,000 psi.

5.2.3.2 Test section

The test section shown in Figure 5-8 is a four foot section of tube used for experiment placement and data collection. The modular nature of the 28-inch shock tube allows the test section to be placed in locations designed for specific shock wave profiles. It has three large access locations (12.5” by 18.5”) cut for windows and mounting plates. The windows are used for viewing samples under shock loading and the mounting plates are used for mounting sensors and samples. The importance of mounting sensors in the rigid mounting plates is emphasized by the results shown in Figure 2-12. This figure shows extreme variations observed when mounting a PCB sensor in the thick (1.5”) mounting plate vs. the thin shock tube wall (0.5”).

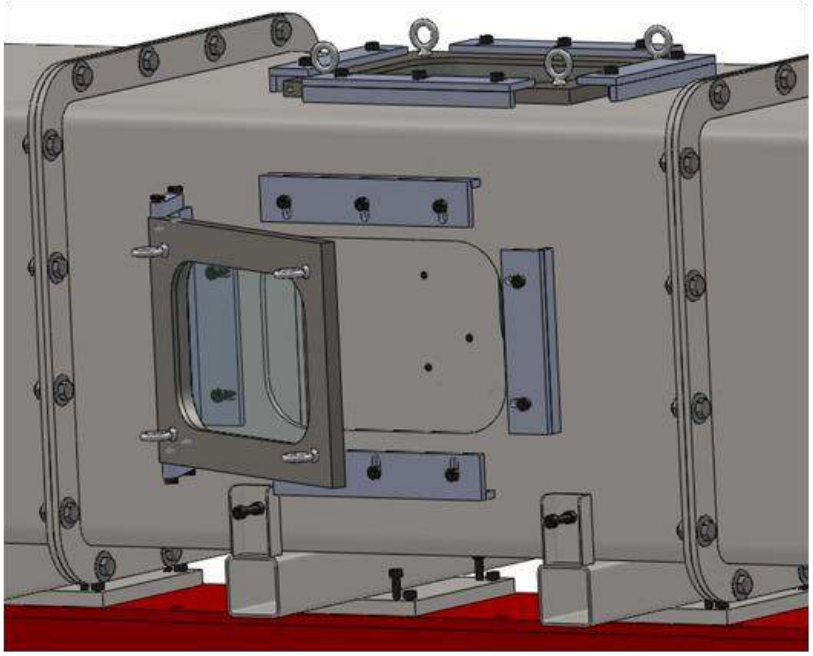

Figure 5-8: Test section of 28-inch shock tube. The side viewing windows open on hinges and are held closed with four sliding clamps. The top window is equipped with lifting rings for simple removal. A 1.5” thick sensor mounting plate is located on the opposite side of the front window. Experiment mounting is done using holes on the bottom of the test section.

All windows and mounting plates are configured with lifting rings, hinge mounting points, and an o-ring groove. The side windows are mounted on hinges for easy access and the upper window uses lifting rings and the hoist for access. The clamps for holding the windows closed consist of a sliding angle clamp on each side of the window for a total of four clamps and 12 bolts.

The window glass dimensions are 18” wide, 12” high, and 1.25” thick and was cut from bullet resistant glass with five laminated layers. The window is supported against positive pressure from the shock tube by a ½ inch lip on the window frame creating a viewing area of 11” by 17”. The window is glued in place to constrain it from negative pressure in the shock tube.

It is important to note that the use of high wattage lighting should be minimized to prevent thermal stresses from forming in the various lamination layers. One window was exposed to a 700 watt lamp for 20 minutes and experienced cracking from thermally induced stress.

5.2.4 Catch tank

The catch tank was designed to contain and slowly release the large volume of expanded gas generated from a shot, minimizing blast loading of lab structures and reducing noise level. The use of a suddenly changing cross sectional area was studied and found to successfully mitigate energy (Jiang et. al, 1999). The inside of the catch tank is lined with carpet for sound absorbing purposes. The catch tank was primarily designed for the 28-inch shock tube, but an opening was cut allowing the 9 inch shock tube to be mounted on top of the 28-inch tube and inserted into the catch tank.

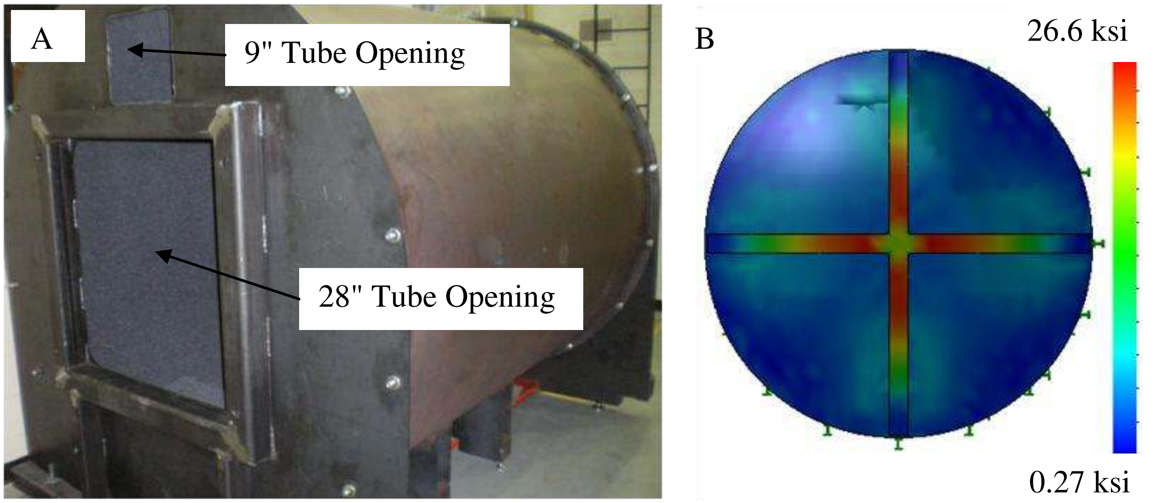

Figure 5-9: (A) The catch tank is designed to contain and mitigate shock energy and contains openings for the 28" and 9" shock tubes. The inside is lined with carpet for greater noise reduction. (B) Finite element analysis of the back side produced a safety factor of 1.35 (36 ksi yield) with an exaggerated static load of 20 psi.

Finite element analysis was performed on the catch tank using an internal pressure estimate of 20 psi, which is very conservative considering that the area of the catch tank is 5.8 times the area of the 28-inch shock tube. This showed a safety factor against yield to be 1.35 under these conservative loading conditions. The catch tank rests on adjustable feet and is moved into place using a 6 foot pallet jack. 5000 lb ratchet straps and concrete anchors are used to anchor the catch tank to minimize motion induced by a blast. When the catch tank is not strapped down movement of up to 4 inches has been observed, but large displacement of the catch tank is not a danger.

5.3 Membrane burst characteristics

Mylar membranes of 0.01 inch thickness are used to contain the pressurized gas in the driver section until rupture, allowing a shock wave to propagate down the shock tube. The outer diameter of the membranes was cut to 10.63 inches using water jet cutting, and the inner diameter of the breech is 8 inches. The flat membranes deform upon pressurization in a hemispherical manner until rupturing as shown in Figure 5-10.

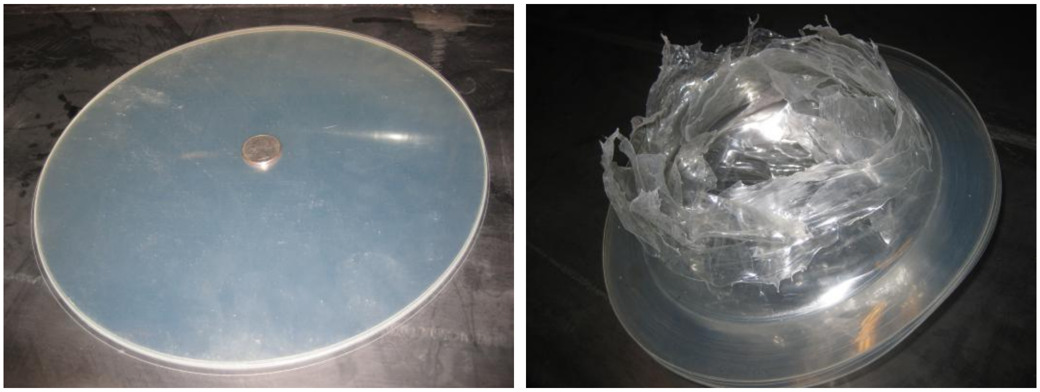

Figure 5-10: Stack of ten x 0.01” burst membranes before and after rupture

Stacking multiple membranes creates a linear increase in burst pressure with an average value of 64.7 psi with a standard deviation of 2.26 psi per membrane. This is nearly half of the 132.6 psi burst pressure measured for a 4 inch breech (Holmberg, 2010). Figure 5-11 shows the best fit trend from 36 different experiments. The burst pressure variations are likely due to different filling rates, membrane inconsistencies, and the pressure sensor accuracy limits. Two outliers are shown but not considered in the linear fit because the membranes were pre-stressed below burst pressure, unloaded, and then pressurized to burst. Loading the membranes at a slower rate could be practiced to obtain higher burst pressures, but this is not currently done.

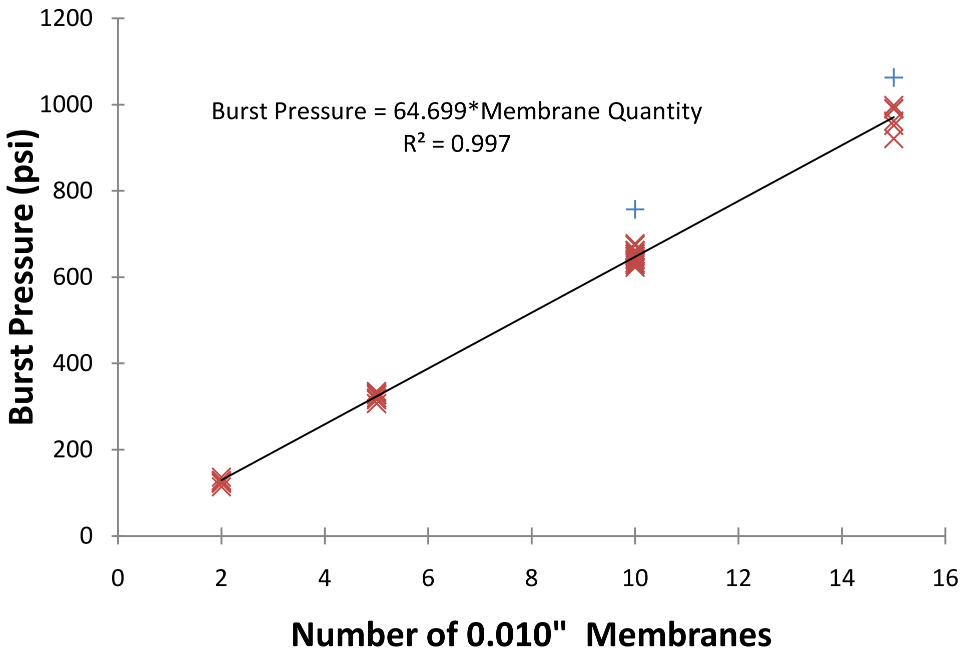

Figure 5-11: Membrane burst pressure compared to the quantity of 0.010" membranes. Average burst pressure of 64.7 psi per membrane. Linear trend does not include two outliers caused by pre-stressed membranes.

5.4 Determination of desired test section location

A variety of factors contribute to determining the location of the test section. The shock profile in the test section must take the form of the desired shock profile (Friedlander for these TBI studies), but there are other considerations that were taken into account as well. The contact surface should not considerably enter the test section because density differences could cause abrupt loading changes. For this reason, an approximation was made to determine how far the contact surface travels into the shock tube. Since far-field blast waves can be considered planar, the shock front planarity was also tested at various locations and described in this section.

5.4.1 Idealized calculation of contact surface location

Upon rapid expansion of the driver gas, the temperature and pressure drops causing a density increase in the driver gas. The location of contact between the driver and driven gas is defined as the contact surface. The shock overpressure across a contact surface does not change, but the density difference causes a discontinuity in kinetic energy. This density difference can cause significant changes in reflected pressure across the contact surface. The use of a heated driver could be used to decrease the density of the driver gas. The contact surface can also be avoided by determining the fully expanded volume of the driver gas, and placing the sample beyond that location. The final volume of the expanded gas can be calculated using the isentropic expansion of an ideal gas, as given by equation 5.1 (Cengel & Boles, 2006).

$$\frac{P_2}{P_1} = \left(\frac{V_1}{V_2}\right)^k \tag{5.1}$$

An example calculation demonstrates a higher pressure shot with nitrogen at 1000 psi using a 24 inch driver length. This driver length has a volume (V1) of 1206 cubic inches. Nitrogen has a specific heat ratio of 1.4, and the gas is assumed to expand to atmospheric pressure (P2) of 14.5 psi. Using these parameters produces an expanded volume of approximately 24,812 cubic inches. The volume of the breech and the transition combined (V2) is approximately 27,500 cubic inches. According to this calculation, the contact surface will not exit the transition, and the sample can be placed anywhere and still avoid the contact surface discontinuity. Performing the same calculation using helium (specific heat ratio of 1.6) produces an expanded volume of 17,002 cubic inches, which is less than the calculation for nitrogen.

The limitation of this analysis is apparent because it assumes that the contact surface does not mix with the driven gas. Observation of actual tests using a nitrogen driver of 30 inches with an 800 psi burst showed that the contact surface partially entered the test section placed 2 feet from the transition. This occurred after the shock profile had almost entirely passed so the measured change in reflected pressure was insignificant. The driver and the driven gas also mix in a turbulent manner making the contact "surface" difficult to distinguish exactly. Nevertheless, high pressure shots with a long driver have a tendency to expose the contact surface to the test section and the results should be monitored for reflected pressure increases.

5.4.2 Determination of shock wave planarity

One method of determining if a shock wave is fully developed in a shock tube is by measuring the shock front planarity. This was done by placing a bar with a linear array of PCB 134 sensors in the shock tube, as shown in Figure 5-12. The shock front planarity was determined by measuring the arrival time at various locations on the bar, and any deviation of arrival time will show the shock front curvature. The distance out of plane was calculated using the timing and the shock front velocity (d=V*t).

One sensor was placed in the center of the bar as well as sensors at 4, 8, and 12 inches from the center in both directions. Assuming the bar is not mounted perfectly perpendicular to the shock tube, averaging of 4A and 4B ensures that non-planarity measurements caused by a skewed bar are corrected. The sensors at 8 and 12 inches were averaged in the same manner. A final sensor was located 13 inches from the center and was adjusted based on the calculated angle of the sensor bar.

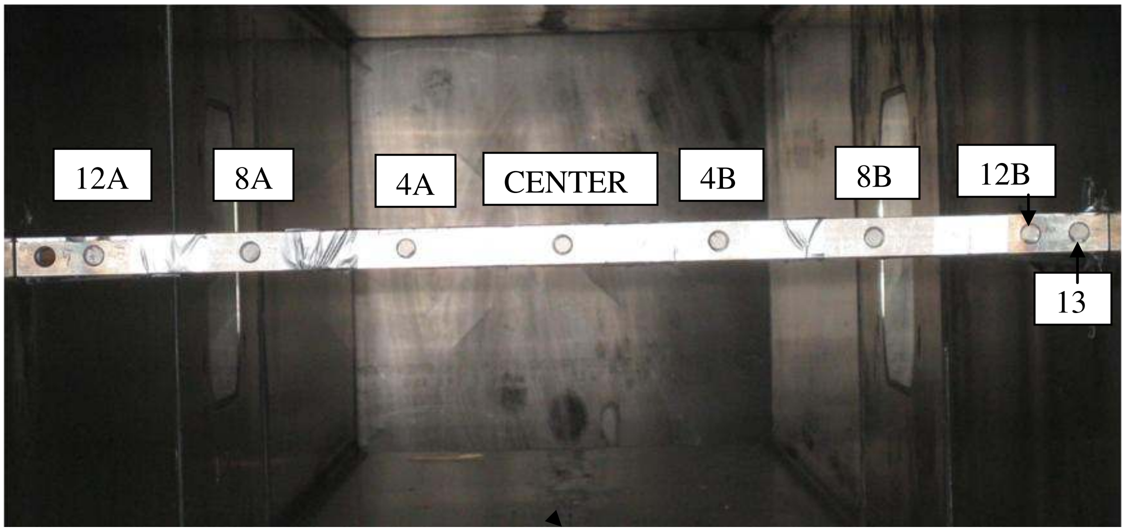

Figure 5-12: Sensor bar used for planarity testing in 28-inch shock tube.

After the sensor bar was mounted, shock waves were generated using an 11.75 inch nitrogen driver and 10 membranes. This produces shock waves with peak overpressures between 15 and 18 psi, depending on the burst pressure and distance from the breech. The sensor bar was mounted 48, 98, and 136 inches from the transition exit.

The planarity results shown in Figure 5-13 demonstrate non-planarity with a shock front leading at the edges by approximately 0.15 inches at a location 48 inches from the transition exit. The curvature corresponds to an approximate diameter of 47 feet, which can be considered planar. This is a rough approximation using 1 data point, but the concept is shown. The results became increasingly planar to the location 136 inches from the transition exit. The results are scattered with some apparent error, but the general trends show increasing planarity at increasing distances from the transition. Nevertheless, the test section was placed 24 inches from the transition (48 inches to center) because short duration Friedlander profiles can be generated with this placement.

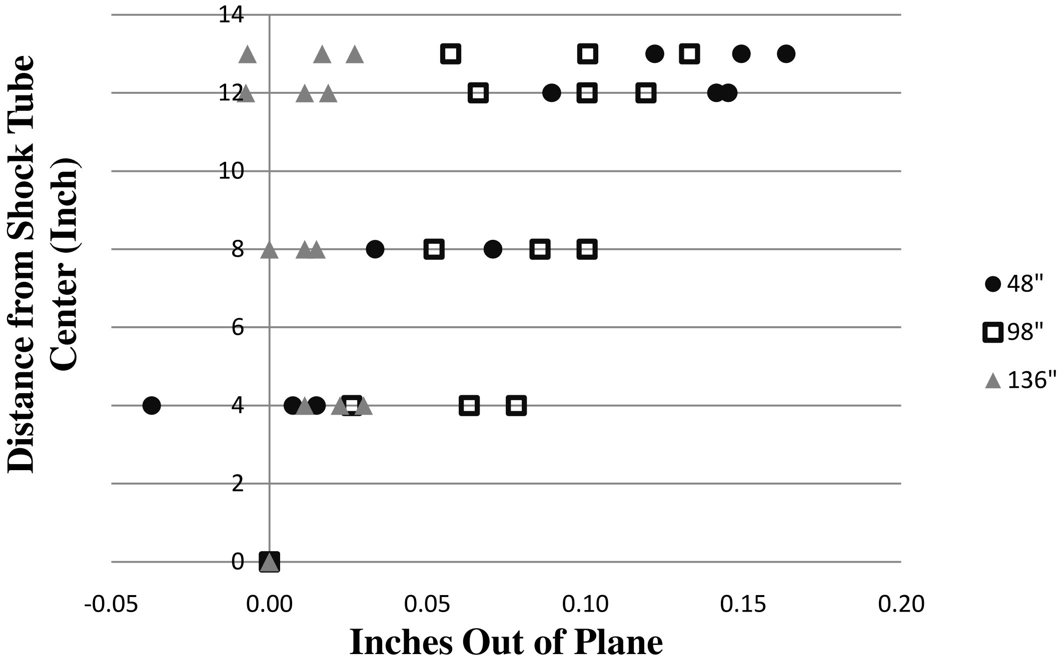

Figure 5-13: Shock wave planarity measurements in 28-inch tube taken at 48", 98", & 136" from the exit of the transition for 18 psi overpressure shock waves

5.5 Shock wave characterization and shock profiles for the 28-inch shock tube

This section outlines several shock tube configurations for generating shock waves, with the majority of the tests geared towards generating Friedlander profiles which replicate blast waves. The effects of varying the driver length, driver gas, number of membranes, and test section position are compared in this section. Adjusting these parameters generates shock profiles with varying pressure, impulse, and duration characteristics.

Assuming the driver length can change and all other parameters are fixed, a very long driver length will produce a flat topped profile with certain peak pressure, duration, and impulse. An "ideal" driver length will produce a sharp Friedlander profile with a peak pressure identical to the flat topped profile, a lower impulse, and a shorter duration. Shortening the driver length more will produce a Friedlander profile but the peak pressure, impulse, and duration will all decrease.

Using a driver gas of a low molecular weight such as helium will produce higher peak pressures than a high molecular weight gas such as nitrogen, but the pulse duration will be significantly shorter. The negative portion of a helium-driven shock wave is much less prominent than from a nitrogen-driven shock wave. The high pressure helium shots did not exhibit any significant negative pressure.

Adjusting the quantity of rupture membranes will linearly increase the burst pressure causing non-linear increases in peak shock wave overpressure and impulse. Empirical polynomial trends were determined for the peak overpressure and impulse. The positive durations tended to increase with increasing burst pressure but not consistently enough to create an accurate trend.

The test section's distance from the exit of the transition is the final parameter that was varied for characterization experiments and primarily changes the shock wave duration. The rarefaction wave from the driver travels faster than the shock front causing the peak pressure of a Friedlander wave to erode and the duration to increase at increased distances from the driver. The maximum peak pressure can be obtained by lengthening the driver as previously described.

5.5.1 Nitrogen driver characterization

As previously mentioned, a nitrogen driver can create a Friedlander profile which exhibits a sharp peak followed by decay and a negative phase. Shock tube characterization with nitrogen was performed with an eight foot and a two foot spacer between the exit of the transition and the test section producing “long” and “medium” duration shock wave profiles respectively. “Short” duration profiles were generated using helium and the two foot spacer section between the test section and transition.

The pressure sensor PCB 1146 was placed in the mounting plate eight inches upstream from the center of the test section. The peak overpressures were determined by averaging 100 data points after the first local peak after the shock arrival. This was typically about 8 microseconds after the shock arrival because of the time for the shock to cross the sensor tip. The maximum impulse is the time integral under the shock wave positive duration. The positive duration is likewise defined as the time between the shock arrival and the location of the maximum positive impulse. The burst pressure was measured using a static pressure transducer mounted in the driver section.

5.5.1.1 Test section placement 8 feet from transition (long pulse durations)

For this test section placement, the driver length was set at 11.75, 17.75, and 23.75 inch lengths and sets of 2, 5, 10, and 15 membranes were used for a total of 12 shots. For these shots the PCB 1146 pressure sensor was mounted in the test section mounting plate located 113.5 inches from the exit of the transition. A summary of the peak pressures, maximum positive impulse, and the positive duration are shown in Table 5-1.

The peak pressures for the 17.75 and 23.75 inch drivers were very similar because the pressure profiles were slightly flat topped, but the peak pressures for the 11.75 inch driver were significantly lower. This leads to the conclusion that the “ideal” driver length is between 17.75 and 11.75 inches. Shots 520 and 521 show a significant difference in impulse (16.4%), but the peak pressure and duration had minor differences (0.2% and 2.7% respectively). This emphasizes the significance of the proper driver length for comparing shock tube data with actual explosive data. One cannot simply characterize a blast wave by the peak pressure and duration. Other factors such as the shape of the wave must be considered as well. This point was emphasized in chapter 4 during the discussion of the loading outside of the shock tube.

Table 5-1: Summary of burst pressure, peak pressure, maximum impulse, and positive duration for test section placement 8 feet from transition exit using nitrogen driver gas.

Membrane Quantity	**Driver Length**	**Shot #**	**Burst Pressure**	**Peak Pressure (100 pt avg.)**	**Maximum Impulse**	**Pos. Duration (@ max impulse)**
	inch		**psi**	**psi**	**psi*ms**	**milliseconds**
2	**11.75**	**495**	**123**	**5.401**	**11.590**	**4.997**
2	**17.75**	**533**	**129**	**5.929**	**15.680**	**5.171**
2	**23.75**	**528**	**127**	**6.067**	**19.820**	**6.125**
5	**11.75**	**492**	**320**	**9.822**	**17.760***	**4.248***
5	**17.75**	**532**	**328**	**11.290**	**32.700**	**6.929**
5	**23.75**	**529**	**327**	**11.350**	**40.560**	**7.648**
10	**11.75**	**496**	**654**	**15.290**	**43.970**	**7.771**
10	**17.75**	**520**	**648**	**17.330**	**54.830**	**8.059**
10	**23.75**	**521**	**643**	**17.290**	**64.650**	**8.282**
15	**11.75**	**497**	**962**	**18.690**	**59.020**	**7.872**
15	**17.75**	**531**	**991**	**21.260**	**76.170**	**9.246**
15	**23.75**	**530**	**998**	**22.230**	**94.540**	**10.918**

(*) Data may not be accurate due to signal noise that was not consistent with other profiles

Since the peak pressures using a 17.75 and 23.75 inch driver were similar, both sets of data were used for determining the maximum overpressure trend shown in Figure 5-14. The second curve on Figure 5-14 contains peak pressure data for the 11.75 inch driver with the test section located 114 inches from the transition. The peak pressure data from Table 5-1 also exhibit properties of the maximum pressure, so those data were also used for the maximum overpressure trend. The best fitting trends are parabolic opening in the positive burst pressure direction and are shown in Figure 5-14. This could be a very useful design tool for experiment development in the 28-inch shock tube. Based on this trend, a peak overpressure of 25.5 psi could be obtained with a burst pressure of 1350 psi if higher pressures were desired. This would require approximately 20 0.010” Mylar membranes.

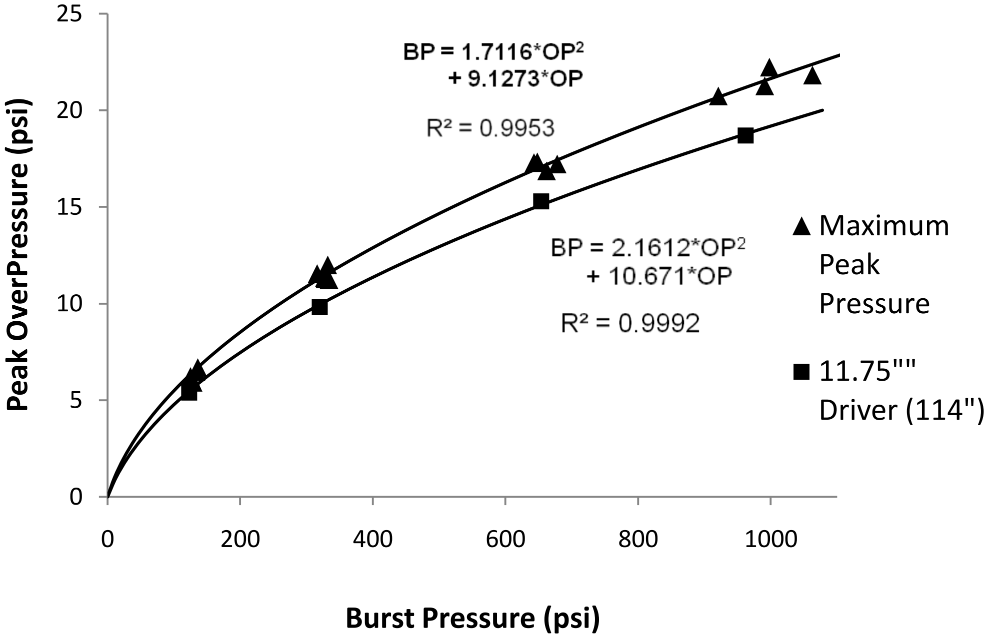

Figure 5-14: Peak overpressure to burst pressure comparison using a nitrogen driver

The trend lines for the maximum impulse at various driver lengths are parabolas opening to the right as shown in Figure 5-15. This demonstrates the impulse increase with rising burst pressure as well as longer driver lengths. The data point for the 11.75

inch driver from shot 492 was not considered due to the inconsistent nature of this profile. The shock profile for shot 492 can be seen in Figure 5-17 along with a description of why this point was excluded. The trend lines are forced to pass through zero, so there are effectively 5 data points for each trend. More data points were not collected because the shock tube is typically consistent, and the trend lines are only intended to be used as a guideline. The collection of free field measurements during experiments is advised.

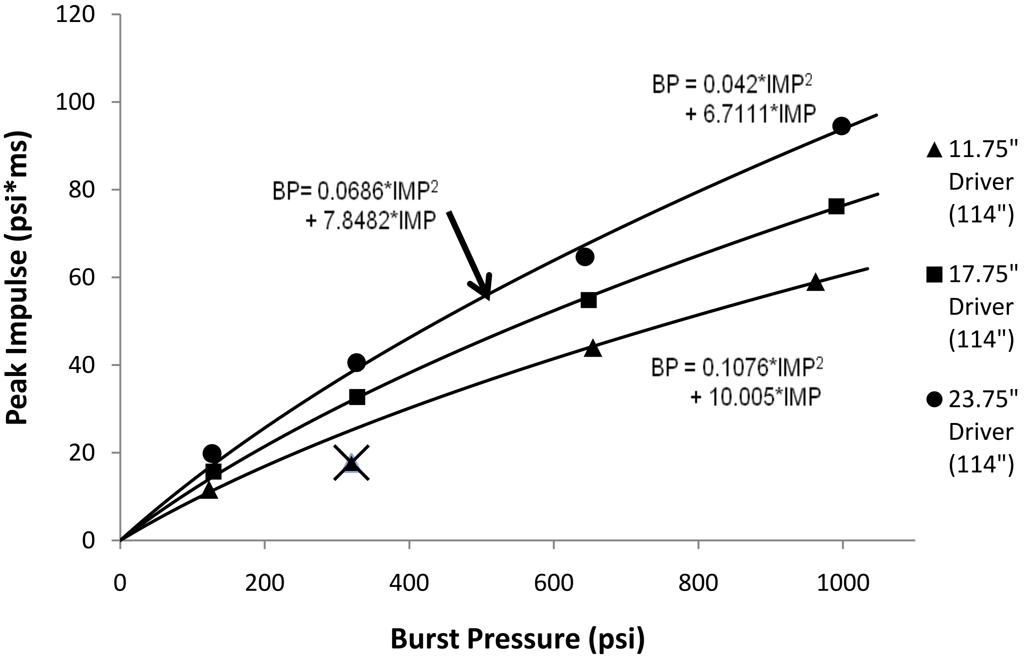

Figure 5-15: Peak impulses using nitrogen driver lengths of 23.75", 17.75", and 11.75". Measurements were taken in the test section 113.5" from the transition exit.

Figure 5-16 shows the shock wave and impulse profiles generated using two 0.010 inch Mylar membranes. The 17.75 inch driver does not produce as sharp of a profile as the 11.75 inch driver but the peak overpressure is slightly higher. This leads to the understanding that a driver length of approximately 15 inches would produce an ideal Friedlander profile with a peak pressure around 6 psi. If a greater impulse is desired at similar pressures, a longer driver length can be used.

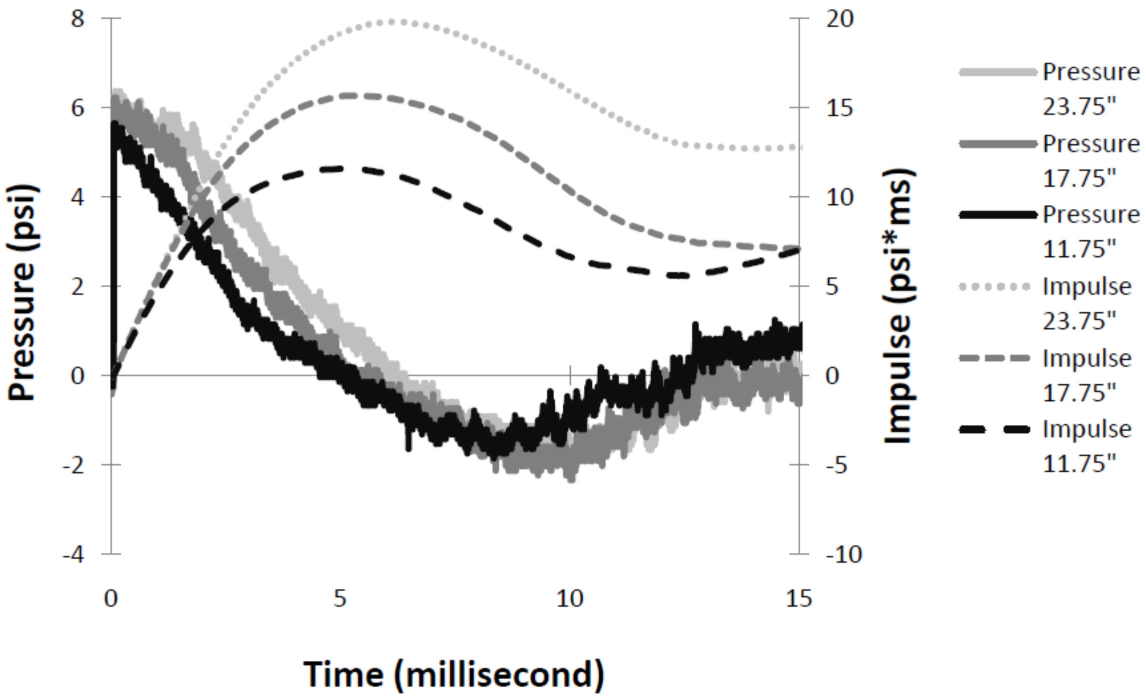

Figure 5-16: Shock and impulse profiles 114 inches from transition exit using a nitrogen driver gas, 2 x 0.01 inch Mylar membranes, and variable breech length.

Figure 5-17 shows shock wave and impulse profiles generated using five 0.010 inch Mylar membranes. Contrary to the two-membrane shots, a driver length of 17.75 inches produced a sharp Friedlander profile at the maximum peak overpressure. A longer driver produced a flat topped profile while a shorter driver produced a profile with a lower peak pressure. Shot number 492 using the 11.75 inch driver length exhibited strong electromagnetic noise which was removed at 6.75 and 10.5 milliseconds as denoted by a small negative spike and a flat region, respectively. This profile was likely compromised by electrical noise, causing a shorter duration and lower impulse than expected.

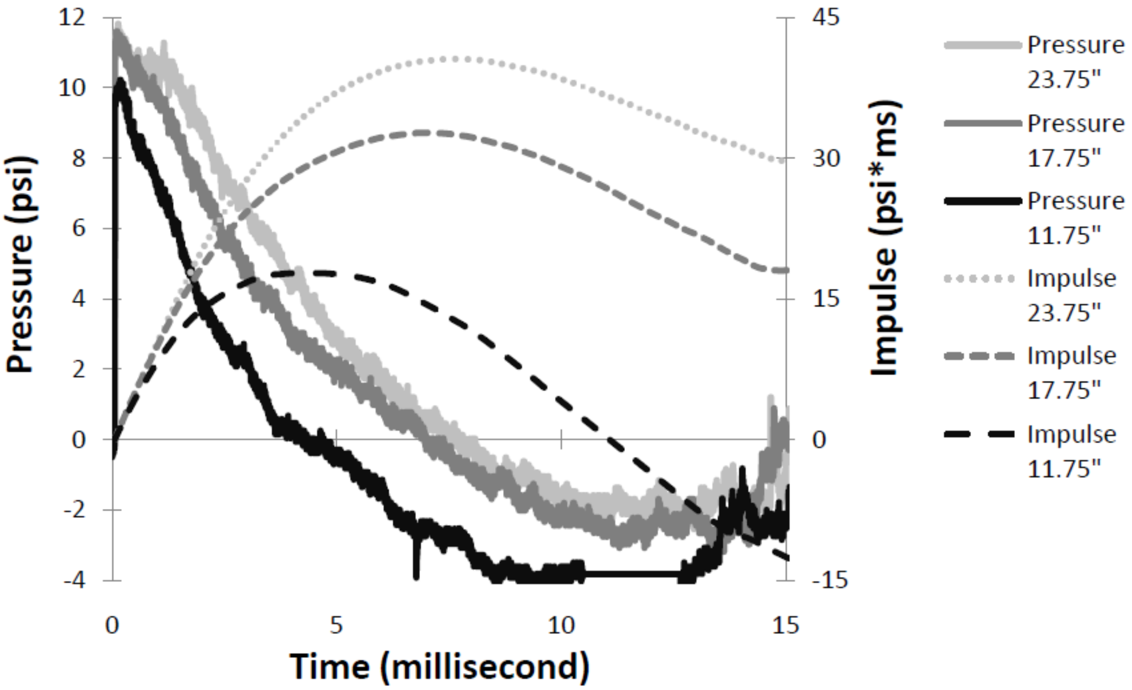

Figure 5-17: Shock and impulse profiles 114 inches from transition exit using a nitrogen driver gas, 5 x 0.01 inch Mylar membranes, and variable breech length

Figure 5-18 shows shockwave and impulse profiles generated using ten 0.010 inch Mylar membranes. The 11.75 inch driver profile is similar to the ones used for the planarity testing in the 28-inch shock tube. The profile generated with a 17.75 inch driver appears to have the best profile since it reached the peak pressure and also has a very sharp peak. These profiles begin to show a crisp secondary shock during the negative phase of the pressure history. The secondary shock is caused by the driver rarefaction creating a vacuum, recompressing, and expanding to form the secondary shock wave. The arrival time of the secondary shock is dependent upon the driver length as well as the pressure behind the shock front. The secondary shock arrives faster for a short driver length.

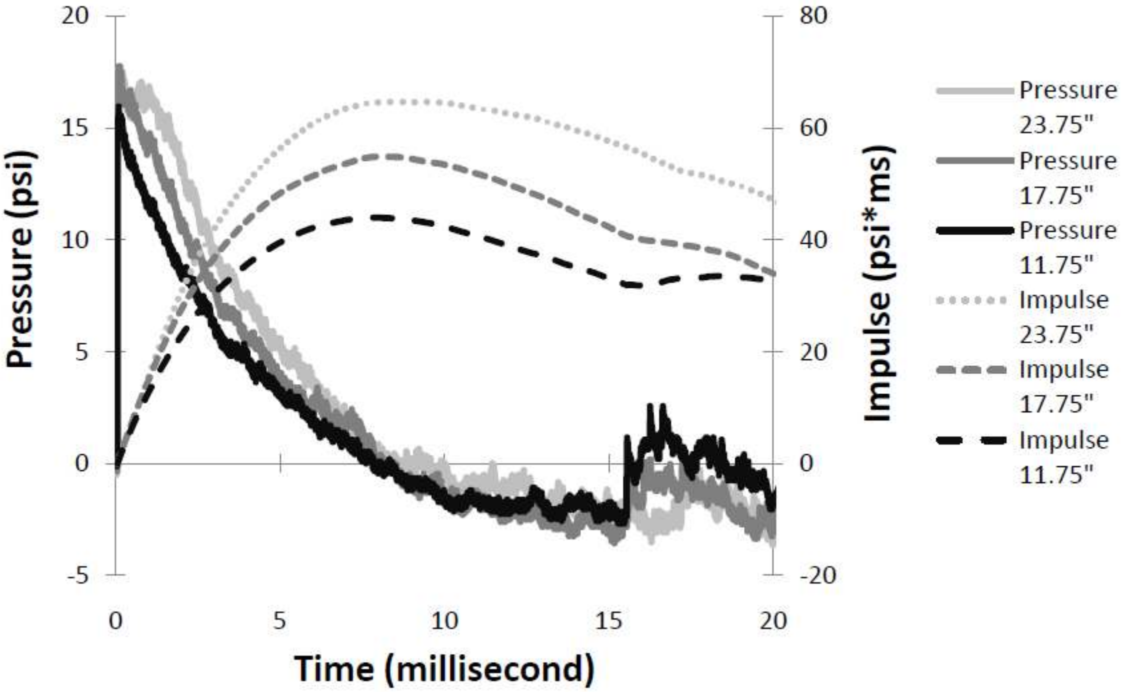

Figure 5-18: Shock and impulse profiles 114 inches from transition exit using a nitrogen driver gas, 10 x 0.01 inch Mylar membranes, and variable breech length.

Figure 5-19 shows the maximum pressure profiles generated using nitrogen with the test section located 8 feet from the transition. Using fifteen 0.010 inch membranes a driver length of 17.75 inches produced a sharp profile near the maximum peak pressure. This profile is the highest intensity Friedlander profile using a nitrogen driver. The pressure profile for the 11.75 inch driver has electrical noise which can be neglected. It also shows a secondary shock before the other profiles due to the shorter driver length.

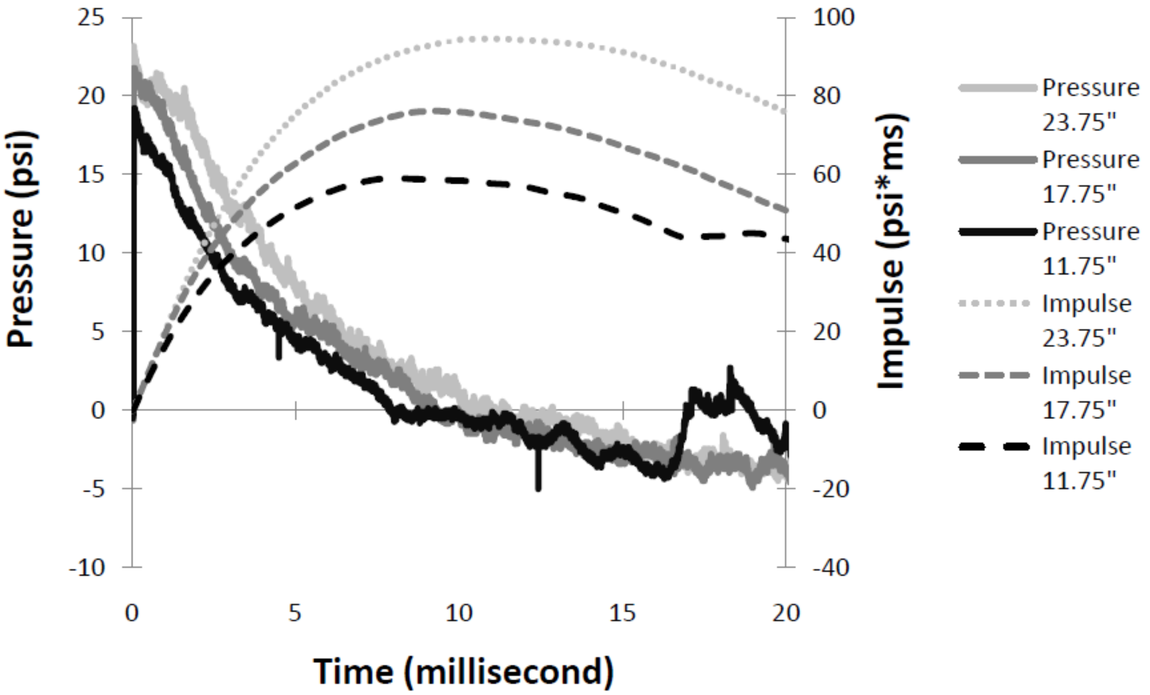

Figure 5-19: Shock and impulse profiles 114 inches from transition exit using a nitrogen driver gas, 15 x 0.01 inch Mylar membranes, and variable breech length.

5.5.1.2 Test section placement 2 feet from transition (medium durations and flat topped)

For this test section placement, the driver length was set at 11.75 and 17.75 inch lengths with membrane sets of 2, 5, 10, and 15. All shots from this set of data reached peak pressure before the rarefaction from the driver deteriorated the peak, so tests with longer driver lengths were not tested for determining ideal Friedlander profiles. Flat topped shock waves were generated using a 47.75 inch breech with 2 and 5 membranes. These low pressure flat topped waves were generated as a proof of concept; higher pressure flat topped waves could be generated but were not tested. For these shots the PCB 1146 pressure sensor was mounted in the test section mounting plate located 41.5 inches from the exit of the transition. These shock profiles have a shorter duration than the previous nitrogen shots because the test section is closer to the driver.

Table 5-2: Summary of burst pressure, peak pressure, maximum impulse, and positive duration for test section placement 2 feet from transition exit using nitrogen driver gas.

Membrane Quantity	Driver Length inch	Shot #	Burst Pressure psi	Peak Pressure (100 pt avg) psi	Maximum Impulse psi*ms	Pos. Duration (@ max impulse) ms
2	11.75	607	125	6.23	11.53	3.976
2	17.75	595	136	6.69	16.16	4.947
2	47.75	625	133	6.48	31.70	8.538
5	11.75	605	316	11.55	24.26	5.244
5	17.75	593	332	12.00	32.96	5.842
5	47.75	624	334	11.24	60.56*	8.984*
10	11.75	603	662	16.86	41.50	6.028
10	17.75	594	678	17.22	55.69	7.006
15	11.75	604	921	20.74	52.30	6.442
15	17.75	596	1063	21.82	75.10	6.763

Since maximum peak pressures were reached for all shots, the peak pressure trend is included in Figure 5-15 in the previous section. The empirically derived relation for the peak overpressure is given for convenience by the following equation.

$$\boldsymbol{BP = 1.7312 * OP^2 + 8.7226 * OP}$$

BP ~ Burst Pressure

OP ~ Over Pressure

The maximum impulse trends for various driver lengths are parabolic opening to the right as shown in Figure 5-20. The impulse trend for the flat topped profile is shown, but not enough data points were generated for an accurate curve fitting. The trend is likely close to being realistic due to the consistency of the other trends.

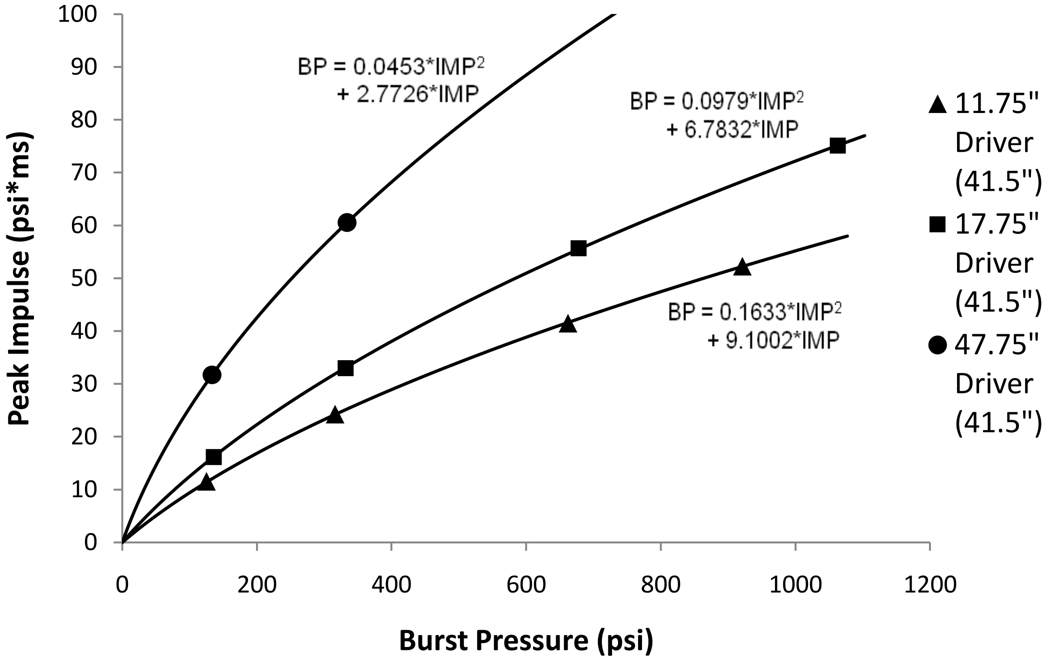

Figure 5-20: Peak impulses using nitrogen driver lengths of 17.75" and 11.75". Measurements were taken in the test section 41.5" from the transition exit.

Figure 5-21 shows the pressure and impulse profiles for various driver lengths using two rupture membranes. A driver length of 11.75 inches appears to produce the best Friedlander profile for this configuration; the setup 113.5 inches from the transition had a longer ideal driver length of 17.75 inches. The "flat top" profile generated with a 47.75 inch driver does not appear to be flat, but tapered on the top. It is assumed that this is caused by charge decay since the peak pressure is 0.7% of the maximum pressure range of the PCB sensor (1000 psi). Higher pressure waves do not see significant peak pressure decay. Using a more sensitive sensor or higher loading pressures should exhibit flat-topped behavior.

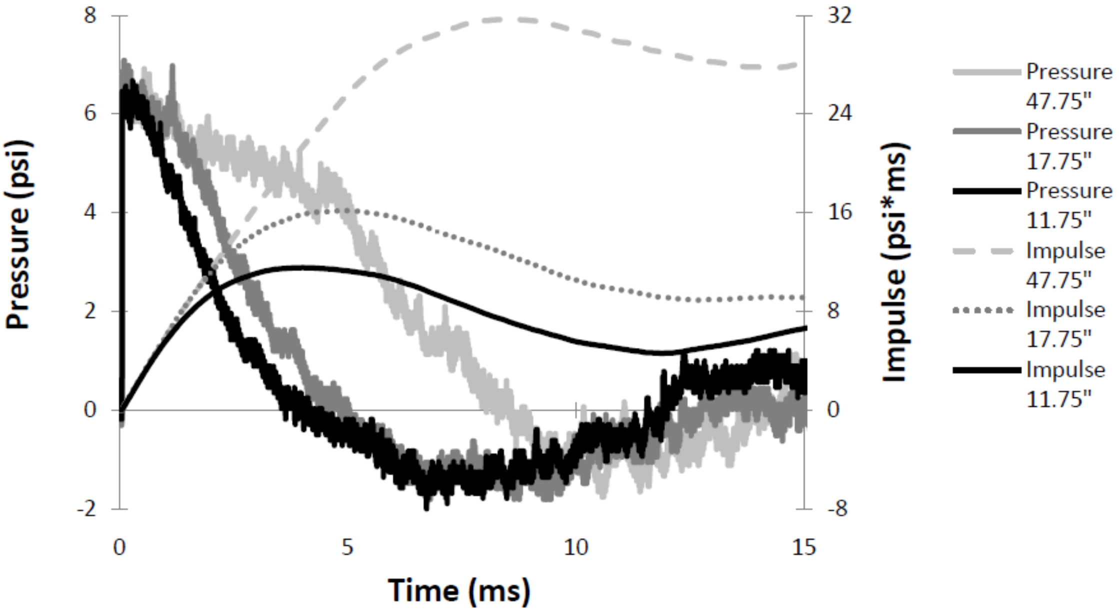

Figure 5-21: Shock and impulse profiles 44 inches from transition exit using a nitrogen driver gas, 2 x 0.01 inch Mylar membranes, and variable breech length.

Figure 5-22 shows three shock profiles generated using five rupture membranes. The best Friedlander profile was generated using the 11.75 inch breech, although a slightly shorter driver could be used to sharpen the peak. The flat topped profile is not shown as perfectly flat but is better than the profile generated with two membranes. The duration of this flat topped wave was determined to be 8.984 milliseconds as shown in Table 5-2, but this was based upon the local maximum of the impulse. Based on observation, the approximate duration is approximately 7 milliseconds. The impulse varies by less than 3% at these two different durations. Higher pressure flat topped waves were not generated, but they could be if desired.

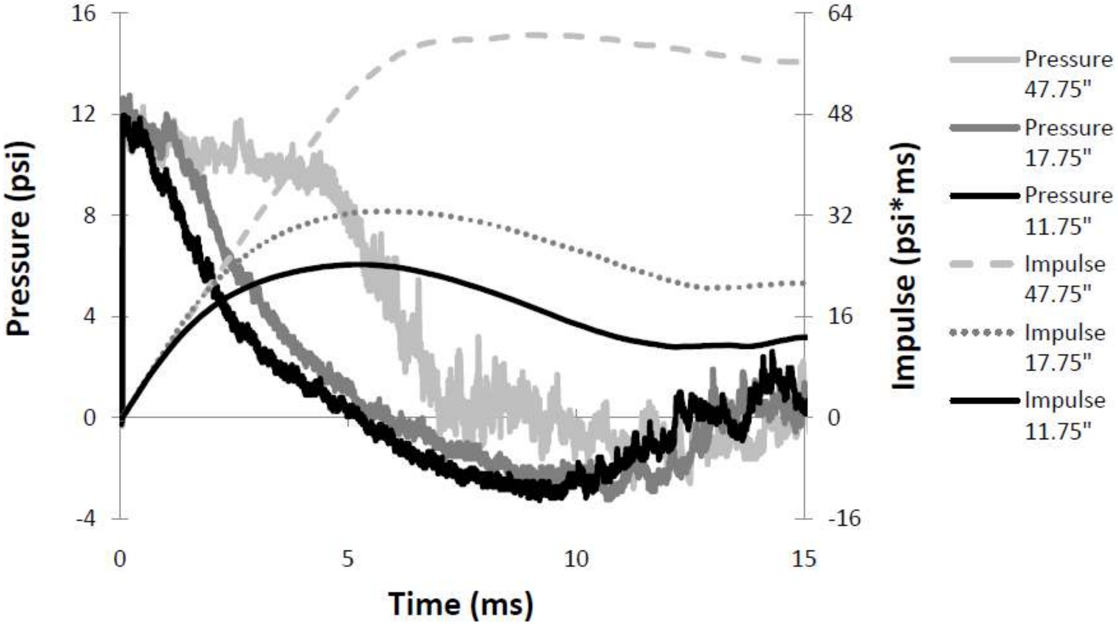

Figure 5-22: Shock and impulse profiles 44 inches from transition exit using a nitrogen driver gas, 5 x 0.01 inch Mylar membranes, and variable breech length.

Figure 5-23 shows the pressure profiles generated in the test section 44 inches from the transition using ten burst membranes. A driver length of 11.75 inches produced a sharp Friedlander profile without degradation in peak pressure intensity. This shock profile exhibits all of the characteristics of an ideal Friedlander profile: fast rise time, sharp peak, and gradual decay to a negative phase. The longer drive length produced a slightly flat topped wave with equal peak overpressure.

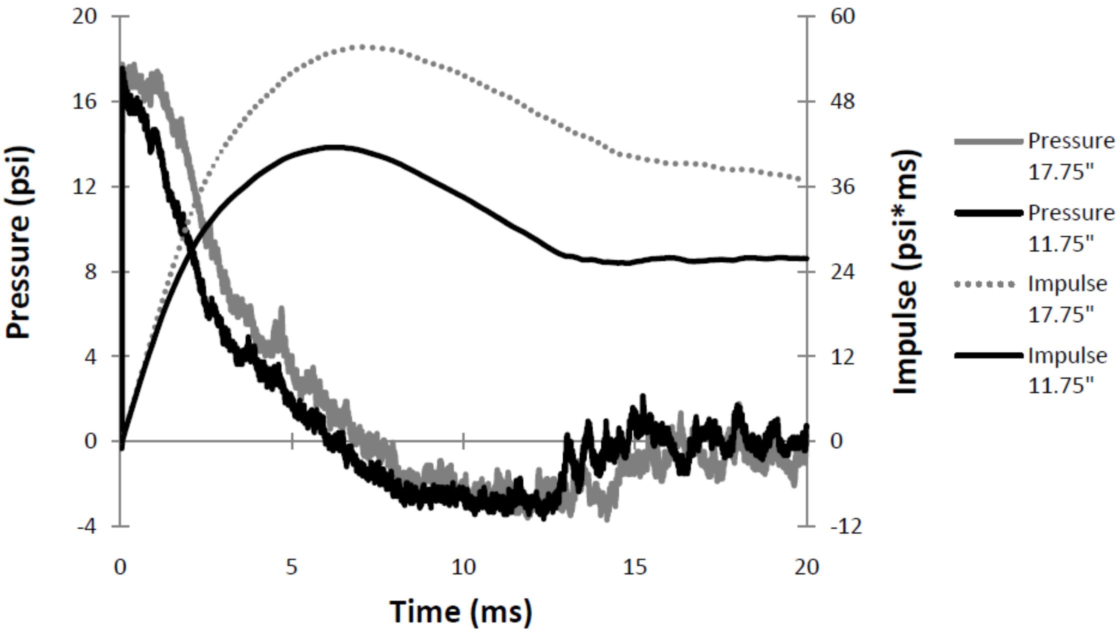

Figure 5-23: Shock and impulse profiles 44 inches from transition exit using a nitrogen driver gas, 10 x 0.01 inch Mylar membranes, and variable breech length.

The highest pressure shots generated with a nitrogen driver are shown in Figure 5-24, and were accomplished using 15 membranes. A driver length of 11.75 inches produced the cleanest, sharpest shock profile with defined positive and negative pressure phases. This profile has a shorter duration than the profiles 113.5 inches from the test section with the same burst pressure. A slight blip occurred after the initial peak in the pressure profile generated with the longer driver. The 100 point average for determining the peak pressure did not include this anomaly. This blip is likely caused by complex flow occurring as the driver gas expands from the driver through non-symmetric transition, but does not influence the shock front rise time.

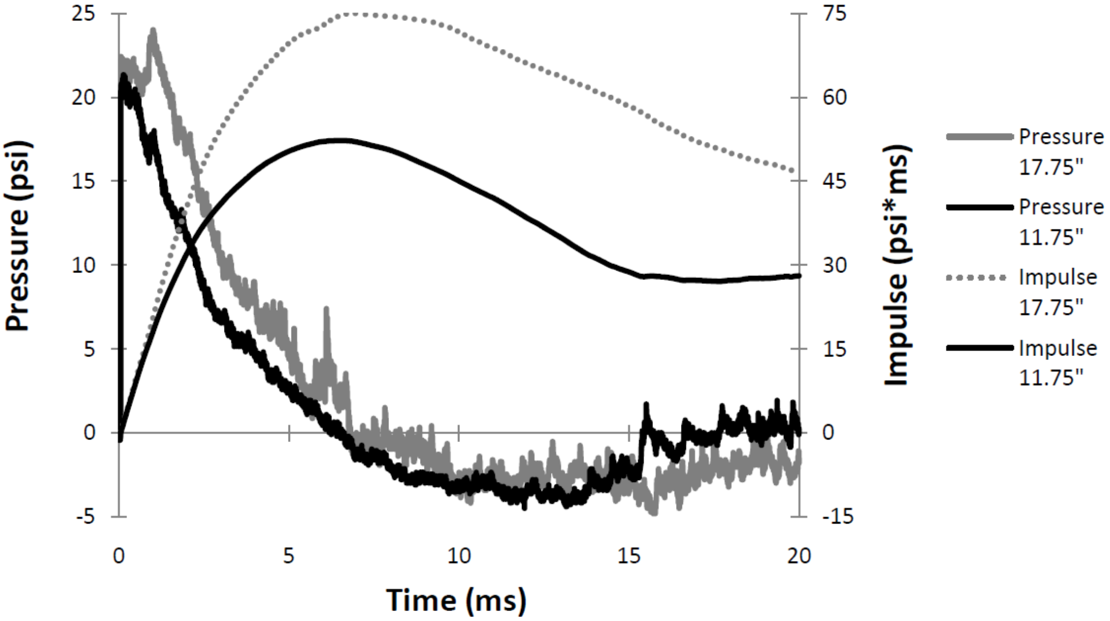

Figure 5-24: Shock and impulse profiles 44 inches from transition exit using a nitrogen driver gas, 15 x 0.01 inch Mylar membranes, and variable breech length.

5.5.2 Helium driver characterization with test section 2 feet from transition (short durations)

Using helium driver gas produces shock waves with peak pressures as much as 85% higher than nitrogen shots using at the same burst pressure. The positive duration of these profiles is also significantly less. Table 5-3 gives a summary of these values for shock waves generated using 17.75 inch and 29.75 inch helium driver lengths.

Table 5-3: Summary of burst pressure, peak pressure, maximum impulse, and positive duration for test section placement 2 feet from transition exit using helium driver gas.

Membrane Quantity	**Driver Length inch**	**Shot #**	**Burst Pressure psi**	**Peak Pressure (100 pt avg) psi**	**Max. Impulse psi*ms**	**Pos.Duration (97% decay) ms**	**Exponential Fit (A*e^{k*t})**	
							A	**k**
2	**17.75**	**602**	**114**	**8.63**	**11.63**	**4.07**	**10.642**	**-0.862**
2	**29.75**	**611**	**122**	**10.59**	**17.08**	**4.66**	**13.54**	**-0.75**
5	**17.75**	**599**	**335**	**16.53**	**22.69**	**4.71**	**18.54**	**-0.745**
5	**29.75**	**610**	**307**	**19.85**	**29.68**	**5.14**	**21.28**	**-0.68**
10	**17.75**	**601**	**629**	**25.52**	**34.47**	**5.32**	**23.446**	**-0.659**
10	**29.75**	**609**	**639**	**30.93**	**46.72**	**5.30**	**31.93**	**-0.66**
15	**17.75**	**600**	**952**	**31.33**	**44.60**	**4.96**	**32.732**	**-0.707**
15	**29.75**	**608**	**990**	**40.87**	**61.49**	**5.65**	**38.80**	**-0.62**

The negative pressure phase is minimal for the lower pressure shots and essentially non-existent for the higher pressure shots. For this reason, the positive duration was determined by an exponential decay curve fitting to the shock profile using the peak to the first location that dropped below 5% of the peak pressure. The positive duration was defined as the time that it took the best fit curve to decay to 3% of the peak value. This is arbitrary, but visual inspection of the pressure traces shows that the calculated durations match quite well. A different criterion could easily be calculated using the given curve fitting parameters, but visual estimation of the duration may be the most accurate method. The maximum positive impulse was then calculated for the 97% decay duration, which may not directly correspond to the maximum impulse shown in Figures 5-27 to 5-30.

Figure 5-25 shows the parabolic peak pressure trends for helium shots with both driver lengths. The trends have R^2 values very close to 1, allowing peak pressures for a given burst pressure to be easily and accurately calculated for a given burst pressure. Since flat topped waves were not observed for the long driver length, the maximum peak pressure is not represented by the upper curve. Increased driver length tests were not pursued because the 29.75 inch driver produces results close to the maximum overpressure and current shock profiles are within the regime pertinent to mild TBI.

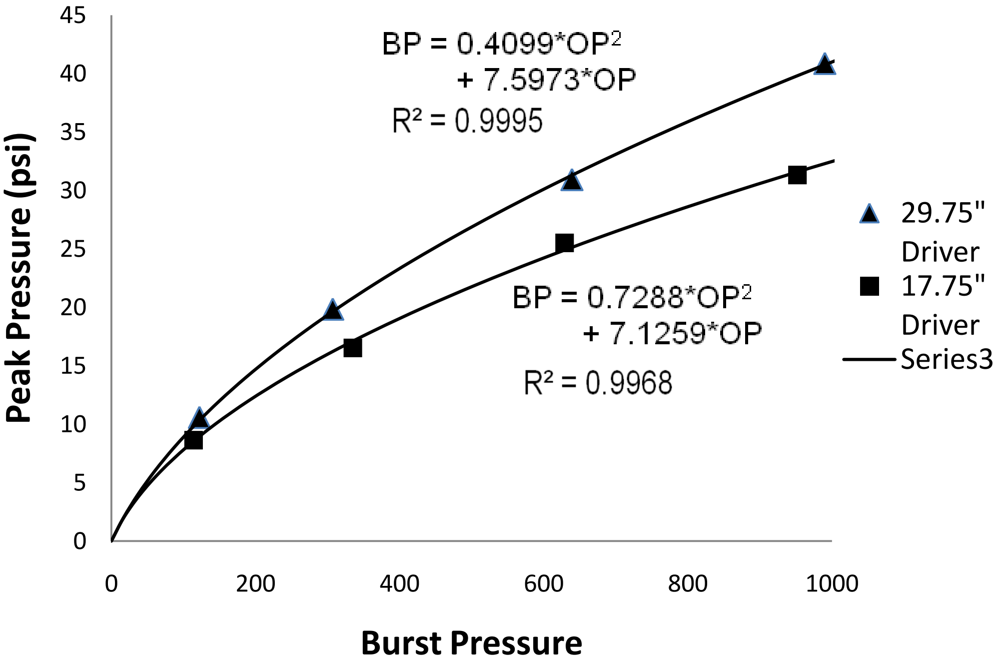

Figure 5-25: Peak pressures using helium driver lengths of 29.75" and 17.75". Measurements were taken in the test section 41.5" from the transition exit.

Figure 5-26 shows the impulse trends using a helium driver which are also parabolic in nature. Visual and statistical inspection shows that the trends are a good fit. These trends are dependent upon the 97% decay interpretation for the positive duration of helium driven shock waves. Since the pressure signal oscillates close to zero after 97% decay, slight duration variations have little effect on the calculated impulse shown. It is apparent how significantly the driver length controls the impulse.

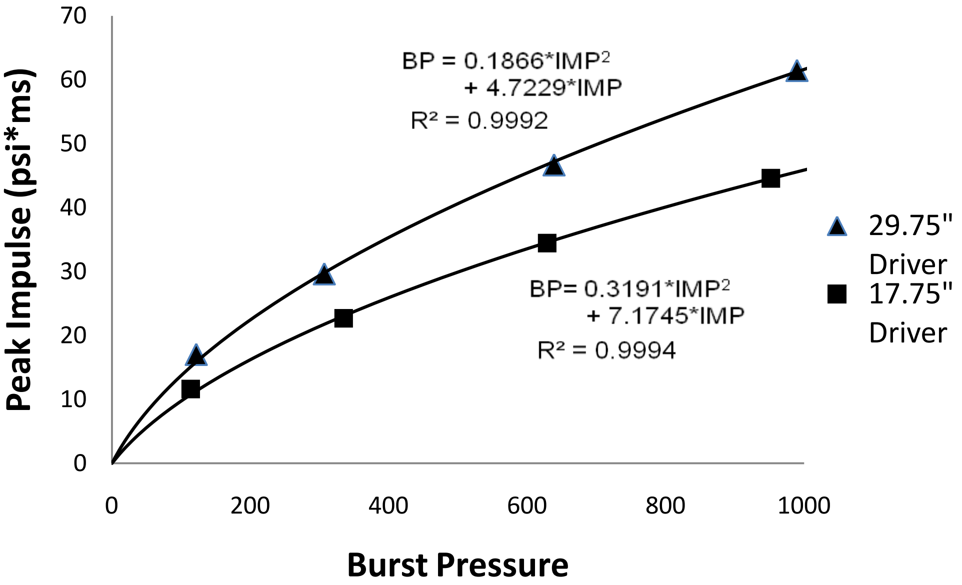

Figure 5-26: Peak impulses using helium driver lengths of 29.75" and 17.75". Measurements were taken in the test section sensor plate 41.5" from the transition exit.

Figure 5-27 shows the pressure traces using two 0.010 inch Mylar membranes and a helium driver. These profiles have a significantly reduced shock wave duration compared to the tests using a nitrogen driver. Both profiles have a sharp peak but the 29.75 inch driver is better for producing a high pressure Friedlander profile. Although using a helium driver in a straight shock tube does not produce a significant negative pressure phase, these profiles do. This is caused by the shock wave expansion through the transition. For lower pressure testing, this setup has shown to produce excellent Friedlander profiles with a short duration (~4.5 milliseconds).

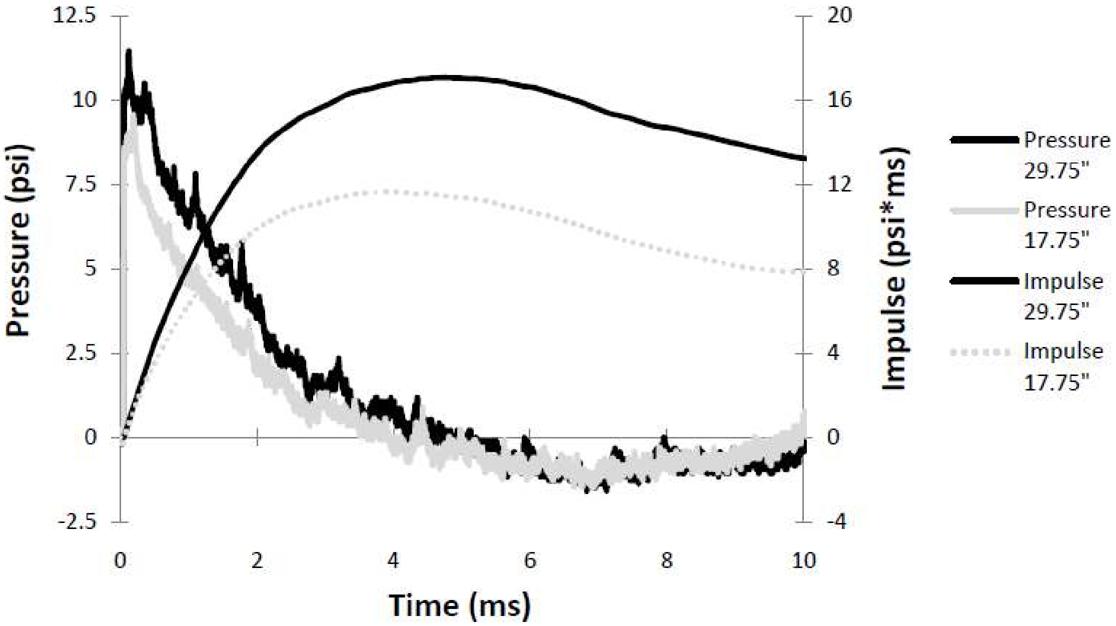

Figure 5-27: Shock and impulse profiles 44 inches from transition exit using a helium driver gas, 2 x 0.01 inch Mylar membranes, and variable breech length.

The sharp peaked pressure profiles shown in Figure 5-28 were generated using five burst membranes, and exhibit all of the features of a Friedlander wave. However, the intensity of the negative phase relative to the rest of the shockwave has declined when compared to the profiles from the two-membrane tests. The peak intensity of the test using a 29.75 inch driver is nearly equivalent to the peak pressure generated with a nitrogen driver and 15 membranes, although the impulse and duration are less.

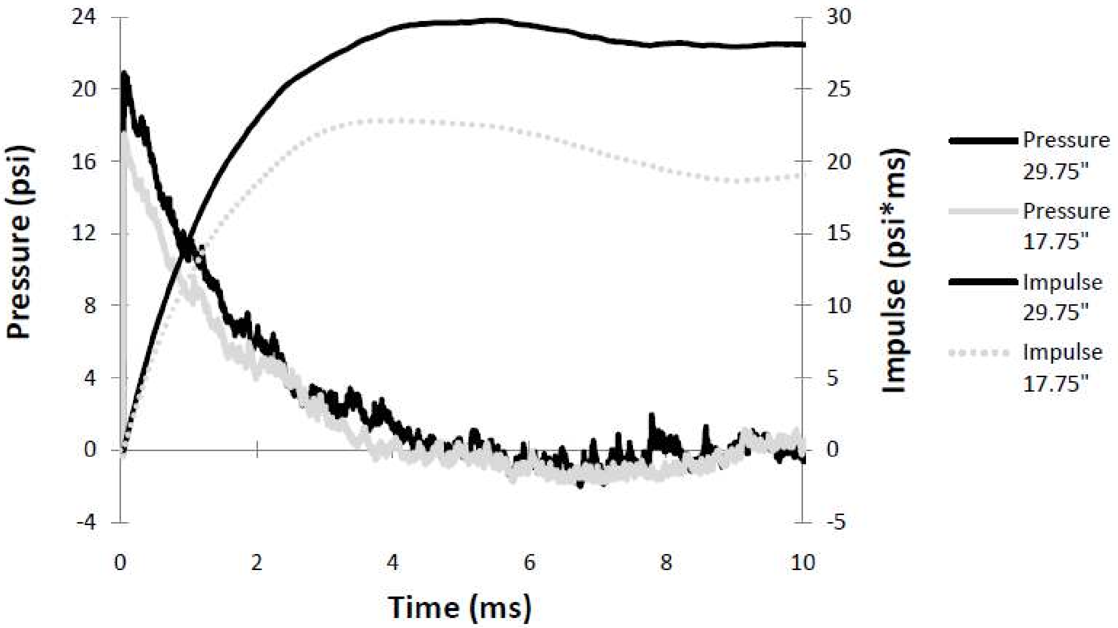

Figure 5-28: Shock and impulse profiles 44 inches from transition exit using a helium driver gas, 5 x 0.01 inch Mylar membranes, and variable breech length.

Figure 5-29 shows two sharp shock wave profiles generated with 10 burst membranes and a helium driver. These shots produced higher peak pressures than what was obtained using nitrogen drivers. The 29.75 inch driver length produces a higher peak pressure and a higher peak impulse than the 17.75 inch driver. Neither profile has a significant negative pressure phase after the positive duration. This is the reason that the positive durations for helium shots were calculated using the 97% decay of the exponential fit.

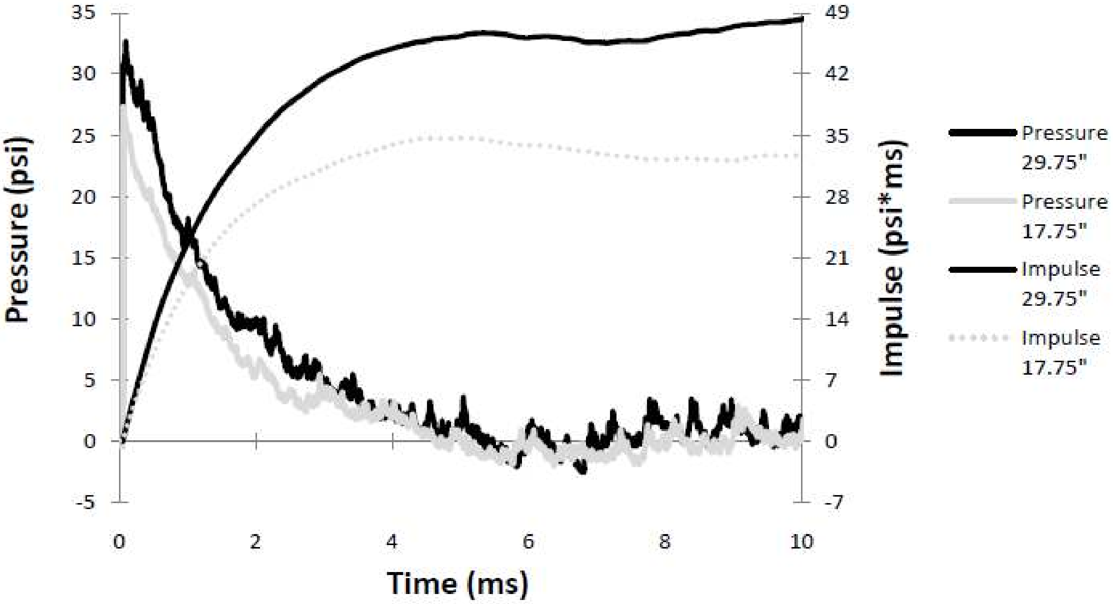

Figure 5-29: Shock and impulse profiles 44 inches from transition exit using a helium driver gas, 10 x 0.01 inch Mylar membranes, and variable breech length.

The final round of helium shots used 15 membranes and corresponds to the highest peak pressure shock waves generated and is shown in Figure 5-30. The 29.75 inch driver produced a peak pressure of 40.9 psi (100 point average), while the shorter driver test produced a much lower peak pressure. These are not ideal Friedlander profiles because they do not have a significant negative duration, but the rest of the shock wave is well developed. A stronger negative portion could possibly be generated by using a shorter transition section, causing the driver gas to expand more rapidly and potentially create a vacuum. This could induce turbulence that would diminish any gains associated with the negative pressure. Simulations would be useful to pre-determine the flow characteristics of a shorter transition section.

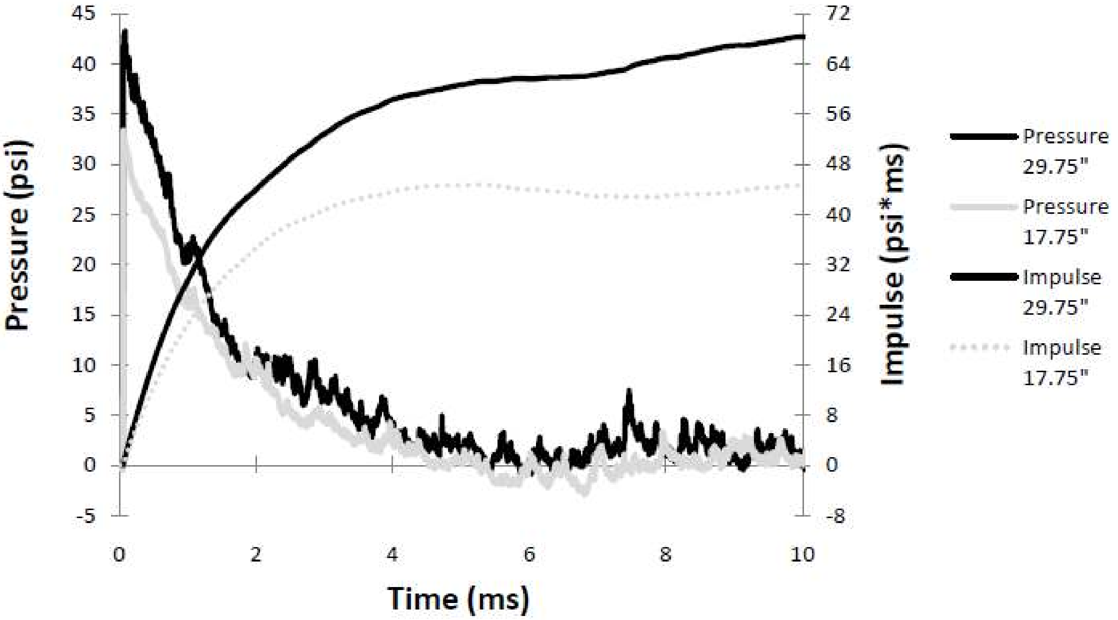

Figure 5-30: Shock and impulse profiles 44 inches from transition exit using a helium driver gas, 15 x 0.01 inch Mylar membranes, and variable breech length.

5.6 Internal reflections caused by dummy head placement in test section

When performing a test inside a shock tube, a rule of thumb is that the maximum amount of area blockage should be 10% (Ritzel, 2009). Part of the design consideration for the 28-inch shock tube was to be able to place a full-scale realistic model head in the shock tube, and generate realistic Friedlander loading conditions. Although the 28-inch shock tube followed this guideline, the actual reflections were measured to determine the significance.

To do this, a dummy head mounting point (neck) was centered at the base of the test section. A side wall pressure sensor was located 16 inches above and 6 inches in front of the closest location on the dummy head for a total distance of 17.1 inches. The test section was located 8 feet from the exit of the transition, and the loading conditions consisted of five 0.010" membranes, a 17.75" breech length, and nitrogen driver gas.

The burst pressures for the test with and without the model head were 318.3 psi and 327.7 psi respectively, which is a 3.0% difference. Figure 5-31 shows two pressure measurements taken with and without the RED head to determine the degree of reflections created. The data were filtered using a 10 point running average in order to show detail. The maximum impulses with and without the RED head are 31.57 psi*ms and 32.68 psi*ms respectively, which is a 3.5% difference, which is similar to the burst pressure difference.

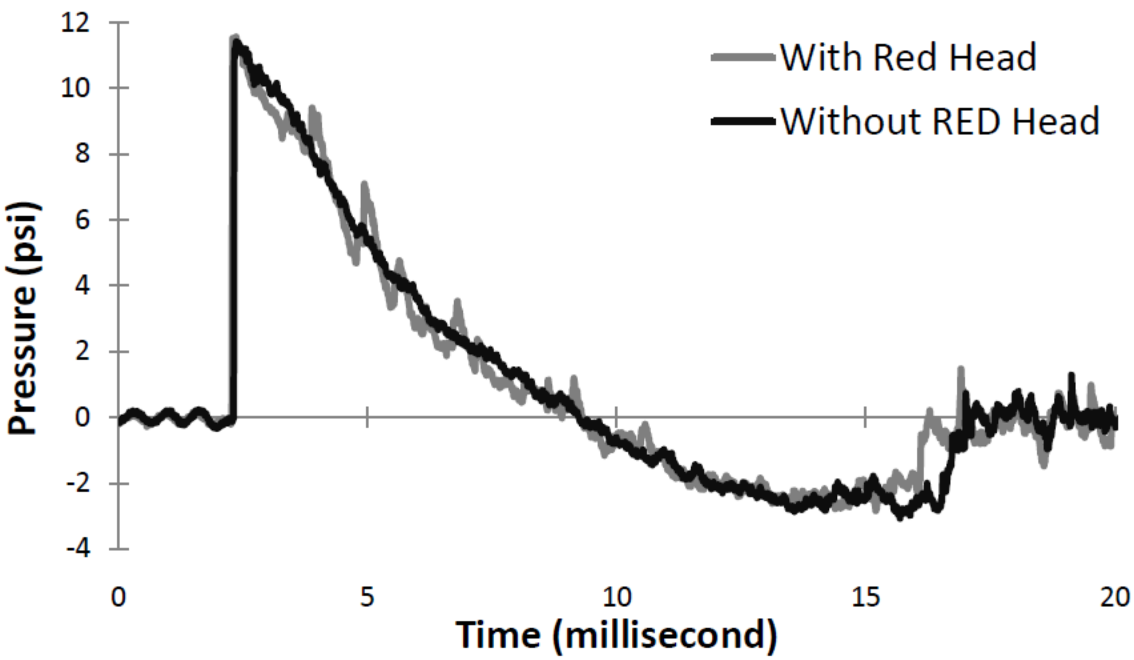

Figure 5-31: Comparison of incident shock wave profile with and without the model head in the tube. Pressure sensor was located on the shock tube wall 6 inches upstream and 16 inches above the closest point on model head.

The timing between the arrival of the shock front and the first reflection was 1.59 milliseconds, which corresponds to an average velocity of 895 ft/s (Mach 0.8) with respect to the fixed shock tube. The velocity with respect to the incoming flow would be much higher. In conclusion the effect of the reflections from the model head has a minimal impact, but it is recommended that reflections be considered when performing experiments in the 28-inch tube.

5.7 Summary

A large-scale 28-inch shock tube was designed, fabricated, and characterized to replicate one dimensional Friedlander shock profiles which accurately represent blast conditions at moderate distances from an explosion source. The design of the shock tube was covered including design requirements and construction. The idea of a catch tank was also used successfully to contain and mitigate the blast energy.

Expansion from 8 inch diameter to 28-inch square caused some turbulent flow which was non-planar by 0.15 inches at a location 48 inches from the transition exit and developed into a planar wave after 10 feet. Although the shock front was not perfectly planar at 48 inches, testing was still conducted near this location to generate high pressure, short duration blast profiles. A byproduct of these studies was the determination that piezoelectric sensors should be mounted in a thick mounting plate to minimize sensor noise induced by acceleration.

Shock wave characterization was performed using nitrogen and helium drivers with 2 and 8 foot spacers between the test section and the transition section. Friedlander profiles ranging from 4 to 9.5 milliseconds and peak pressures up to 41 and 22 psi were generated using helium and nitrogen drivers, respectively. Low intensity, flat topped shock waves were also created. Empirical relations for the peak overpressure and positive impulse vs. burst pressure were developed for predicting loading conditions.

A final test showed that minimal internal reflections are present when a full-scale head-helmet model is tested in the shock tube. Further full-scale head-helmet interaction studies are intended to follow.

Chapter 6: Concluding Remarks

This chapter consists of a brief summary of the previous chapters in this thesis. It also contains suggestions for future studies regarding traumatic brain injury and shock tube development.

6.1 Summary

Traumatic brain injuries are a commonly induced by improvised explosive devices. TBIs can be induced from the blast wave (primary), shrapnel (secondary), or extreme accelerations (tertiary), but the primary blast loading is not currently well understood or protected against. Because this problem is not understood, research has been carried out to replicate and measure these blast waves and their structural interactions with models to better understand the mechanical loading that induces TBIs.

The fundamental principles of shock wave physics were covered. A data measurement and processing system was developed for recording and analyzing shock wave data using LabVIEW. Experiments were performed to demonstrate proper sample placement for blast wave induced TBI experiments. An oil filled cylinder was developed and tested as a simplified head model to understand some of the fundamental potential loading characteristics seen by the skull and brain when exposed to a blast wave. A modular 28-inch square shock tube was developed and characterized for testing full-scale head/helmet interactions and other large experiments.

The data acquisition and analysis system was designed around National Instruments hardware and programmed in LabVIEW to collect and view data in an efficient and repeatable manner. The data collection program was implemented to automatically calibrate data and record all pertinent experimental input parameters. An analysis program is useful for rapid viewing of data and implementing functions such as adjustable scaling, filtering, averaging, and Fourier transforms. The features of two piezoelectric pressure sensors were covered as well as two small-scale pressure sensors (piezoresistive and optical). Experiments in the square shock tubes showed that piezoelectric pressure sensors can produce faulty measurements if significant accelerations induced by shock tube flexure are present. This can be compensated for by mounting the sensors in a thick, rigid plate to minimize flexure and acceleration. It was also experimentally shown that the optical Fiso sensors have a limited loading rate which can cause extreme errors during rapid loading induced by shock waves. These programs and sensors were commonly used for several shock wave studies, so the background information was important for interpreting the data accurately.

A study of an idealized head model was performed inside of the 9 inch square shock tube to better understand wave propagation modes which could lead to a TBI. A mineral oil-filled polycarbonate cylinder was used to represent the two fundamental components of a head: an elastic cylindrical shell (polycarbonate) filled with a viscous fluid medium (mineral oil). Surface pressure, circumferential strain, free field pressure, and internal oil pressure were measured for cylinders with two different shell thicknesses. Timing analysis showed that upon shock arrival, a low intensity surface stress wave is circumferentially transmitted through the shell at the approximate longitudinal sound speed in polycarbonate. A pressure wave in the fluid simultaneously propagates at the fluid sound speed. These waves are significantly faster than the surface pressure wave.

Initially the oil pressures on the front of the cylinder were significantly higher than the center and back pressures. Flow separation and recompression at the 90° cylinder surface caused a prominent negative surface pressure which induced a release in oil pressure followed by re-pressurization in both cylinders. The initial internal oil pressure is not strongly dependent upon the cylinder thickness, but at later times the pressure oscillations are strongly dominated by the structural properties of each cylinder. The thicker, more rigid cylinder oscillated at higher frequencies than the thin-walled cylinder and also experienced cavitation near the loading point. Further investigation is required for the cavitation topic. Although the cylinder is a simplified head model that produced significant results, the wave interactions are complicated and require further study.

Sample placement outside and near the exit of shock tubes has historically been common practice, but the loading characteristics outside the shock tube are significantly different than inside. The necessity for accurately replicating an IED blast led to the development of an experiment to demonstrate these differences by measuring surface pressure on a cylinder at various offsets from the shock tube exit. Results showed degradation in peak pressure and impulse with increasing distance from the shock tube exit as well as significant differences in profile shape. The results showed extreme pressure gradients as well as excessive vacuum pressures outside the shock tube. .External loading was significantly caused by high-velocity turbulent jet flow which is not characteristic of typical blast wave profiles. A far-field blast wave is assumed to be planar, so the shock front planarity was measured at various shock tube offsets. The shock front was planar inside the tube, but became progressively non-planar followed by an increase in planarity. This transition outside the shock tube is associated with the turbulent jet-flow. When using a shock tube to simulate a free-field blast wave, the ideal sample placement is inside the tube in a location tuned to the desired blast profile. Placing a sample outside the shock tube will cause significant loading/damage to a specimen, but it is not characteristic of blast loading.

The necessity to perform blast testing on full-scale head-helmet models led to the development of a 28-inch square shock tube. This shock tube is driven using an 8 inch diameter driver which transitions to the 28-inch section. The driver length can be adjusted from 6 to 48 inches in 2 inch increments allowing the shock wave shape and pressure to be tuned. The 28-inch square sections of the shock tube are modular which allows the test section location to be adjusted for additional shock wave tuning. Helium and nitrogen driver gases were also used to vary shock wave profiles. The test section is equipped with laminated glass windows for viewing a sample during blast exposure. A catch tank was developed to mitigate blast energy exiting the shock tube which reduces noise and prevents damage to lab structures.

Characterization of the 28-inch tube was done using helium and nitrogen driver gases, various driver lengths, and two test section locations. The nitrogen driver produced Friedlander profiles with peak pressures between 5.5 and 22 psi with durations ranging from 4 to 9.25 milliseconds. The helium driver produced higher pressure and shorter duration blast waves ranging from 8.5 to 41 psi and 4 to 5.6 milliseconds. Low intensity flat topped shock waves were demonstrated using a nitrogen driver. A linear fit to burst pressure and membrane quantity showed that the average burst pressure is approximately 65 psi per 0.010 inch thick Mylar membrane. Empirical relations were also developed for peak pressures and peak positive impulse with respect to burst pressure. An empirical relation was not developed for the positive duration because a distinctive trend form did not exist, although increased burst pressure typically showed longer duration profiles. Testing also demonstrated minimal internal reflections caused by placement of a full-scale head-helmet model in the shock tube.

6.2 Recommended Future Studies

Now that three shock tubes are fully functional and characterized in the UNL shock facility there is a lot of potential for future experiments. A continuation of the liquid cylinder experiment is suggested as well as structural testing of cadaver heads to better understand the loading phenomena of skin, skull, and brain material under simulated IED blast loading conditions. The use of a helium driver in conjunction with a shorter transition section could potentially be used to generate high pressure shock waves with a considerable negative phase. Another potential round of experiments could be done to develop and test a reflector plate to reduce secondary loading for the 28-inch shock tube.

6.2.1 Liquid filled cylinder continuation experiments

A continuation to the liquid cylinder test would be to use a cylinder of a different material, but with the same stiffness as the polycarbonate cylinders. The stiffness is the modulus of elasticity times the second moment of inertia (E*I). The pressure inside cylinders of equal stiffness could be compared. This would be a very useful test because polycarbonate has a significantly lower Young's modulus than bone and the use of a higher modulus cylinder with the same stiffness would allow further conclusions to be made about the structural response of bone under blast loading conditions.

Another continuation of the liquid filled cylinder experiment could be the analysis of a liquid filled sphere under shock loading. The liquid filled cylinder experiment involved an idealized structure in two dimensions to simulate the structure of a skull and brain. The blast loading of a two dimensional cylinder gave some insight into what could be happening to the skull and brain under blast loading, but it is an idealization that has potential for error. A spherical model would be a slightly more complicated model than a cylinder, but it would be closer to the reality of an actual human skull.

6.2.2 Dummy head and cadaver testing in 28" shock tube

Testing of a dummy model of a human head is an important step towards understanding the external loading on a human head. A dummy head model can also be used to characterize the effectiveness of military helmets to mitigate the pressurization of the head. However, the material and structural properties of a dummy skull are drastically different than the properties of an actual skull. Therefore, cadaver samples could be used to better understand the structural propagation of shock and pressure waves through skin, skull, and brain material. Strain and pressure measurements could be taken on the surface of the skull and pressure measurements could be taken inside of the brain cavity. This type of testing would require collaboration with medical experts as well as engineers to create a quality testing for the benefit of blast induced TBI research.

6.2.3 End effect tuning of the 28" shock tube

Although the 28-inch shock tube is not currently configured for animal testing, the addition of a partial reflector system could be implemented to reduce the secondary loading created after the primary blast as shown in Figure 6-1. Elimination of the secondary loading associated with A1 and A2 would expose samples to a pure Friedlander wave without additional loading.

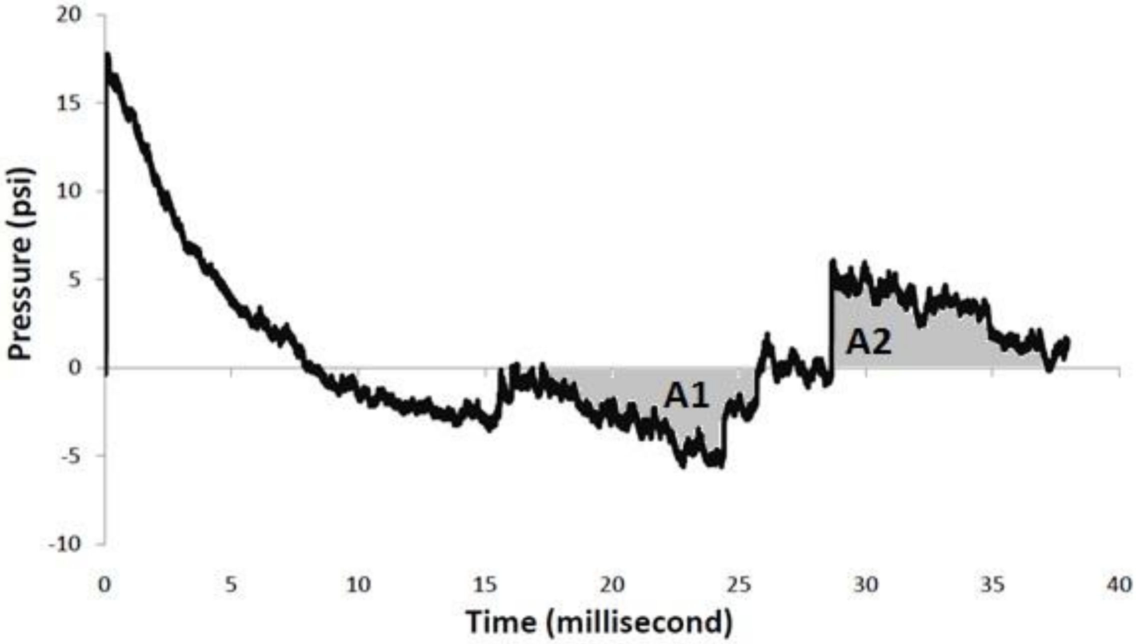

Figure 6-1: Illustration of loading after the primary shock which could be minimized using an offset reflector plate. A1 is induced by a rarefaction from the shock tube exit and A2 is caused by a reflection from the back of the catch tank on the 28-inch shock tube.

This is critical for animal testing because of the necessity for relevant blast loading without secondary effects. The data during secondary loading of a non-living sample can be ignored, but non-relevant loading of a live sample must be eliminated before experimentation to produce accurate loading without extra unknowns. Animal testing must be done in a manner that is scientifically relevant and does not carelessly use living samples. The use of a reflector plate has been implemented and tested on the 9 inch shock tube to minimize these effects as described by Holmberg (2010). Placement of an offset reflector plate/baffle at the end of the 28-inch shock tube would partially eliminate the effect of the rarefaction shown as A1 and the effect of reflection from the catch tank as shown by A2 in Figure 6-1.

6.2.4 Tuning 28" shock tube for increased negative-pressure phase using helium

The lower pressure shock waves generated with helium had a significant negative phase, but the helium-generated high pressure shock waves did not. This is likely caused by the rate the driver gas expands through the transition. Shortening the transition would cause a more rapid expansion and potentially create a significant negative-pressure phase. Although this could generate a negative-pressure phase, a side effect of increased turbulence could occur. A greater distance from the transition may be necessary for turbulent flow stabilization, which could cause the negative portion to dissipate over the increased distance.

Simulation of the current transition could be performed until the simulated data matches measured pressure profiles. Once current data and simulations are matched, a shorter transition configuration could be simulated to determine the feasibility of further optimizing the helium generated Friedlander profiles in the 28-inch shock tube. A shorter transition could be manufactured to fit inside one of the existing 4 foot straight tube sections.

References

Audet, J. (2011). *Failure analysis RMA-7001 on 5 FOP-M-PK-C2-F1-M2-R3-ST.* Fiso Technologies.

Bass, C. R., Rafaels, K. A., & Salzar, R. S. (2008). Pulmonary Injury Risk Assessment for Short-Duration Blasts. *Jaurnal of Trauma Injury, Infection, and Critical Care* , 604-615.

Bauman, R. A., Ling, G., Tong, L., Januszkiewicz, A., Agoston, D., Delanerolle, N., et al. (2009). An Introductory Characterization of a Combat-Casualty Care Relevant Swin Model of Closed Head Injury Resulting from Exposure to Explosive Blast. *Journal of Neurotrauma* , 841-860.

Benson, T. (2008, December 9). *Normal Shock Waves*. Retrieved September 17, 2010, from NASA Web Site: http://www.grc.nasa.gov/WWW/K-12/airplane/normal.html

Boresi, A. P., & Schmidt, R. J. (2005). *Advanced Mechanics of Materials: Sixth Edition.* U.K.: John Wiley & Sons Inc.

Bowen, I. G., Fletcher, E. R., & Richmond, D. R. (1968). *Estimate of Man's Tolerance to the Direct Effects of Air Blast.* Washington D.C.: Defense Atomic Support Agency.

Cengel, Y. A., & Boles, M. A. (2006). *Thermodynamics: An Engineering Approach.* New York: McGraw-Hill.

Cernak, I., Wang, Z., Jiang, J., Bian, X., & Savic, J. (2001). Ultrastructural and Functional Characteristics of Blast Injury Induced Trauma. *Journal of Trauma* , 695-706.

Chavko, M., Kollera, W. A., Prusaczyka, W. K., & McCarron, R. M. (2007). Measurement of blast wave by a miniature fiber optic pressure transducer in the rat brain . *Journal of Neuroscience Methods* , 277-281.

Chen, Y. C., Smith, D. H., & Meaney, D. F. (2009). In-Vitro Approaches for Studying Blast-Induced Traumatic Brain Injury. *Journal of Neurotrauma* , 861-876.

Courtney, M., & Courtney, A. (2010). Working toward exposure thresholds for blast-induced traumatic brain injury: Thoracic and acceleration mechanisms. *NeuroImage* .

CVI Melles Griot. (2011). *Optical Gloassary Character F Selection Fabry-Perot Interferometer*. Retrieved March 28, 2011, from CVI Melles Griot Corporation Web Site: http://www.cvimellesgriot.com/company/Glossary.aspx?Character=F

Dreazen, Y. J. (2010, March). Afghan bombs grow, forcing troops to adapt. *Wall Street Journal* .

Dytran Instruments. (1996, August 12). *Product Data Sheets*. Retrieved March 19, 2011, from Dytran Instruments Web Site: http://www.dytran.com/img/products/2300V.pdf

Engineering ToolBox. (n.d.). *Stress in Thick-Walled Tubs or Cylinders*. Retrieved March 12, 2010, from Engineering ToolBox Web Site: http://www.engineeringtoolbox.com/stress-thick-walled-tube-d_949.html

Esparza. (1986). Airblast measurements and equivalency for spherical charges at small scaled distances. *Explosives Safety Seminar*, (pp. 2029-2057).

Finkel, M. F. (2006). The neurological Consequences of Explosives. *Journal of Neurological Science* , 63-67.

Fiso Technologies Inc. (n.d.). *FOP-M Pressure Sensor*. Retrieved February 24, 2011, from http://www.fiso.com/admin/useruploads/files/fop-m.pdf

Ganpule, S., Gu, L., Cao, G., & Chandra, N. (2009). The Effect of Shock Wave on a Human Head. *ASME International Mechanical Engineering Congress and Exposition*, (pp. 1-8). Lake Buena Vista.

Gosselin, P. (2010, October 19). Email Correspondence.

Hammond, R. (2010, March 16). *Richard Hammond shows how a shockwave can be seen*. Retrieved June 6, 2011, from BBC News: http://news.bbc.co.uk/2/hi/science/nature/8569953.stm

Harrigan, T., Roberts, J., Ward, E., & Merkle, A. (2010). Correlating Tissue Response with Anatomical Location of MTBI Using a Human Head Finite Element Model under Simulated Blast Conditions. *IFMBE Proceedings 32*, (pp. 18-21).

Hoge, C. W., McGurk, D., Thomas, J. L., Cox, A. L., Engel, C. C., & Castro, C. A. (2008, January 31). Mild Traumatic Brain Injury in US Soldiers Returning from Iraq. *New England Journal of Medicine* , 453-463.

Holmberg, A. D. (2010). *Development and Characterization of Shock Tubes for Laboratoty Scale Blast Wave Simulation.*

Honma, H., Ishihara, M., Yoshimura, T., Maeno, K., & Morioka, T. (2003). Interferometric CT measurement of three-dimensional flow phenomena on shock waves and vortices discharged from open ends. *Shock Waves* , 13: 179-190.

Huntington, W. K. (2001). TNT Blast Scalinf for Small Charges. *19th International Symposium of Ballistics*, (pp. 647-654). Interlaken.

Jiang, Z., Onodera, O., & Takayama, K. (1999). Evolution of shock waves and the primary vortex loop discharged from a square cross-sectional tube. *Shock Waves* , 9: 1-10.

Kingery, C. N., & Gion, E. J. (1989). *Jet Flow from Shock Tubes.* Technical Report, BRL.

Kulite Semiconductor Products, Inc. (2010). *Kulites Data Sheets.* Retrieved May 7, 2011, from Kulite Corporation Web Site: http://www.kulite.com/pdfs/pdf_Data_Sheets/LE-080.125.pdf

Long, J. B., Bentley, T. L., Wessner, K. A., Cerone, C., Sweeney, S., & Bauman, R. A. (2009). Blast Overpressure in Rats: Recreating a Battlefield Injury in the Laboratory. *Journal of Neurotrauma* , 827-840.

Merkle, A., Wing, I., & Roberts, J. (2010). Human Surrogate Head Response to Dynamic Overpressure Loading in Protected and Unprotected Conditions. *IFMBE Proceedings 32*, (pp. 22-25).

Microsoft Corporation. (2011). *Excel Specifications and Limits*. Retrieved March 17, 2011, from Microsoft Office : http://office.microsoft.com/en-us/excel-help/excel-specifications-and-limits-HP010073849.aspx

Moss, W. C., King, M. J., & Blackman, E. G. (2009). Skull Flexure from Blast Waves: A Mechanism for Brain Injury with Implications for Helmet Design. *Physics Review Letters* .

Mott, D. R., Schwer, D. A., Young, T. R., Levine, J., Dionne, J.-P., Makris, A., et al. (2008). Blast-Induced Pressure Fields Beneath a Military Helmet. *Bulletin of the American Physical Society*, *53-15.* San Antonio.

National Instruments. (2006, October 6). *NI Developer Zone: Strain Gauge Configuration Types.* Retrieved February 22, 2011, from National Instruments Corporation Web site: http://zone.ni.com/devzone/cda/tut/p/id/4172

NCTC. (2011). *TNT Equivalents for Various Explosives.* Retrieved May 31, 2011, from The National Counter Terrorism Center web site: http://www.nctc.gov/site/technical/tnt.html

Pack, D. C., & Curtis, J. P. (1999). On the effect of asymmetries on the jet from a linear shaped charge. *Journal of Applied Physics* , 6701-6704.

PCB Piezotronics. (2009). *Introduction to Piezoelectric Pressure Sensors*. Retrieved March 3, 2011, from PCB Corporation Web site: http://www.pcb.com/techsupport/tech_pres.php

PCB Piezotronics. (2003, December 5). *Pressure Sensor Model 134A24 Spec Sheet.* Retrieved February 24, 2011, from http://www.pcb.com/spec_sheet.asp?model=134A24&item_id=4059

Physics Animations. (n.d.). *FIBER OPTIC INTERFEROMETER FABRY-PEROT* . Retrieved February 24, 2011, from http://physics-animations.com/sensors/English/interf.htm

Pinet, E., Pham, A., & Rioux, S. (2005). Miniature Fiber Optic Pressure Sensorsfor Medical Applications: an Opportunity for Intra-Aortic Balloon Pumping (IABP) therapy. *International Conference on Optical Sensors*, (pp. 234-237). Bellingham.

Protection Engineering Consultants. (2010). *Our tools: ConWep version 2.1.* Retrieved May 11, 2011, from Protection Engineering Consultants Web Page: http://www.protection-consultants.com/tools/ConWep_V21.html

Rafaels, K. A., Bass, C. R., Panzer, M. B., & Salzar, R. S. (2010). Pulmonary Injury Risk Assessment for Long-Duration Blasts:. *The Journal of Trauma Injury, Infection, and Critical Care* , 368-374.

Ramasamy, A., Harrisson, S. E., Clasper, J. C., & Stewart, M. M. (2008). Injuries from Roadside Improvised Explosive Devices. *Journal of Trauma, Injury, Infection, and Critical Care* , 910-914.

Richmond, D. R., Damon, E. G., Bowen, Gerald, Fletcher, R., & White, C. S. (1966). *Air-Blast Studies with Eight Species of Mammals.*

Ritzel, D. (2009). *Short Course: Basics of Blast Physics, Damage, and Injury.* Lincoln: Dyn-FX Cosulting Ltd.

Selfridge, A. (2009, August 20). *US data for Plastics*. Retrieved April 14, 2011, from Signal Processing Company Web site: http://www.signal-processing.com/tech/

Selvan, V. (2011). *Simulation of Liquid Filled Cylinder.* Powerpoint Presentation, UNL, Engineering Mechanics Computational Group.

Shah, A., Faiez, R., & Khan, M. (2011, May 24). *Roadside Bomb Kills 10, Wounds 28 in Afghanistan*. Retrieved May 26, 2011, from CBS News web site: http://www.cbsnews.com/stories/2011/05/24/ap/asia/main20065744.shtml

Shepherd, J. E., & Inaba, K. (2010). *Dynamic Failure of Materials and Structures.* Springer.

Taylor, P. A., & Ford, C. C. (2008). *Modeling and Simulation of Blast-Induced, Early-Time Intracranial Wave Physics Leading to Traumatic Brain Injury.* Sandia National Laboratories, Albuquerque.

Wardlaw, A., & Goeller, J. (2010). Cavitation as a Possible Traumatic Brain Injury (TBI) Damage Mechanism. *IFMBE Proceedings 32*, (pp. 34-37).

Zel'dovich, Y. B., & Raizer, Y. P. (2002). Physics of Shock Waves and High Temperature hydrodynamic Phenomena. New York: Academic Press Inc.

Zhang, L., Yang, K. H., & King, A. I. (2004). A Proposed Injury Threshold for Mild Traumatic Brain Injury_Zhang. *ASME , 126*, 226-236.